

Title	Metasomatism at a metapelite-ultramafic rock contact at the subduction interface: Insights into mass transfer and fluid flow at the mantle wedge corner	:
Author(s)	Ryosuke Oyanagi, Masaoki Uno, Atsushi Okamoto	
Citation	Journal title (Repository name etc.), Volume, Issue, Pages (Article number) etc. ・ジャーナル名 (刊行物・サイト名) ・巻号・ページ (その他論文番号等): Contributions to Mineralogy and Petrology, 178, 27, (2023)  ・DOI (URL)	
Chation	https://doi.org/10.1007/s00410-023-02011-1  Publication Date: yyyy/mm/dd  · 出版日: 2023 年 4 月 14 日  Publisher  · 出版者: Springer Nature	
Declaration	This preprint is the Author Accepted Manuscript (AAM) of the above.  - 本プレプリントは、上記論文の(受理済)著者最終稿 (AAM) である。  All necessary permissions from the publisher have  - ジャーナル(出版者)から必要な許諾を	
Notes	This version of the article has been accepted for publication, after peer review (when applicable) and is subject to Springer Nature's AM terms of use, but is not the Version of Record and does not reflect post-acceptance improvements, or any corrections. The Version of Record is available online at: https://doi.org/10.1007/s00410-023-02011-1	
		v v4. 2504

# Metasomatism at a metapelite–ultramafic rock contact at the subduction interface: Insights into mass transfer and fluid flow at the mantle wedge corner\*

# Ryosuke Oyanagi†

School of Engineering and Science, Kokushikan University, Tokyo 154-8515, Japan and Research Institute for Marine Geodynamics (IMG), Japan Agency for Marine-Earth Science and Technology (JAMSTEC), Yokosuka 237-0061, Japan

#### Masaoki Uno and Atsushi Okamoto

Department of Environmental Studies for Advanced Society, Graduate School of Environmental Studies, Tohoku University, Sendai 980-8579, Japan

Metasomatism of the subducting slab and mantle wedge influences the rheological and chemical properties of rocks at the subduction zone interface. We investigated a serpentinite body that originated from the mantle wedge in the Tomisato area of the Sanbagawa metamorphic belt, SW Japan. At the boundary between the serpentinite body and a pelitic schist, metasomatic reaction zones have developed, consisting of pelitic schist, albite schist, muscovite rock, chlorite rock, tremolite schist, talc schist, talc+serpentine rock, and serpentinite. Using petrological observations, we showed that metasomatism at the interface occurred around the peak P – T conditions (0.8–1.0 GPa and 530–570 °C), which correspond to those at the mantle wedge corner. Mass balance calculations revealed that the metasomatism of the pelitic schist was accompanied by the removal of Si and Ca and the addition of Mg, whereas the metasomatism of the serpentinite was accompanied by the addition of Ca and Al. The Ca was supplied externally, and Na, K, and C were released to an external system. Fluid-mediated mass transfer induces formation of tremolite-rich rocks after serpentinite and chlorite-rich rocks after metasediments, which could be widespread along the subduction interface and the mantle wedge corner. We propose that metasomatism at the mantle wedge corner redistributes elements between fluids and rocks, introduces spatial heterogeneities in the mineral assemblages in the mantle wedge and subducting slab, and that it could produce fluid overpressure. Consequently, such metasomatism would influence slab-mantle decoupling and seismicity.

#### I. INTRODUCTION

Fluid flow in subduction zones plays a key role in arc volcanism (Marschall and Schumacher 2012), the global water cycle (Rüpke et al. 2004), and seismicity (Hacker et al. 2003). In subduction zones, primary  $H_2O \pm CO_2$  fluids are released from the subducting slab by metamorphic devolatilization, the depth of which has been investigated using thermal, petrological, and thermodynamic models (Peacock and Wang 1999; Gonzalez et al. 2016; Condit et al. 2020). However, the juxtaposition of chemically contrasting rocks at the contact between difference lithologies can lead to metasomatism and dehydration reactions that would not occur if each whole-rock composition was kept separate (Sanford 1982; Peacock 1987; Spandler et al. 2008; Miller et al. 2009; French and Condit 2019; Beinlich et al. 2020; Codillo et al. 2022b, a; Hoover et al. 2022). This metasomatic devolatilization is thought to produce high pore-fluid pressures (Nishiyama 1989; Nishiyama et al. 2017), which may trigger the non-volcanic tremor and episodic slow slip events (Tarling et al. 2019; Okamoto et al. 2021) that are observed at the base of the mantle wedge (Saiga et al. 2013). Moreover, metasomatic devolatilization

Silica is the most abundant chemical component of the crust, and silica minerals are highly soluble at elevated temperature and pressures (Manning 1994, 1997, 2018); therefore, silica metasomatism is expected to produce talc at the interface between the mantle wedge and the subducting slab (Peacock 1987; King et al. 2003; Kim et al. 2013; Nagaya et al. 2020; Peacock and Wang 2021). In contrast, recent thermodynamic modeling suggests that the mobility of Al, Mg, Ca, and C is enhanced by the formation of complexes in response to changes in pH (e.g., Galvez et al. 2015, 2016; Tumiati et al. 2017; Manning 2018; Manning and Frezzotti 2020). Therefore, quantitative estimates of the relative mobilities of these elements are required to understand the spatial and temporal evolution of chemical and mechanical characteristics at the slab—mantle interface.

To better understand the metasomatic reactions and element transfer at the slab–mantle interface, we investigated metamorphic and metasomatic processes at a pelite–ultramafic boundary in the Tomisato district in the Sanbagawa metamorphic belt, SW Japan. Numerous ultramafic bodies occur in the higher-grade parts of the subduction zone, which are thought to have been derived from the mantle wedge (deeper than ~30–40 km depth; Aoya et al. 2013). Systematic reaction zones have developed at the boundaries between serpentinites and pelitic schists. We constrained the P-T conditions and

controls the degree of decoupling along the slab—wedge interface by producing mechanically weak reaction zones consisting of, for example, chlorite- or talc-rich rocks (Hirauchi and Katayama 2013; Hirauchi et al. 2013; Peacock and Wang 2021).

<sup>\*</sup> This version of the article has been accepted for publication, after peer review (when applicable) and is subject to Springer Nature's AM terms of use, but is not the Version of Record and does not reflect post-acceptance improvements, or any corrections. The Version of Record is available online at: https://doi.org/10.1007/s00410-023-02011-1

<sup>†</sup> Corresponding Author. oyanagir@kokushikan.ac.jp

timing of the metasomatic reactions using petrological features, in particular the compositional zoning in garnet from the reaction zone. We carried out mass balance calculations for the transport of elements and fluid flow at the interface, and we discuss the implications of our results for the transport of elements and metasomatic reactions at the subduction zone interface.

#### II. GEOLOGICAL SETTING

The Sanbagawa metamorphic belt is a Cretaceous subduction-related high- to intermediate-P/T metamorphic belt that extends for ~800 km along the southwestern part of Japan (Fig. 1a). The largest part of the Sanbagawa belt occurs in Central Shikoku (Fig. 1a). The belt is divided into four metamorphic zones based on mineral assemblages in pelitic schists: chlorite, garnet, albite-biotite, and oligoclase-biotite zones (in order of increasing metamorphic grade; Enami 1983; Higashino 1990). The peak metamorphic conditions obtained by the conventional geothermometers and phase equilibria were ~360 °C and 0.5-0.6 GPa (pumpellyite–actinolite facies) in the chlorite zone (CHZ), 425–455 °C and 0.7–0.9 GPa (greenschist facies) in the garnet zone (GTZ), 495–545 °C and 0.8–1.0 GPa (epidote amphibolite facies) in the albite-biotite zone (ABZ), and 585-635 °C and 0.9-1.1 GPa (epidote amphibolite facies) in the oligoclase-biotite zone (OBZ) (Enami 1983; Enami et al. 1994; Wallis et al. 2000). Some of the high-grade rocks in central Shikoku experienced eclogite-facies metamorphism (eclogite unit; Wallis and Aoya 2000; Endo et al. 2009, 2012; Kouketsu et al. 2014a; Yoshida et al. 2021). Peak temperatures obtained using Raman analyses of carbonaceous matter in metasediments from the Sanbagawa belt have yielded broadly consistent results with those estimates, although there is some spatial heterogeneity even within the same metamorphic zones (Kouketsu et al. 2021). Higher peak temperatures (~500 °C) have been reported in some parts of the GTZ, and lower peak temperatures (~400 °C) in some parts of the ABZ (Kouketsu et al. 2021).

The Sanbagawa belt contains pelitic, psammitic, and mafic schists along with minor metachert, and is the result of the subduction of an oceanic sedimentary sequence that was deposited on basaltic oceanic crust. In addition, there are numerous ultramafic blocks and bodies (peridotite, serpentinite, and tremolite schists), centimeters to kilometers in scale, in the parts of the belt that are higher in grade than the CHZ or around the boundaries between the CHZ and GTZ (Kunugiza et al. 1986; Banno 2004; Aoya et al. 2013; Mizukami et al. 2014; Hirauchi et al. 2021; Okamoto et al. 2021). These are thought to be blocks of paleo-mantle wedge that became incorporated into the subduction complex that formed along the Cretaceous Eurasian margin (Aoya et al. 2013).

We investigated an ultramafic body in the Tomisato distinct, central Shikoku, Japan (the Tomisato ultramafic body;  $33^{\circ}53'46.1"N 133^{\circ}28'55.7"E$ ; Fig. 1a–b). The body is located in the GTZ, closed to the boundary with the ABZ (Fig. 1b). The peak P-T conditions in this region are estimated

to have been 1.0–1.1 GPa and 500–550 °C (Okamoto and Toriumi 2005), slightly higher than those estimated for the GTZ. The depleted compositions of Cr-rich spinel in the serpentinite from Tomisato distinct suggest that the Tomisato ultramafic body originated in the mantle wedge rather than in the subducting slab (Hirauchi et al., 2021). Hirauchi et al. (2021) described block-in-matrix structures in antigorite serpentinite from the Tomisato ultramafic body and proposed that the antigorite in the matrix was oriented favorably for slip deformation by dislocation creep. Our study focused on chemical exchange between the pelitic schist and serpentinite that may have occurred after the initial deformation.

#### III. METHOD

The minerals were examined in thin sections cut perpendicular to the foliation and parallel to the lineation. The compositions of the minerals were analyzed using an electron probe microanalyzer (EPMA; JEOL JXA-8200) at JAM-STEC, Yokosuka, Japan, using an accelerating voltage of 15 kV and a beam diameter of 1–5 µm. The beam current was 1–10 nA for quantitative analysis, and 50 nA for element maps. Wollastonite (Si, Ca), rutile (Ti), corundum (Al), hematite (Fe), MnO, periclase (Mg), albite (Na), sanidine (K), and Cr<sub>2</sub>O<sub>3</sub> standards were used for calibration. ZAF corrections were applied to convert raw data to wt.%. Amphibole compositions were calculated using the method of Dale et al. (2005) and classified according to the scheme of Leake et al. (2003).

Mineral phase maps and quantitative elemental maps were made using XMapTools (Lanari et al. 2014). Mineral phase maps were generated from EPMA elemental maps over areas of >2000  $\times$  2000  $\mu$ m with a beam diameter of 10  $\mu$ m and were used to estimate the modal abundance of each phase.

To determine the porosity and density of the samples, we used the triple weighing method (e.g., Dullien 1992). This involved drying the samples in an oven to obtain their dry mass  $(M_{dry})$ , and then measuring their mass when saturated with water while in air  $(M_{sat})$  and in water  $(M_{im})$ . The porosity  $(\phi)$  and density  $(\rho)$  of the samples were calculated using the equation  $\phi = (M_{sat} - M_{dry})/(M_{sat} - M_{im})$  and  $\rho = \rho_w M_{dry}/[(1-\phi)(M_{sat}-M_{im})]$ , where  $\rho_w$  is the density of water. The porosity and density were determined for three rock specimens per sample (10-50 g), and the measurements were repeated three times. The precision of the density measurements was < 0.8%.

The whole-rock major and minor element (V, Cr, Ni, Cu, Zn, As, and Sn) compositions of the samples were determined using a wavelength-dispersive X-ray fluorescence spectrometer (WDXRF; Rigaku RIX2100) and an energy dispersive X-ray fluorescence spectrometer (EDXRF; PANalytical Epsilon 5), respectively, at Tohoku University, Sendai, Japan. For WDXRF analyses of major element compositions, glass disks of the samples were prepared. Six grams of powder from each sample was heated at 105 °C for 3 h to remove moisture. The major element analyses excluded volatile contents, and loss on ignition (LOI) values were determined by heating the samples

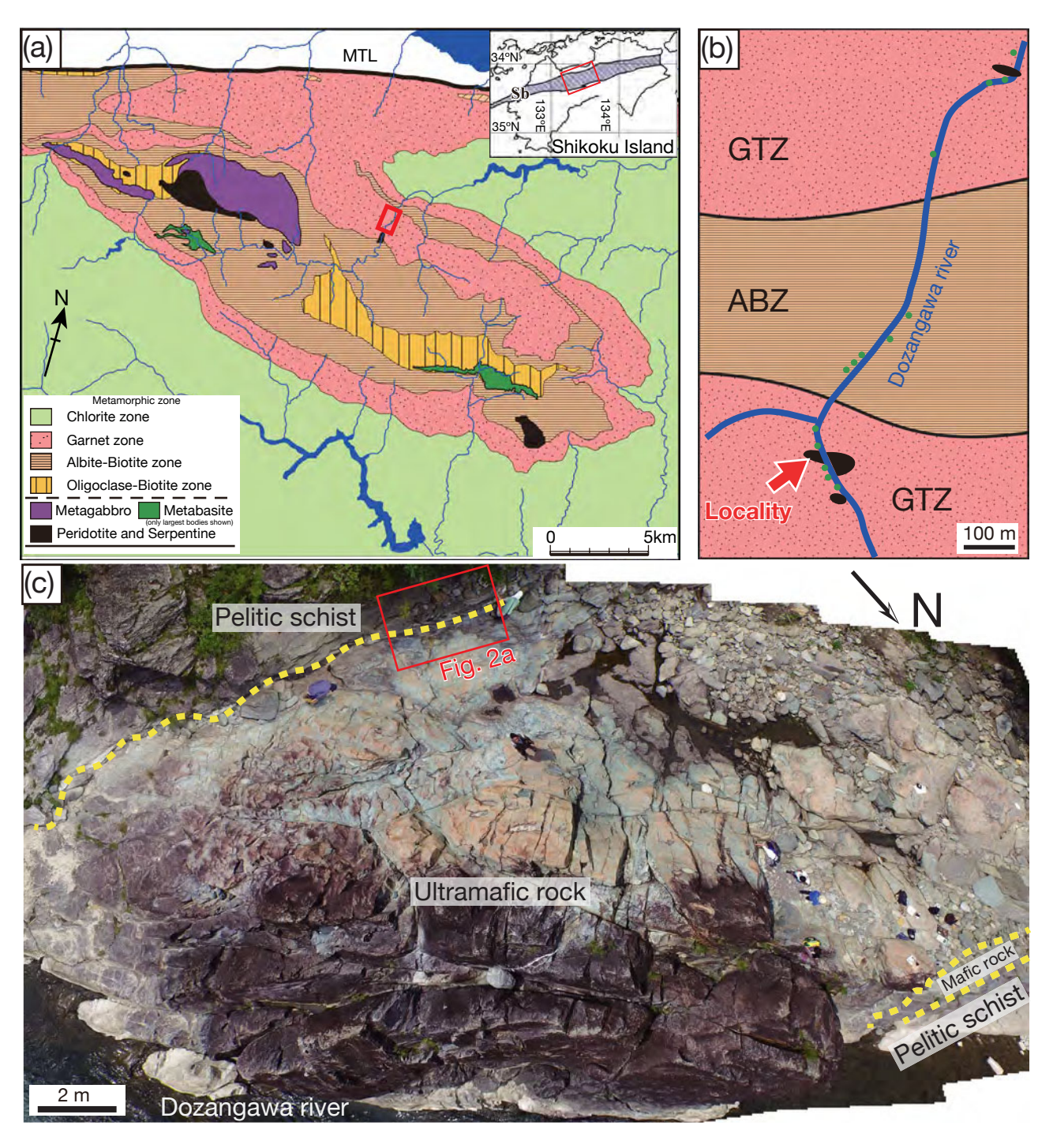


FIG. 1. (a) Geological map showing the metamorphic zones of the Sanbagawa metamorphic belt, central Shikoku, Japan (modified after Higashino 1990; Mouri and Enami 2008; Mori and Wallis 2009; Kouketsu et al. 2010). The bold red rectangle indicates the study area, enlarged in (b). The inset map shows central Shikoku and the Sanbagawa metamorphic belt (Sb; Wallis et al. 2020). (b) Geological map of the survey area. The green and black circles show the occurrence of mafic schist and ultramafic rock, respectively (after Okamoto and Toriumi 2005). (c) Plan view photograph of the ~20 m wide Tomisato ultramafic body taken by drone (DJI Mavic pro). The yellow dotted lines indicate lithological contacts. The red box indicates the pelitic schist—ultramafic rock boundary investigated in this study.

at 950 °C for 6 h. Glass disks were prepared by heating 5.4 g of flux (49.5% LiBO<sub>2</sub>, 49.5% Li<sub>2</sub>B<sub>4</sub>O<sub>7</sub>, and 1% LiBr) and 0.6 g of sample in a muffle furnace at 1050 °C. The glass disks were irradiated using X-rays from an Rh anode tube with an

accelerating voltage of 75 kV and a beam current of 8 mA. For EDXRF analyses of minor element compositions, pressed pellets were prepared from the samples. A polyvinyl chlorite ring sample holder (3 cm in diameter and 0.5 cm thick)

was used. Each pellet was pressed at 100, 150, and 200 MPa for 1 min each. An acceleration voltage of 75–100 kV and a beam current of 6–8 mA were used during the analyses. The Igneous Rock Series (Geological survey of Japan; GSJ) and 26 geological and environmental standard reference materials (Yamasaki et al. 2011) were used as reference standards during the WDXRF and the EDXRF analyses.

Trace element [14 rare earth elements (REEs), Ba, Th, Nb, Y, Hf, Ta, U, Pb, Rb, Cs, Sr, Sc, and Zr] compositions of the samples were determined using inductively coupled plasma-mass spectrometry (ICP-MS; Agilent 7700) at the GeoAnalytical Lab, Washington State University (WSU). The preparation techniques are described in detail by Steenberg et al. (2017). Powdered samples were mixed with an equal amount of lithium tetraborate flux (typically 2 g), placed in a carbon crucible, and fused at 1000 °C in a muffle furnace for 30 min. After cooling, the fused bead was ground briefly in a carbon steel ring mill and a 250 mg portion was placed in a 30 ml screw-top Teflon PFA vial for dissolution. This consisted of a first evaporation with 2 ml HNO3, 6 ml HF, and 2 ml HClO<sub>4</sub> at 110 °C. After evaporating to dryness, the sample was wetted, and the sides of the vial were rinsed with a small amount of water before a second evaporation with 2 ml HClO<sub>4</sub> at 160 °C. After the second evaporation, the samples were dissolved in ~10 ml of water, 3 ml HNO<sub>3</sub>, 5 drops of H<sub>2</sub>O<sub>2</sub>, and 2 drops of HF, and warmed on a hot plate until a clear solution was obtained. The solutions were then analyzed by ICP–MS. The long-term coefficient of variation of ICP-MS at WSU is <2% for Ce, Pr, Nd, Tm, Yb, Y, Hf, Sr and U; <4% for La, Gd, Er, Lu, Ba, Pb, Rb, Th, Ta, Cs, Sc, and Zr; <6% for Sm and Eu; and <10% for Tb, Dy, Ho, and Nb (Steenberg et al., 2017). The Eu anomaly (Eu/Eu\*) was calculated as  $Eu_{CN}/[Sm_{CN}GD_{CN}]^{0.5}$  (McLennan 1989), where the subscript CN indicates normalization to chondrite.

Raman spectroscopy (Nanophoton RAMANtouch) was conducted using a 532 mm laser and a 1200 mm<sup>-1</sup> grating at JAMSTEC. The Raman peak position was calibrated using a silicon wafer (520.7 cm<sup>-1</sup>). The Raman spectroscopy on carbonaceous material (RSCM) thermometer was used to estimate the peak temperature of the metasedimentary rocks associated with the ultramafic rocks. For RSCM, the laser power at the sample surface was set to 1–3 mW. We followed the analytical procedure described by Beyssac et al. (2002, 2003, 2007). The degree of graphitization of carbonaceous matter (CM) was evaluated by the relative areas of the G, D1, and D2 Raman bands. The R2 ratio [R2 = D1/(G + D1 + D2)]was converted to temperature using the RSCM thermometer of Beyssac et al. (2002, 2003, 2007). The intrinsic error in the thermometer related to the petrological data used for calibration is 50 °C and its precision is ~15 °C (Beyssac et al. 2007). The peak pressures experienced by the metasedimentary rocks were estimated using the quartz-in-garnet (QuiG) elastic geobarometer, which uses the shift in frequency in Raman spectra from quartz grains that are completely enclosed in garnet. For QuiG geobarometry, Raman spectra were collected from polished sections (<50–100 µm thickness) using a laser power of 5–10 mW at the surface. During the Raman analysis, quartz inclusions near cracks or exposed at the surface of the thin section were avoided. The centers of quartz inclusions with diameters of ~10 µm were measured to reduce the interference from the host garnet (Enami 2012). Frequency shifts in the quartz Raman spectra were estimated using  $\Delta\omega_1$  values ( $\Delta\omega_1 = \omega_1(standard) - \omega_1(sample)$ , where  $\omega_1(standard)$  and  $\omega_1(sample)$  are the difference in the position of the peaks near 464 and 205 cm<sup>-1</sup> in the standard and sample spectra). The  $\Delta\omega_1$  values were used to estimate pressures, employing the P-T relationship proposed by Kouketsu et al. (2014b).

#### IV. RESULTS

## A. Tomisato serpentinite and reaction zone

The Tomisato ultramafic body is exposed over an area of  $\sim 20 \times 30$  m across the Dozangawa river (Fig. 1c). The long axis of the serpentinite body is subparallel to a mineral lineation in the surrounding pelitic schists. The ultramafic body contacts with the pelitic schist along the northern boundary, whereas it contacts with the mafic rock along the southern boundary (Fig. 1c). These boundaries are clearly recognized in the outcrop (Fig. 1c). Detailed descriptions of serpentinite from the Tomisato ultramafic body have been presented by Hirauchi et al. (2021). Between the serpentinite and pelitic schist, a sequence of metasomatic reaction zones (~100 cm thick) is developed in both the metapelite and ultramafic rock (Fig. 2a), comprising pelitic schist, albite schist, muscovite rock, chlorite rock, tremolite schist, talc schist, talc+serpentine rock, and serpentinite. The boundary between the pelitic and albite schists is not clear in the outcrop (Fig. 2a). Foliation in the muscovite and chlorite rocks is not clear in the outcrop, and the boundary between the albite schist and the muscovite rock is sharp with no evidence of faulting (Fig. 2b). In contrast, faults are observed along the boundaries between (i) the chlorite rock and the tremolite schist, and (ii) the tremolite and talc schists (Fig. 2a). The talc schist occurs as lenses between the tremolite schist and talc+serpentine rock (Fig. 2a). In the talc+serpentine rock, dark green angular serpentinite clasts are cut by a network of talc veins (Fig. 2c). With increasing distance from the boundary with the metapelite, the proportion of talc veins decreases and that of the light green serpentine matrix increases. The serpentinite located far from the pelitic schist has a typical block-in-matrix structure, composed of dark green massive serpentine blocks enclosed in a light green serpentine matrix (Fig. 2d; Hirauchi et al. 2021). A pervasive branching talc vein network is developed in the talc+serpentine rock (Fig. 2c, S1). The albite schist contains several veins that intersect the foliation at a high angle (>60°; Fig. 2b). The muscovite rock and the chlorite rock contain no visible veins in the field (Fig. 2b). We collected 21 samples across the reaction zone (Table 1). Mineral assemblage in each lithology and representative mineral phase map were shown in Fig. 3a and Fig. 3b-f, respectively.

The pelitic schist is composed of quartz (25 vol.%) + plagioclase (31 vol.%) + muscovite (29 vol.%) + epidote (3 vol.%) + garnet (2 vol.%) + chlorite (5 vol.%) + amphibole (<1 vol.%) with accessory titanite, tourmaline, apatite, and

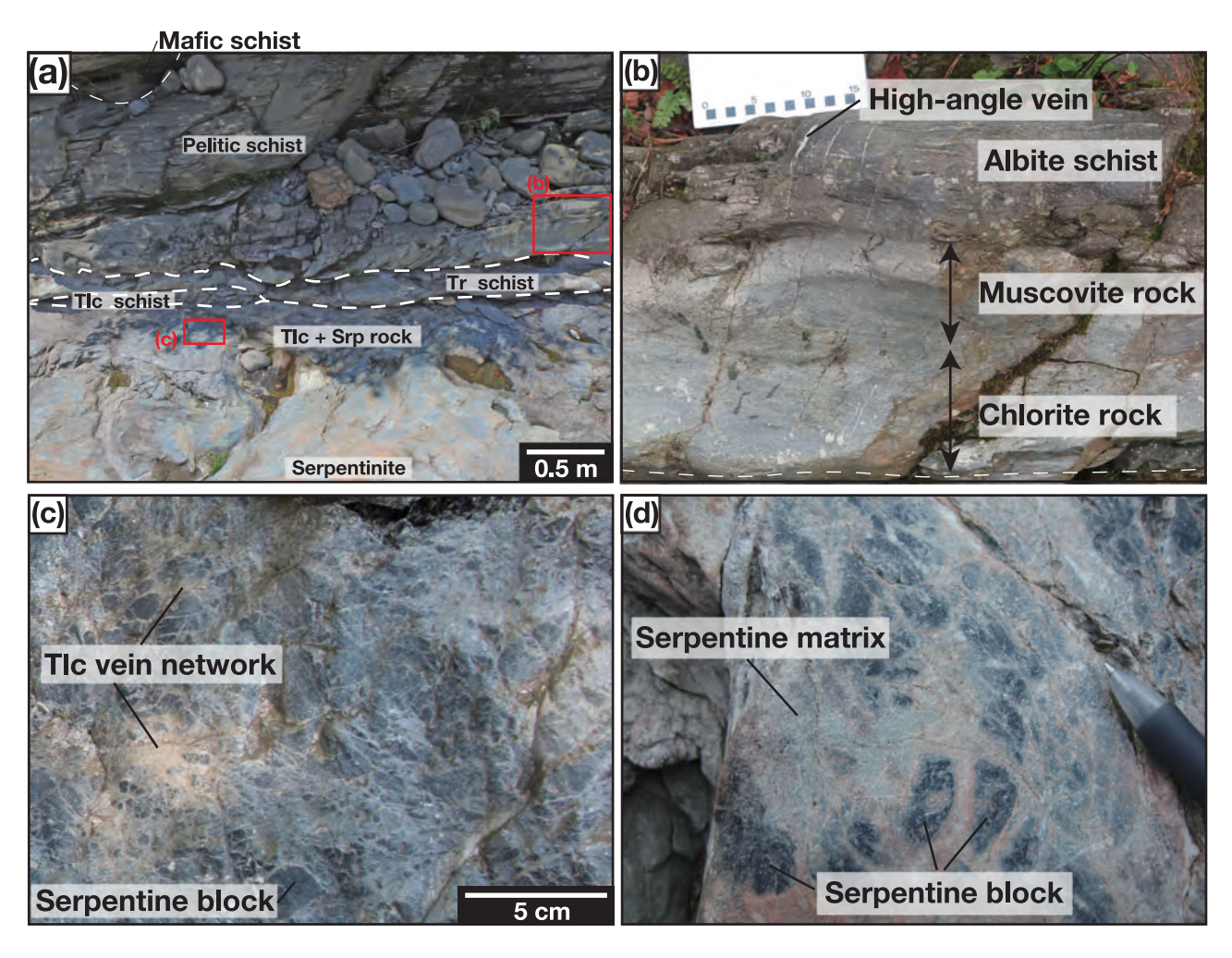


FIG. 2. (a) Photograph of the pelitic schist–ultramafic rock boundary. The white dashed lines indicate faults, and red rectangles show the locations of (b) and (c). (b) Photograph of the albite shist, muscovite rock, and chlorite rock. (c) Photograph of the talc+serpentine rock. (d) Photograph of the less-metasomatized serpentinite located far from the pelitic schist, composed of serpentine blocks and matrix.

rutile (Figs. 3a-b, 4a; Table 2). The schistosity is defined by the shape preferred orientation of chlorite and muscovite, and the lineation is defined by the shape preferred orientation of amphibole. Quartz and plagioclase occur in the granoblastic matrix (~0.1–1 mm). Garnet occurs in the pelitic schist as subhedral, partially resorbed porphyroblasts (0.5–1 mm; Figs. 3b, 4a; Fig. S2a, b), and contain inclusions of quartz, epidote, and titanite. Garnet crystals experienced less chloritization compared to those in the albite schist and the muscovite rock and have a range of fracture densities, from unfractured (Fig. S2b) to moderately fractured (Fig. 3a; Fig. S2a, b). Amphibole occurs as acicular grains (0.1–1 mm), with c-axes commonly aligned parallel to the foliation and lineation (Fig. S3a-b). Epidote occurs as idiomorphic grains (~0.1 mm). Chlorite occurs as greenish flaky crystals and as pseudomorphs after garnet. Biotite has not been observed. CM occurs mainly as inclusions in albite and garnet, or forms CM-rich layers that are 0.1-0.5 mm thick and oriented subparallel to the foliation (Fig. S2a, b).

The albite schist is ~30 cm thick and composed of plagioclase (60–80 vol.%) + chlorite (7–13 vol.%) + stilpnomelane (2–6 vol.%) with minor quartz, amphibole, muscovite, apatite, garnet, and titanite (Figs. 3a, c, d, 4b, S4a, S5a, b; Table 2). The schistosity is defined by the shape preferred orientation of chlorite, amphibole, and muscovite. Plagioclase occurs in the granoblastic matrix. CM occurs in plagioclase cores, but not in rims (Fig. S5a, b). Quartz also occurs in the granoblastic matrix but sometimes occurs locally as inclusions in plagioclase. Garnet (~0.2 mm) is rare in the albite schist due to extensive chloritization that has formed pseudomorphs (Fig. 4b; Fig. S5a, b). Amphibole occurs as acicular grains (0.2–0.5 mm) that are colorless under the microscope, and is commonly elongated parallel to the foliation; however, it is absent in some samples. Stilpnomelane occurs as brownish acicular and flaky crystals (~0.5 mm) with random orientations filling space in the granoblastic plagioclase matrix. Some amphibole rims are cut by stilpnomelane crystals (Fig. S3c, d), suggesting that stilpnomelane growth postdated that of amphibole.

The high-angle veins in the albite schist are lenticular with widths of ~0.5–10.0 mm (Fig. 2b). The thick high-angle veins (~10 mm in width) are composed of quartz with minor stilpnomelane. Quartz grains are commonly euhedral to subhe-

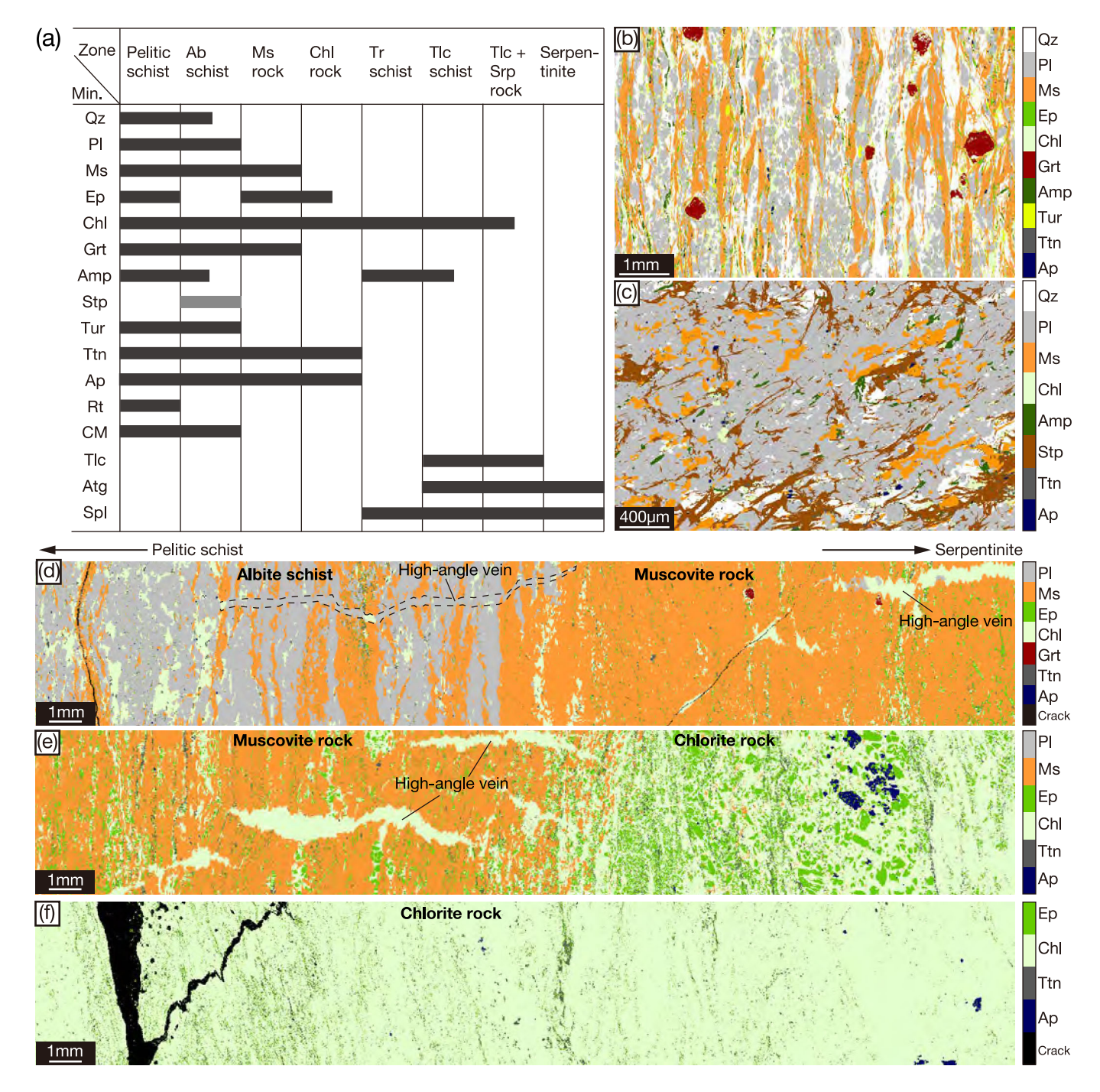


FIG. 3. (a) Mineral assemblages across the pelitic schist—ultramafic rock boundary. The black bar indicates the phase that present at the peak P–T, whereas the gray bar indicates the phase formed at retrogression stage. (b–f) Representative mineral distribution maps. (b) Mineral distribution map for the pelitic schist (sample 150808S1). (c) Mineral distribution map for the albite schist (sample 150808S2). (d) Mineral distribution map at interface of albite schist (sample 170808S1a\_up) and muscovite rock (sample 170808S1a\_low). (e) Mineral distribution map at interface of muscovite rock (sample 170808S1b\_up) and chlorite rock (sample 170808S1b\_low). (f) Mineral distribution map of chlorite rock (sample 170808S1c). The left and right sides of Fig. 3d–f are the pelitic schist side and serpentinite side, respectively. Mineral abbreviations are after Whitney and Evans (2010).

dral (0.1–10.0 mm). Stilpnomelane occurs as brownish acicular and flaky crystals, as also observed in the host rock. By contrast, the thin (~0.5 mm in width) high-angle veins consist predominantly of albite with minor chlorite (Fig. 3d). The

albite crystals in the veins are optically continuous with wall rock grains of the same mineral and are elongated with long axes perpendicular to the vein wall. The chlorite in the veins is greenish under plane-polarized light. The muscovite rock

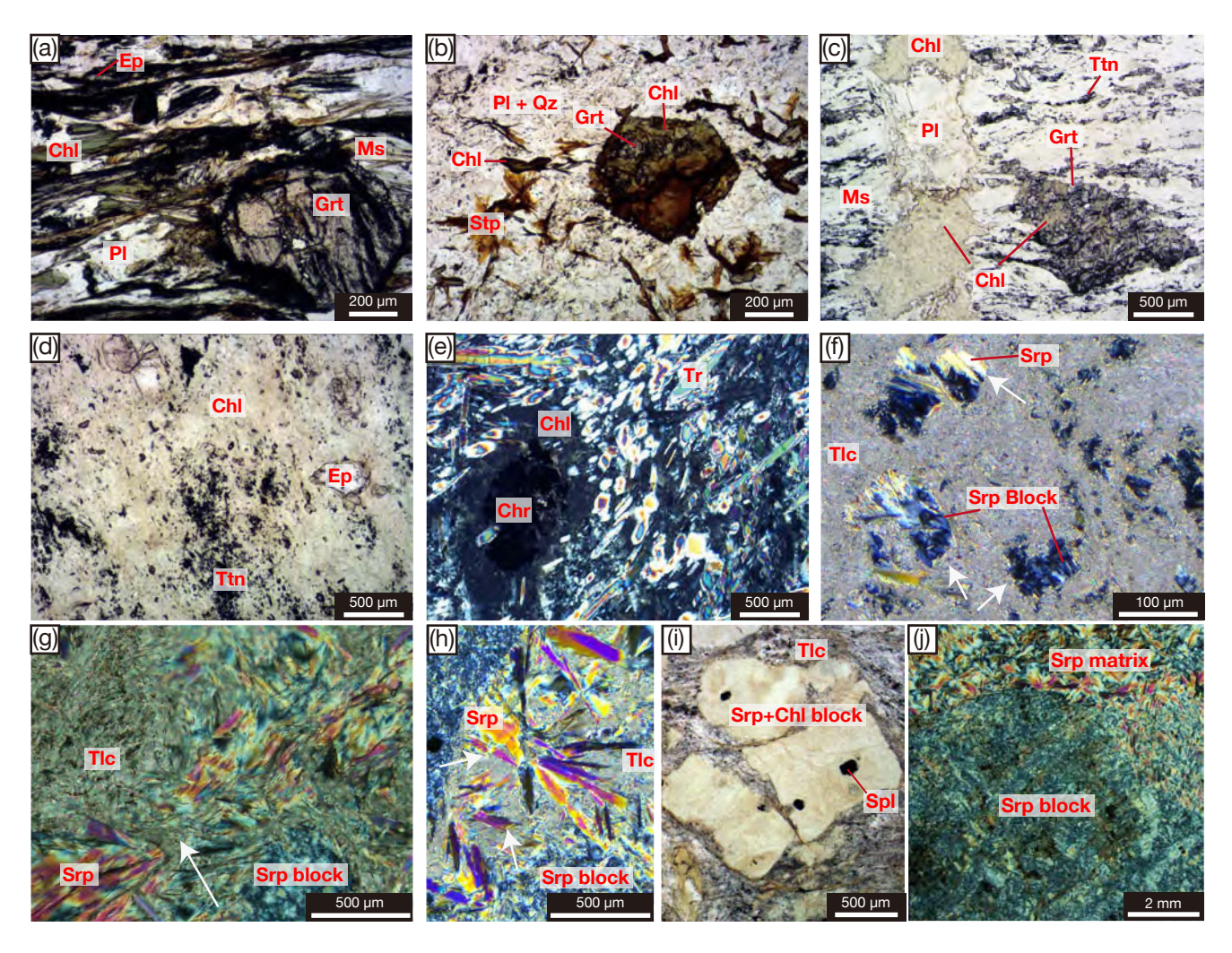


FIG. 4. Photomicrographs of rocks from the Tomisato area. (a) Pelitic schist, (b) albite schist, (c) muscovite rock, and (d) chlorite rock (all under plane-polarized light). (e) Tremolite schist under cross-polarized light. (f) Talc schist under cross-polarized light. Serpentine occurs as patches in the talc matrix. Both elongated serpentine and block serpentine are overprinted by talc (as indicated by white arrow). The elongated serpentine is relict of matrix serpentine in the serpentinite. (g) Talc+serpentine rock under plane-polarized light. Serpentine is replaced locally by chlorite. The talc overprints the elongated serpentine (as indicated by white arrow). (h) Talc+serpentine rock under plane-polarized light. The elongated serpentine overprints talc (as indicated by white arrow). (i) Talc+serpentine rock under plane-polarized light. (j) Serpentinite under cross-polarized light.

is ~20 cm thick and composed of muscovite (75–84 vol.%) + epidote (6-10 vol.%) + garnet (<1 vol.%) + chlorite (8-13 vol.%), with accessory titanite, apatite, and rutile, and contains veins of chlorite + plagioclase oriented at a high angle to the foliation (Figs. 3a, d, e, 4c; Table 2). The boundary between the albite schist and muscovite rock is sharp under the microscope (Fig. 3d). The schistosity of the muscovite rock is defined by the shape preferred orientation of muscovite, chlorite, epidote (0.1–0.5 mm), and titanite (<0.1 mm; Fig. 4c), although this is not clear in the field (Fig. 2b). CM has not been observed in the muscovite matrix, but occurs locally as inclusions in garnet. Garnet crystals are anhedral, 0.2-0.5 mm in diameter, and extensively resorbed, with portions of their rims being replaced by chlorite (Fig. S6a). Crystals located near veins are strongly fractured and replaced by chlorite (Fig. 4c; Fig. S6b, c). Garnet is boudinaged in one sample (150808S1a\_low), with the segments between boudins being filled with plagioclase and chlorite (Fig. S6c).

High-angle sigmoidal veins of ~1 mm in width occur in the muscovite rock (Figs. 3d, e, 4c, S6b, c), although they are not clear in the field (Fig. 2b). The veins consists of chlorite + albite in areas close to albite schist (Figs. 3d, 4c) and of chlorite in areas close to chlorite rock (Fig. 3e). The chlorite in the veins is greenish under plane-polarized light (Figs. 4c, S6b), and the albite crystals in the veins (~0.5 mm) are anhedral with wormy rims (Figs. 4c, S6b).

The chlorite rock is ~20 cm thick and composed predominantly of chlorite (70–98 vol.%) along with epidote (<1–22 vol titanite, and apatite (Figs. 3a, e, f, 4d; Table 2). The boundary between the muscovite and chlorite rock is sharp under the microscope (Fig. 3e). The schistosity is defined by the mineralogical layering and weakly aligned chlorite, al-

though this is not clear in the field (Fig. 2b). The chloritedominated zone lacks CM and garnet. The chlorite is dark gray under cross-polarized light and occurs as equigranular grains elongated parallel to the foliation. Subhedral epidote (0.1-1.0 mm), apatite, and fine-grained titanite crystals occur in the chlorite matrix (Figs. 3e, 4d). Epidote was observed in the chlorite rock adjacent to the muscovite rock but has not been observed in the chlorite rock adjacent to the tremolite schist (Fig. 3e, f). The tremolite schist is ~20 cm thick and composed of spinel crystals (<1 vol.%) of ~1.0 mm in diameter enclosed in a matrix of tremolite (67 vol.%) and chlorite (33 vol.%; Figs. 3a, 4e, S4b, S7a, b; Table 2). Tremolite occurs as aggregates of small idiomorphic crystals and as large, randomly orientated acicular crystals (0.1 - 1.0 mm; Figs. 4e,S7a, b). Chlorite is olive or dark green under plane-polarized light. Spinel has been mostly replaced by chlorite (Fig. S7a). Serpentine was not observed in the tremolite schist.

The talc schist is ~30 cm thick and composed of spinel (<1 vol.%; ~1 mm) enclosed in a talc (64–79 vol.%) matrix, along with chlorite (21–34 vol.%) and occasional tremolite patches (Figs. 3a, 4f, S4c, S7c, d; Table 2). Talc crystals are elongated parallel to the foliation (Fig. S7c, d). The chlorite is dark blue under cross-polarized light and occurs as patchy crystals. The talc + chlorite matrix contains blocks composed of equigranular aggregates of serpentine and elongated serpentine crystals (Fig. 4f).

The talc+serpentine rock is composed of talc (13-42 vol.%) + serpentine (antigorite; 50–86 vol.%) with minor spinel (Figs. 3a, 4g–i, S4d; Table 2). Talc veins are associated with elongated coarse-grained serpentine (Fig. 4g–i). The talc overprints the elongated serpentine (Fig. 4i), and sometimes the elongated serpentine overprint talc (Fig. 4h). The modal abundance of the serpentine blocks decreases from the serpentinite towards the talc schist. Serpentine + chlorite + spinel blocks (1-10 mm) are separated by talc veins (Fig. 4i), and the talc+serpentine rock grades into talc schist that is devoid of serpentine blocks.

The serpentinite is composed of serpentine (antigorite; >95 vol.%) with minor spinel (Figs. 3a, 4j; Table 2). Serpentine blocks consist of aggregates of equigranular grains. The serpentine in the matrix occurs as aggregates of coarse (<1 mm) elongated grains (Fig. 4j). Raman spectra show that the serpentine in both the blocks and matrix is antigorite. No relict olivine occurs in the serpentinite. The lack of orthopyroxene, clinopyroxene, and their pseudomorphs suggests that the protolith was a dunite. Spinel (~1 mm) and pentlandite are observed as minor phases; spinel grains are observed only in the serpentine blocks, whereas pentlandite grains are observed only in the matrix.

## B. Mineral cheimstry

Representative mineral compositions are listed in Table 3.

# 1. Plagioclase

Plagioclase crystals in the pelitic schist, albite schist, and bleached rock have similar compositions, close to pure albite  $[X_{Ab} = \text{atomic Na/(Na + Ca)} = 0.99].$ 

#### 2. Epidote

Epidote crystals in the pelitic schist, albite schist, muscovite rock, and chlorite rock are clinozoisite. The  $X_{Pst}$  [atomic Fe<sup>3+</sup>/(Fe<sup>3+</sup> + Al)] values of the epidote are 0.06–0.23.

#### 3. Garnet

Compositional zoning was observed in garnet crystals in the pelitic schist. Garnet  $X_{\rm Sps}$  [atomic Mn/(Fe + Mn + Mg + Ca)] values decrease and  $X_{\rm Prp}$  values increase from cores ( $X_{\rm Sps}=0.43$ ,  $X_{\rm Prp}=0.02$ ) to rims ( $X_{\rm Sps}=0.10$ ,  $X_{\rm Prp}=0.05$ ; Fig. 5a, b). Fe contents increase monotonously from cores ( $X_{\rm Alm}=0.36$ ) to rims ( $X_{\rm Alm}=0.62$ ; Fig. 5a, b). Ca contents increase from cores ( $X_{\rm Grs}=0.26$ ) to the middle parts of the crystals ( $X_{\rm Grs}=0.36$ ), then decrease towards the rims ( $X_{\rm Grs}=0.27$ ; Fig. 5a, b).

In the muscovite rock, the  $X_{\rm Sps}$  values of the garnet crystals decrease from cores (0.30) to the inner rims (0.15), then decrease further in the outer rims (0.15; Fig. 5a, c). The  $X_{\rm Prp}$  and  $X_{\rm Alm}$  values increase from cores ( $X_{\rm Prp} = 0.02$ ,  $X_{\rm Alm} = 0.36$ ) to the inner rims ( $X_{\rm Mg} = 0.04$ ,  $X_{\rm Alm} = 0.51$ ), then decrease in the outer rims ( $X_{\rm Prp} = 0.02$ ,  $X_{\rm Alm} = 0.40$ ; Fig. 5a, c).  $X_{\rm Grs}$  values decrease systematically from cores (0.32) to the inner rim (0.26; Fig. 5a, c). At the outer rim, they show a discontinuous increase ( $X_{\rm Grs} = 0.40$ ).

#### 4. Chlorite

Chlorite compositions were estimated by normalizing to 14 oxygens, and show a wide range (Fig. 6a, b). The chlorite in the pelitic and albite schists yields similar compositions, with Si contents of 2.65–2.92 apfu, Al(IV) contents of 1.07–1.34 apfu, and atomic Mg/(Mg + Fe) ratios of 0.35–0.48. The compositions of most of the chlorite crystals in the muscovite rock are similar to those in the pelitic schists [Si = 2.65-2.83 apfu]Al(IV) = 1.16-1.35 apfu, Mg/(Mg + Fe) = 0.40-0.48], butthose close to the chlorite rock have elevated Mg/(Mg + Fe) ratios (0.50–0.61; Fig. 6a). Chlorite crystals in the chlorite rock have high Mg/(Mg + Fe) ratios (0.68–0.76). Overall, chlorite XMg values increase with distance from the pelitic schists (i.e., with decreasing distance to the tremolite schist; Fig. S8). Chlorite crystals in the tremolite schist, talc schist, and talc+serpentine rock are supersilic (Si >3.0 apfu) with elevated Mg/(Mg + Fe) ratios (0.82–0.88; Fig. 6a).

The chlorites can be divided two clusters on the basis of their Cr and Mn contents: low-Cr (<0.05 apfu), high-Mn (0.01–0.07 apfu) chlorite, and high-Cr (0.01–0.35 apfu), low-Mn (0.01–0.02 apfu) chlorite (Fig. 6b). The chlorite in the

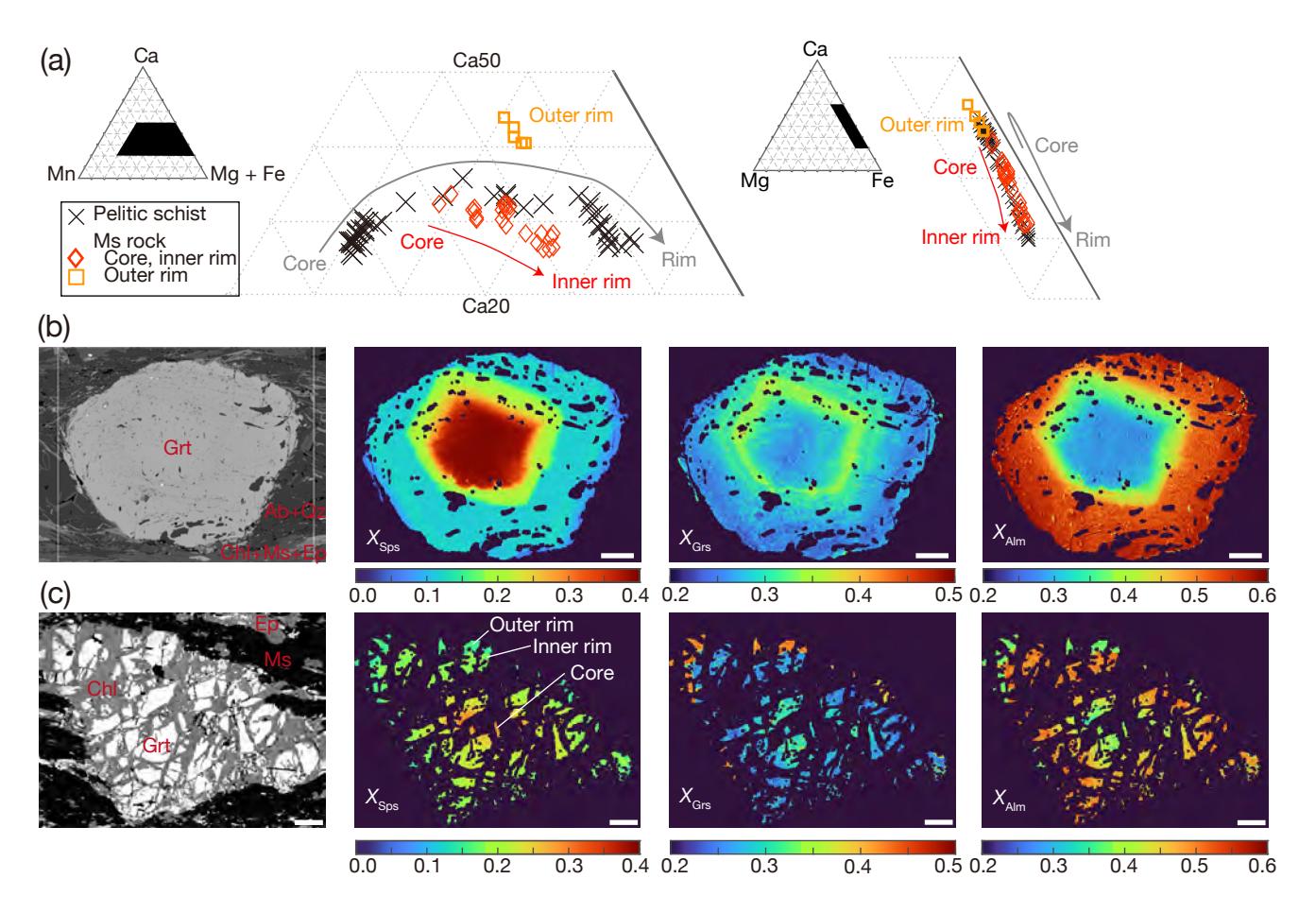


FIG. 5. (a) Ca–Mn–Mg+Fe and Ca–Mg–Fe ternary plots of garnet in the pelitic schist and muscovite rock. (b–c) BSE images and quantitative X-ray maps of garnet crystals from (b) the pelitic schist and (c) the muscovite rock. Mineral abbreviations are after Whitney and Evans (2010).

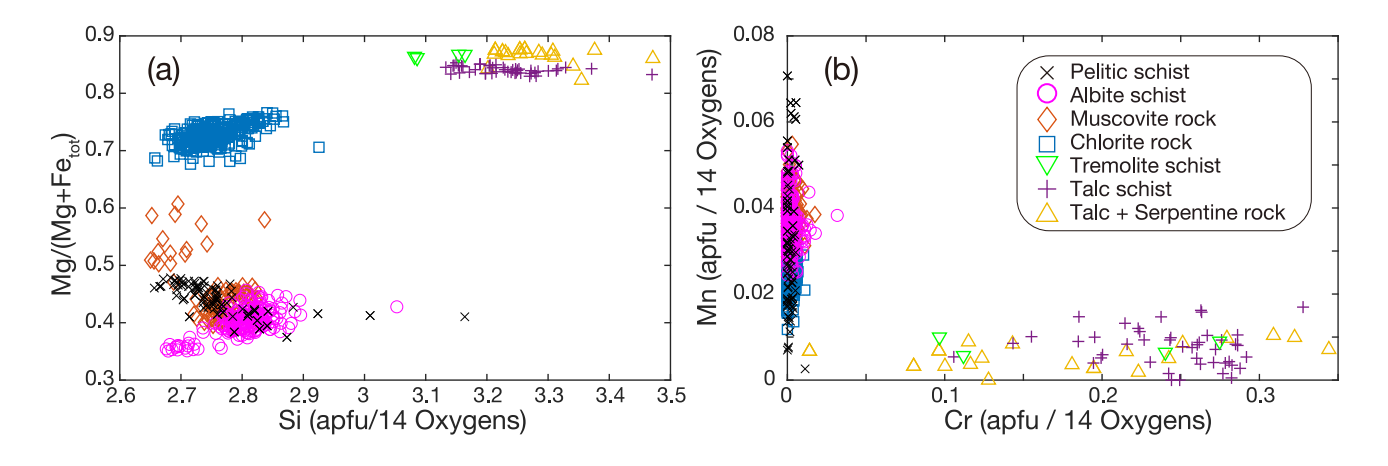


FIG. 6. Composition of chlorite crystals. (a) Si content versus Mg/(Mg + Fetot) ratio. (b) Mn versus Cr contents.

pelitic schist, albite schist, muscovite-rich rock, and chlorite rock are low-Cr, high Mn chlorite, whereas those in the tremolite schist, talc schist, and talc+serpentine rock are high-Cr, low-Mn chlorite.

# 5. Amphibole

Amphibole crystals in the pelitic schist are calcic amphibole and show compositional zoning, with cores mostly of edenite, magnesio-, or ferro-hornblende and rims of actinolite (Fig. S3a, b). Amphibole crystals in the albite schist are also

calcic amphibole, with magnesio- or ferro-hornblende cores and actinolite rims (Fig. S3c, d).

Amphibole crystals in the tremolite schist and talc schist are calcic amphibole, and their compositions ( $X_{\rm Mg} = 0.85-0.91$ ) indicate that they are actinolite and tremolite. The amphibole is crosscut by later stilpnomelane crystals (Fig. S3c, d). The Na contents in the M4 site and Al contents in the T1 site in the amphibole crystals in the pelitic schist decreased from 0.31 to 0 and 1.40 to 0.06, respectively, from amphibole core to rim (Fig. S3e).

#### 6. Talc

The compositions of the talc in talc schist and talc+serpentine rock are similar, with  $X_{\rm Mg}$  values of 0.93–0.95.

#### 7. Serpentine (Antigorite)

Serpentine compositions were estimated by normalizing to seven oxygens. Serpentine from the blocks in the serpentinite far from the pelitic schist has low Al contents (<0.05 apfu) and  $X_{\rm Mg}$  values of 0.91–0.96 (Fig. 7a). The serpentine blocks in the talc schist and talc+serpentine rock have lower  $X_{\rm Mg}$ values (0.80-0.85 and 0.83-0.92, respectively; Fig. 7a) and higher Al contents (0.05–0.50 apfu; Fig. 7b) than the blocks in the serpentinite. The composition of serpentine blocks in the serpentinite can be explained by a combination of the dioctahedral substitution  $[3R^{2+}(2R^{3+}\Box)^{-1}(R^{3+} \text{ is } Fe^{3+} \text{ or } Al^{3+})]$ and the mixing with talc (Fig. 7b). By contrast, the composition of serpentine blocks in the talc schist can be explained by Tschermak substitution [AlAl(Mg, Fe<sup>2+</sup>)<sup>-1</sup>Si<sup>-1</sup>; Fig. 7b]. The composition of serpentine blocks in the talc+serpentine rock can be explained by a combination of the Tschermak substitution, the dioctahedral substitution, and the mixing with talc (Fig. 7b). These observations suggest the occurrence of fine talc intergrowths within the analytical spots of the serpentine block in the talc+serpentine rock and the serpentinite (e.g., Katayama et al. 2010; Beard and Frost 2017). The serpentine blocks have lower  $X_{\text{Mg}}$  values and higher Al contents where located closer to the pelitic schist, suggesting that the infiltration of metasomatic fluid and dissolution-precipitation modified the composition of the serpentine blocks close to the boundary.

The talc+serpentine rock and serpentinite have a serpentine matrix. The matrix serpentine in the serpentinite located far from the pelitic schist has low Al contents (<0.08 apfu) and  $X_{\rm Mg}$  values of 0.86–0.98, whereas that in the talc+serpentine rock is slightly enriched in Al (0.02–0.14 apfu) and has low  $X_{\rm Mg}$  values (0.84–0.96; Fig. 7c). The serpentine in the matrix shows compositional zoning, from high- $X_{\rm Mg}$  (0.96) cores to low- $X_{\rm Mg}$  (0.90) rims. The compositions of the serpentine matrix in the serpentinite can be explained by a combination of the dioctahedral substitution and the mixing with talc (Fig. 7d), while those in the talc + serpentine rock can be explained

by a combination of the dioctahedral substitution and the mixing with talc (Fig. 7d). The fine talc intergrowths would exist within the analytical spots of the serpentine matrix in both the talc+serpentine rock and the serpentinite.

#### 8. Spinel

The spinel composition was estimated by normalizing to seven oxygens and five cations. Spinel crystals in the tremolite schist, talc schist, and talc+serpentine rock is chromite with atomic Cr/(Cr + Al) ratios of 0.96–0.99 and  $Mg/(Mg + Fe^{2+})$  ratios of 0.01–0.04. Spinel crystals in the serpentinite have spinel cores, ferritchromite mantles, and magnetite rims (Hirauchi et al. 2021).

#### C. Whole-rock compositions of the reaction zone

A summary of the whole-rock chemistry is provided in Table 4. In a transect across the reaction zones, whole-rock SiO<sub>2</sub> contents decrease from 65 to 28 wt.% from the pelitic schist to the albite schist, muscovite rock, and chlorite rock, and then increase in the tremolite schist and talc schist (48–56 wt.%) before decreasing again in the talc+serpentine rock and serpentinite to 42 wt.% (Fig. 8). The Al<sub>2</sub>O<sub>3</sub> contents of the pelitic schist, albite schist, muscovite rock, and chlorite rock (15–29 wt.%) are higher than those of the tremolite schist, talc schist, talc+serpentine rock, and serpentinite (<5 wt.%). The Fe<sub>2</sub>O<sub>3</sub> contents decrease from 5.0 wt.% in the pelitic schist to 3.2–4.2 wt.% in the albite schist, then increase to 7.2 wt.% in the muscovite schist and 17.4–18.0 wt.% in the chlorite rock (Fig. 8). The Fe<sub>2</sub>O<sub>3</sub> contents of the tremolite schist, talc schist, talc+serpentine rock, and serpentinite are relatively consistent (4.9–7.8 wt.%; Fig. 8). The MgO contents of the pelitic schist, albite schist, and muscovite rock are low (1.7–3.5 wt.%), and increase monotonically from the chlorite rock (18.7–20.9 wt.%) to the serpentinite (35.9–37.9 wt.%; Fig. 8). The Na<sub>2</sub>O contents of the albite schist (5.4–9.3 wt.%) are higher than those of the pelitic schist (3.5 wt.%) and other lithologies (0.0-0.4 wt.%; Fig. 8). The K<sub>2</sub>O contents decrease from 2.8 wt.% in the pelitic schist to 1.7–1.9 wt.% in the albite schist, then increase to 8.6 wt.% in the muscovite schist, and are <0.1 wt.% from the chlorite rock to the serpentinite (Fig. 8). The CaO contents decrease from 1.1 wt.% in the pelitic schist to 0.7 wt.% in the albite schist, then increase to 1.5 wt.% in the muscovite rock (Fig. 8). The chlorite rock yields CaO contents of 0.9-2.1 wt.%, and the tremolite schist have CaO contents of 6.9 wt.%. The talc schist, talc+serpentine rock, and serpentinite have CaO contents of 0.1-0.2 wt.%.

Ni, Cr, and Zr content showed a marked contrast between lithologies; Ni content of the pelitic schist, albite schist, muscovite rock, and chlorite rock are 20-62 mg/kg, whereas those of tremolite schist, talc schist, talc+serpentine rock, and serpentinite are significantly higher (1718 – 2595 mg/kg; Table 4); Cr content of the pelitic schist, albite schist, muscovite rock, and chlorite rock are 18-101 mg/kg, whereas those of

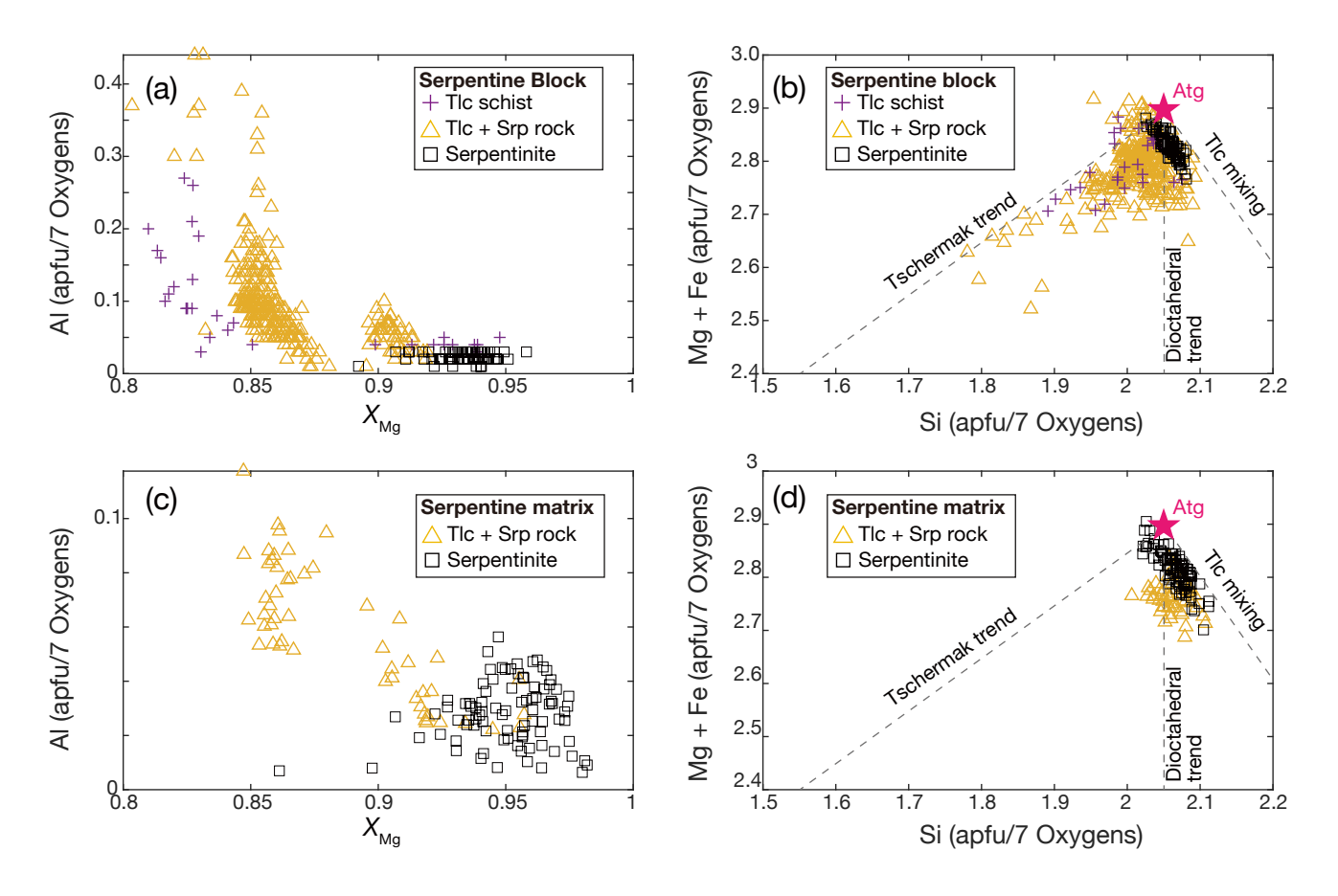


FIG. 7. (a, b) Composition of the serpentine blocks in the talc schist, and serpentinite. (c, d) Composition of serpentine matrix in the talc+serpentine rock and serpentinite. Pink stars in (b) and (d) indicate the composition of pure antigorite.

tremolite schist, talc schist, talc+serpentine rock, and serpentinite are significantly high (1713 – 9286 mg/kg; Table 4); Zr content of the pelitic schist, albite schist, muscovite rock, and chlorite rock are 165 - 274 mg/kg, whereas those of tremolite schist, talc schist, talc+serpentine rock, and serpentinite are under detection limit ( $<\sim$ 10 mg/kg; Table 4). Bulk rock Ti/Cr mass ratio of the pelitic schist, albite schist, muscovite rock, and chlorite rock are 69.90 - 131.38, whereas those of tremolite schist, talc schist, talc+serpentine rock, and serpentinite are 0.00 - 0.04 (Table 4).

The trace element contents of the pelitic schist, albite schist, muscovite rock, and chlorite rock (Fig. 9a) are generally higher than primitive mantle (PM) values, except for Ni and Cr. The Cs, Rb, and Ba contents are variable. The chlorite rock yielded Cs contents of  $1{\text -}10 \times \text{PM}$ , and the pelitic schist, albite schist, and muscovite rock yielded Cs contents of  $>100 \times \text{PM}$ . The chlorite rock yielded Rb contents similar to those of PM, whereas Rb is enriched in the pelitic schist ( $200 \times \text{PM}$ ), albite schist ( $6{\text -}100 \times \text{PM}$ ), and muscovite rock ( $500 \times \text{PM}$ ). The chlorite rock yielded Ba contents of  $0.1{\text -}1 \times \text{PM}$ , whereas Ba is enriched in the pelitic schist ( $60 \times \text{PM}$ ), albite schist ( $10{\text -}60 \times \text{PM}$ ), and muscovite rock ( $600 \times \text{PM}$ ). The REE contents of the pelitic schist, albite schist, muscovite rock, and chlorite rock (Fig. 9b) are >10 times higher than chondritic

values, with the light REEs (LREEs) being enriched relative to the heavy REEs (HREEs;  $La_{CN}/Lu_{CN} = 6.8-10.4$ ). The HREE patterns of the albite schist and muscovite rock are flat, but the HREEs in the chlorite rock are depleted relative to the middle REEs (MREEs). Negative Eu anomalies were observed in the pelitic schist, albite schist, muscovite rock, and chlorite rock (Eu/Eu\* = 0.43–0.93; Table 3).

The tremolite schist, talc schist, talc+serpentine rock, and serpentinite (Fig. 9c) are enriched in Cs relative to PM (<18 × PM). Enrichment in Pb was observed in the tremolite rock, one sample of talc+serpentine rock (150808S8), and serpentinite. U ( $<5 \times PM$ ) and Th ( $<3 \times PM$ ) are slightly enriched in the tremolite rock, one talc schist sample (150808S7), and the talc+serpentine rock. Sr contents are close to PM values, but low in the talc schist, talc+serpentine rock, and serpentinite (<0.04 PM). The tremolite rock, talc schist, talc+serpentine rock, and serpentinite commonly weak LREE enrichment relative to the MREEs and HREEs on chondrite-normalized REE diagrams ( $La_{CN}/Lu_{CN} = 2.8-6.2$ ; Fig. 9d), with flat HREE patterns. The tremolite rock is enriched in MREEs relative to LREEs ( $Sm_{CN}/La_{CN} = 1.3$ ). The tremolite schist, talc schist, talc+serpentine rock, and serpentinite yield variable negative Eu anomalies (Eu/Eu\* = 0.07-0.39; Table 4).

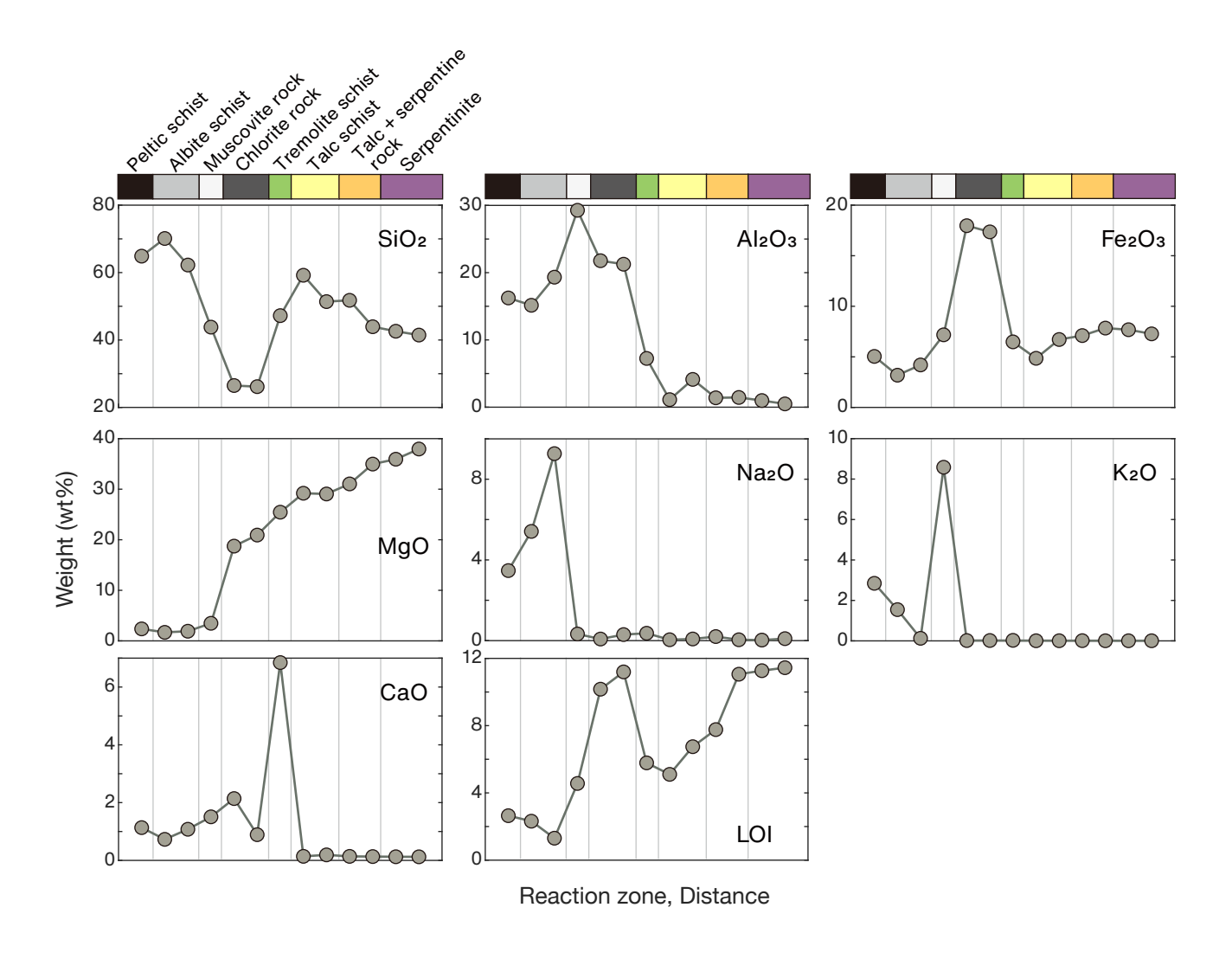


FIG. 8. Whole-rock composition across the reaction zone.

# D. Geothermometry and geobarometry

The presence of plagioclase and quartz inclusions in amphibole shows that plagioclase and quartz coexisted during amphibole growth (Fig. S3a), suggesting that the amphibole grew in equilibrium with these minerals. The horn-blende–plagioclase–quartz (HPQ) geothermometer (Holland and Blundy 1994) was applied to the amphibole in the pelitic schist. The amphibole cores and plagioclase (homogenous  $X_{Ab} = 0.99$ ) in the pelitic schist yields temperatures of 529–570 °C at 0.5–1.0 GPa (Table S1).

The Raman spectra from CM in the pelitic schist are characterized by a pronounced peak at  $1582 \text{ cm}^{-1}$  (G band) and a weak peak at  $1351 \text{ cm}^{-1}$  (D1 band; Fig. S9a). The 30 CM analyses yielded R2 ratios of 0.10-0.35. Average R2 ratio was  $0.255 \pm 0.062$  (1 standard deviation), which corresponds to  $528 \pm 28$  °C. Median was 527 °C.

The Raman spectra from 23 quartz inclusions in garnet crystals in the pelitic schist yielded  $\Delta\omega_1$  values of 4.2–9.7 with a mode at 6.0–8.0 (mean = 7.5; Fig. S9b).

#### V. DISCUSSION

# A. Original pelite-ultramafic rock boundary

The location of the original pelite–ultramafic rock boundary is a basis to understanding elemental transfer during the development of the metasomatic zones. The key observations are as follows. (i) Spinel grains occur in the tremolite-and talc-bearing rocks (Figs. 3a, 4e, i) but are absent in the pelitic schist, albite schist, muscovite rock, and chlorite rock (Figs. 3a, 4a, d). (ii) Titanite occurs in the muscovite rock (Fig. 4c), chlorite rock (Fig. 4d), albite schist, and pelitic

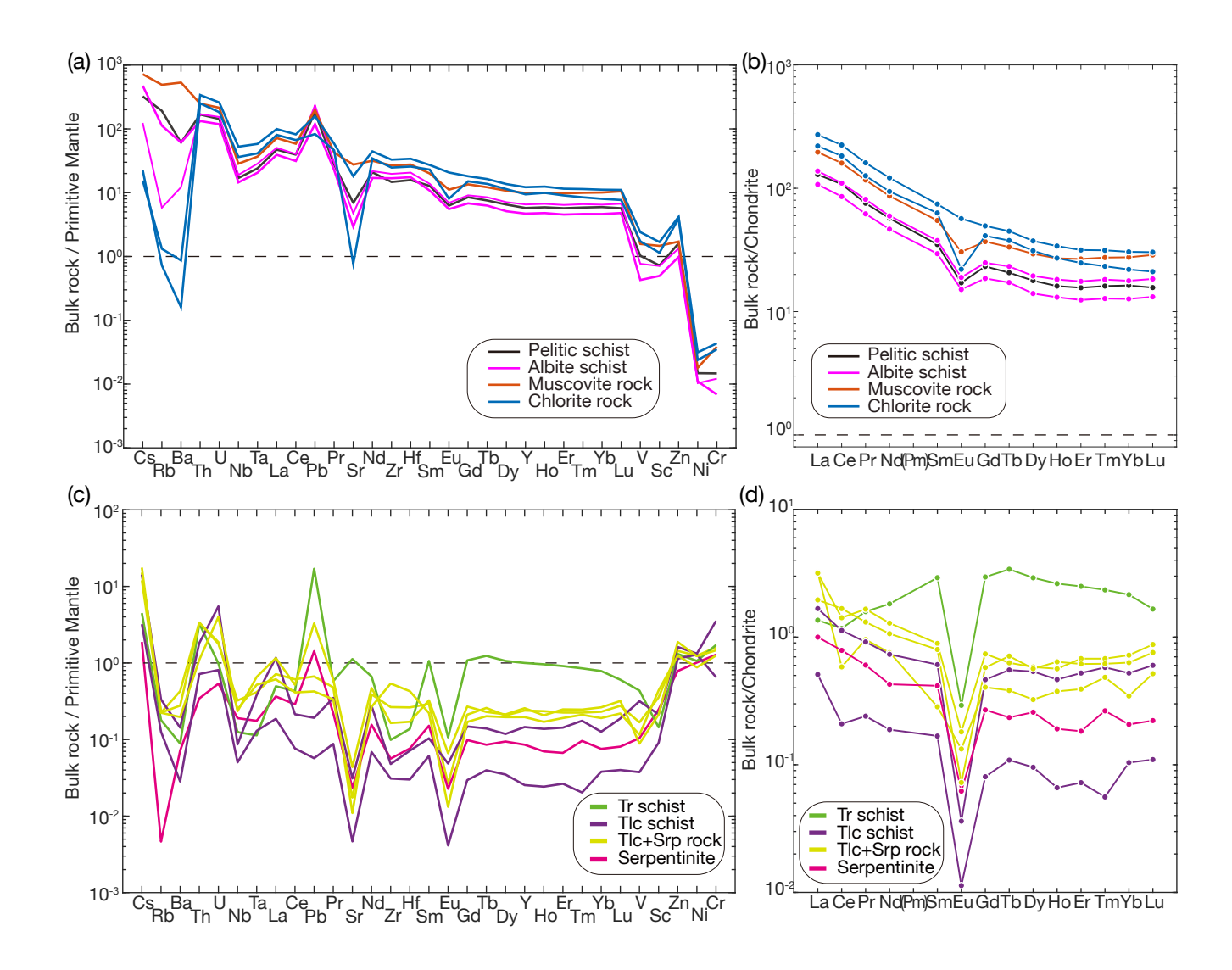


FIG. 9. (a) Trace element and (b) rare earth element patterns of the pelitic schist, albite rock, muscovite rock, and chlorite rock. (c) Trace element and (d) rare earth element patterns of the tremolite schist, talc schist, talc+serpentine rock, and serpentinite.

schist, but is absent in the tremolite and talc schists (Fig. 3a). (iii) The Cr content of chlorite in the chlorite rock is similar to that in the metapelite (92.1 and 38.5 ppm, respectively; Table 4), and lower than that in the tremolite schist, talc schist, and talc+serpentine rock (1713–9286 ppm; Table 4). These observations suggest that the original pelite–ultramafic rock boundary is located between the chlorite rock and the tremolite schist. This interpretation is consistent with the results of Okamoto et al. (2021), who observed partly- to completely-chloritized pelitic schist at the contact with serpentinite. Whole-rock Ti and Cr contents have been used to identify the pelite-ultramafic boundary at other locations (Sanford 1982; Maekawa et al. 2004). Maekawa et al. (2004) proposed that the original boundary between a pelitic schist and ultramafic rock can be identified using the whole-rock Ti

and Cr contents. Similarly, Sanford (1982) suggested that the initial boundary is marked by a discontinuity in the Ti/Cr ratio, which is also observed in our data (Table 3).

# B. Metamorphic history and timing of metasomatism

The RSCM and HPQ thermometers yield similar temperatures ( $528 \pm 28$  and 529 - 570 °C, respectively; Fig. 10a). The two estimates are consistent with each other given the calibration error of the thermometers (50 °C in both cases).

In zoned garnet crystals in the pelitic schist,  $X_{\rm Grs}$  values show an increase followed by a decrease from core to rim, as well as a decrease in  $X_{\rm Sps}$  values and an increase in  $X_{\rm Prp}$  values from core to rim (Fig. 5a, b). The zoning patterns

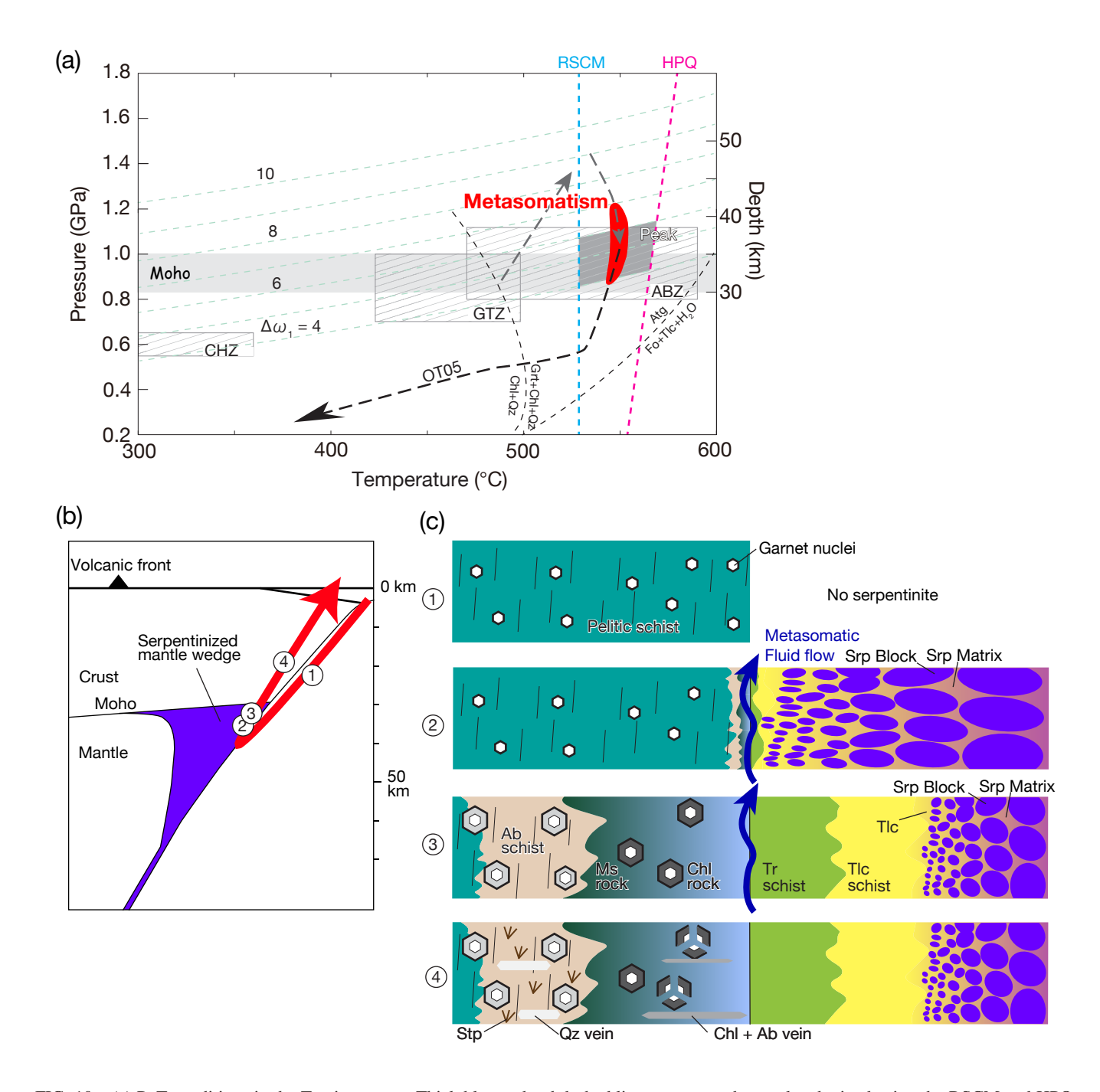


FIG. 10. (a) P-T conditions in the Tomisato area. Thick blue and red dashed lines represent the results obtained using the RSCM and HPQ thermometers, respectively. The P-T conditions of the chlorite (CHZ), garnet (GTZ), and albite (ABZ) zones are shown using black shaded rectangles (Enami 1998; Kouketsu and Enami 2011). The dashed black arrow indicates the retrograde path of the mafic schists from the Tomisato area (OT05: Okamoto and Toriumi 2005). The garnet-in reaction curve is from Inui and Toriumi (2002). (The thin green dashed lines show the P-T conditions estimated using 1 values (Kouketsu et al. 2014b). The estimated peak P-T conditions are indicated by the dark-gray area. The timing of metasomatism between pelitic schist and serpentinite are indicated by the red area. (b) Schematic illustration of a subduction zone. The number in circle corresponds to schematic illustration in (c). (c) Metamorphic history of the Tomisato ultramafic body and the timing of the metasomatism.

are typical of prograde garnet in pelitic schists from the Sanbagawa metamorphic belt (Banno et al. 1986; Enami 1998; Inui and Toriumi 2002; Uno et al. 2015), showing a prograde P-T path with the pressure peak preceding the temperature peak (i.e., heating decompression; Enami 1998; Uno et al. 2015). Kouketsu et al. (2014a) measured the  $\Delta\omega_1$  values of quartz inclusions in the typical prograde garnet from the Sanbagawa metamorphic rocks. They found that the inclusions in the intermediate part of the garnet crystals had the highest  $\Delta\omega_1$  values (i.e., the highest pressure), followed by those in the cores and then the rims, consistent with the prograde P-T path of the metamorphic rocks in the Sanbagawa belt. Therefore, within the range of observed  $\Delta\omega_1$  values (4.2-9.7 cm<sup>-1</sup>; Fig. S9b), the higher  $\Delta\omega_1$  values would correspond to the peak pressure that occurred before the peak temperature, and the lower  $\Delta\omega_1$  values would correspond to the pressures at the peak temperature. When using the lower bound of the  $\Delta\omega_1$ values (4-5 cm<sup>-1</sup>; Fig. S9b), the QuiG geobarometer yields pressures of 0.8-1.0 GPa at the peak temperature (530-570 °C). The estimated peak temperature conditions (530-570 °C) and 0.8–1.0 GPa) are higher than the typical temperatures of the GTZ (425–455 °C and 0.7–0.9 GPa; Enami et al., 1994) where the Tomisato ultramafic body is located (Fig. 10a), but the estimate is similar to the P-T estimates based on amphibole compositions in the mafic schists in the high-grade part of the GTZ (500-550 °C and 0.9-1.1 GPa; Okamoto and Toriumi 2005).

The compositional zoning of garnet can be used not only for reconstructing P-T paths, but also for estimating the timing of chemical changes induced by fluid infiltration (e.g., Erambert and Austrheim 1993; Whitney et al. 1996; Penniston-Dorland et al. 2014). In the muscovite rock, a metasomatized pelitic schist, garnet zoning is characterized by decreases in  $X_{\rm Grs}$  and  $X_{\rm Sps}$  values and an increase in  $X_{\rm Prp}$  values from the core to the inner rim, followed by a discontinuous increase in  $X_{\rm Grs}$  in the outer rim (Fig. 5a, c). The decrease in Ca contents and increase in Mg + Fe contents from garnet cores to rims in the muscovite rock are similar to the zoning from garnet mantles to rims in the pelitic schist (Fig. 5a). Therefore,  $X_{\text{Prp}}$  and  $X_{\text{Grs}}$  zoning (i) between the cores and rims of garnet in the pelitic schist and (ii) the cores and inner rims of garnet in the muscovite rock would represent garnet growth during continuous temperature increase and pressure transition from increase to decrease (Enami 1998). Moreover, the grossular-rich outer rim in garnet from the muscovite rock is absent from garnet in the pelitic schist (Fig. 5a). These observations suggest that the changes in the chemical environment due to the metasomatism of the pelitic schist and serpentinite occurred after the growth of the inner garnet rims. This indicates that the metasomatism started at nearly peak P-Tconditions (Fig. 10a)

In summary, the core to inner rim of garnet crystals in the muscovite rock grew while the rock was a pelitic schist (the protolith of the muscovite rock) prior to metasomatism, whereas the outer rim grew during the infiltration of metasomatic fluid. In this case, the timing of metasomatism is defined as the time when it reached that specific part of the rock, rather than when it began. However, several studies have found that fluid infiltration and the subsequent formation of reaction zones in subduction zones can occur over a very short period, geologically speaking (e.g., Penniston-Dorland et al. 2010; John et al. 2012; Ague 2014; Taetz et al. 2018; Beinlich et al. 2020; Mindaleva et al. 2020, 2023; Oyanagi et al. 2021), suggesting that the timing of metasomatic fluid flow and the initiation of metasomatism can be considered simultaneous on a geological timescale.

We propose that the metasomatism of the pelite and serpentinite occurred around the peak temperature conditions or the earlier-stage of exhumation (0.8–1.0 GPa and 530–570 °C; Fig. 10a-c). The high-angle chlorite ± albite veins cut the metasomatic muscovite matrix (Figs. 3d, S6b, c), suggesting that vein formation occurred after metasomatism. This interpretation is supported by previous studies of the high-angle veins that formed during the later stages of the exhumation of the Sanbagawa metamorphic belt (Toriumi and Hara 1995; Okamoto et al. 2008). Garnet crystals in the muscovite rock are strongly fractured where they occur within a few millimeters of the high-angle veins (Figs. 4c, 5c; Fig. S6a-c), suggesting localized brittle deformation of garnet related to fluid infiltration and local stress changes. In addition, the crosscutting relationships between stilpnomelane and amphibole crystals (Fig. S3c, d) suggest that stilpnomelane growth took place after the growth of the amphibole rim. The HPQ temperature estimates from the amphibole cores indicate that the amphibole grew at peak temperature conditions, suggesting that stilpnomelane growth occurred during the retrograde stage. These events would have occurred after the metasomatism between the pelitic schist and serpentinite. Faults along the boundaries between the chlorite rock and the tremolite schist, and between the tremolite and talc schists (Figs. 2a, S1) also likely developed during the later stages of exhumation.

# C. Mass transfer during development of the reaction zone

Cross-cutting relationships between the serpentinite and the products of its metasomatism suggest the following metamorphic and metasomatic sequence: (i) formation of antigorite blocks, (ii) fracturing of antigorite blocks and precipitation of a second generation of antigorite (antigorite matrix), and (iii) metasomatism of the serpentinite and pelitic schist. In the serpentinite, both serpentine blocks and elongated serpentine crystals (i.e., serpentine matrix) were observed (Fig. 4i). Around the boundary, talc overprints both serpentine blocks and elongated serpentine crystals (Fig. 4f, g). This suggests that metasomatism postdates the growth of the second generation of antigorite. However, elongated serpentine crystals also overprint the talc (Fig. 4h), implying that antigorite growth continued after metasomatism. The tremolite and talc schists are metasomatic products of the serpentinite, whereas the albite schist, muscovite rock, and chlorite rock are metasomatic products of the pelite. The sequence of reaction zones is similar to that which forms under conditions of the greenschist to epidote-amphibolite facies (Sanford 1982; Okamoto et al. 2021). At high metamorphic grades (amphibolite facies; ~600 °C and 1.0 GPa), antigorite breaks down to form talc +

forsterite in other reaction zones (Sanford, 1982).

The tremolite crystals in the tremolite rock are randomly oriented without microscopically observable rotation (Figs. 4e, S7a, b). Similarly, there are no deformation microtextures in the albite schist, muscovite rock, chlorite rock, and talc+serpentine rock. These observations suggest that the crystals grew under static conditions and their thickness (Table 1) was preserved. In contrast, the talc in the matrix of the talc schist has a strong shape-preferred orientation (Fig. S7c–d). Such a shape preferred orientation can develop even under low shear stresses, as talc is weak (Escartín et al. 2008; Collettini et al. 2009; Viti and Collettini 2009; Nagaya et al. 2020). It is therefore uncertain whether the original thickness of the talc schist has been preserved.

Element distribution and mass transfer during metasomatism are controlled by (i) the diffusion of elements between different lithologies and (ii) the removal or addition of elements by infiltrating fluids. Quantitative changes in the mass of element i can be calculated as follows (e.g., Ague 2011):

$$\Delta c_i = \frac{c_{ref}^{ori}}{c_{ref}^{alt}} \times c_i^{alt} - c_i^{ori},\tag{1}$$

where  $\Delta c_i$  is the change in the mass of element *i* per unit mass of original rock,  $c_{ref}^{ori}$  and  $c_{ref}^{alt}$  are the concentrations of immobile elements (the geochemical reference frame) in the original and altered rock, respectively, and  $c_i^{ori}$  and  $c_i^{alt}$  are the concentrations of element i in the original and altered rock, respectively. We considered a range of values for the geochemical reference frame, including upper and lower bounds, rather than using a single value. To determine statistically significant gains or losses of elements, we included the analytical error in the calculations. In addition, we assumed a 5% error in the major element contents to account for heterogeneity in the bulk rock composition. If the content of an element is within  $\pm 2\sigma$  of the geochemical reference frame, there is no conclusive evidence for its gain or loss. If the content of an element is above or below the geochemical reference frame, this suggests it was added or lost during metasomatism, respectively. Details on the selection of the geochemical reference frame and the results of the mass balance calculations are provided in the supplementary material (Supplementary Text 1).

The results of the mass balance calculations are presented in Figure 11. The albite schist (sample 150808S2) shows a  $SiO_2$  gain (+18.4 to +25.2 g/100 g protolith), whereas the other albite rock samples show no significant SiO<sub>2</sub> changes. The muscovite and chlorite rocks show significant SiO<sub>2</sub> losses (-35.3 to -41.0 and -45.4 to -52.7 g/100 g protolith, respectively), with the SiO<sub>2</sub> loss increasing in areas closer to the tremolite schist. The albite schist and muscovite rock show no significant change in Al<sub>2</sub>O<sub>3</sub>, whereas the chlorite rock (sample 150808S4) experienced Al<sub>2</sub>O<sub>3</sub> loss (-4.6 to -6.2 g/100 g protolith). Fe<sub>2</sub>O<sub>3</sub> was lost from the albite schist (-0.9 to -1.5 g/100 g protolith) but remained unchanged in the muscovite rock and increased in the chlorite rock  $(+3.2 \text{ to } +7.9 \text{$ g/100 g protolith). Little MgO was gained or lost from the albite schist and muscovite rock, but it increased in the chlorite rock (+6.3 to +13.2 g/100 g protolith), with the Fe<sub>2</sub>O<sub>3</sub> and MgO gains being greater in areas located closer to the original pelite–ultramafic rock boundary. No significant change in CaO was observed in the albite schist or muscovite rock, but the chlorite rock (sample 170808S1c) experienced a loss in CaO (-0.5 to -0.6 g/100 g protolith). The albite schist gained Na<sub>2</sub>O (+3.0 to +5.6 g/100 g protolith), whereas the muscovite and chlorite rocks lost Na<sub>2</sub>O (-3.2 to -3.4 g/100 g protolith).  $K_2O$  was lost from the albite schist (-0.9 to -2.7 g/100 g protolith) and the chlorite rock (-2.8 g/100 g protolith), but was gained by the muscovite rock (+1.8 to +2.9 g/100 g protolith).

LOI values did not show large changes in the albite schist (-1.4 to +1.5 g/100 g protolith), and they increased slightly in the muscovite rock (+0.2 to +0.4 g/100 g protolith) and increased greatly in the chlorite rock (+2.0 to +5.7 g/100 g protolith). The change in LOI values increases from the muscovite to chlorite rocks, similar to the changes in SiO<sub>2</sub>, FeO, and MgO contents, suggesting that the change in LOI values is related to the proportion of chlorite in the reaction zone. The metasomatic zones with a pelitic protolith decreased in volume, with the albite schist, muscovite rock, and chlorite rock yielding ratios of the volume of altered rock to that of the protolith  $(V_{alt}/V_{ori})$  of 0.90–1.33, 0.52–0.55, and 0.45–0.71, respectively (Table S2). The volume changes are similar to those observed in the chlorite-rich reaction zone formed after pelitic schist concomitantly with the carbonation of serpentinite  $(V_{alt}/V_{ori} = 0.66)$ ; Okamoto et al. 2021). The tremolite schist lost SiO<sub>2</sub> (-5.9 to -14.5 g/100 g protolith; Fig. 11). One of the talc schist samples had a large gain in SiO<sub>2</sub> (+76.3 to +238.3 g/100 g protolith) and the other lost SiO<sub>2</sub> (-0.5 to -19.4 g/100 g protolith). The talc+serpentine rocks lost SiO<sub>2</sub> (-18.5 to -29.0 g/100 g protolith). Al<sub>2</sub>O<sub>3</sub> increased throughout the metasomatic zones with serpentinite protoliths, by +1.7 to +15.7 g/100 g protolith in the tremolite schist and +1.3 to +4.8 g/100 g protolith in the talc schist, but no significant change was seen in the talc+serpentine rock. Fe<sub>2</sub>O<sub>3</sub> and MgO were lost from most of the metasomatic zones with serpentinite protoliths (-1.9 to -5.5 and -14.8 to -30.1 g/100 g protolith, respectively), but one of the talc schist samples (150808S6) showed large gains (+2.4 to +15.7 and +20.1 to +100.0 g/100 g protolith, respectively). CaO was added to the tremolite schist ( $\pm 3.8$  to  $\pm 5.0$  g/100 g protolith) and the talc schist ( $\pm 0.2$  to  $\pm 0.5$  g/100 g protolith), and was lost slightly from the talc+serpentine rock (-0.1 to 0.0 g/100 g protolith). There was no significant change in Na<sub>2</sub>O or K<sub>2</sub>O in any of the metasomatic zones with serpentinite protoliths. LOI values decreased (-6.3 to -9.5 g/100 g protolith), except in one talc schist sample (150808S6) that showed a large increase (-1.3 to +12.7 g/100 g protolith). The  $V_{alt}/V_{ori}$  ratios for the tremolite schist, talc schist, and talc+serpentine rock are 0.52–0.69, 0.41–4.51, and 0.25–0.48, respectively (Table S2).

Most samples from the metasomatic zones in the serpentinite decreased in mass and volume (Fig. S11a–f; Table S2). However, the talc schist (150808S6) showed a significant gain in major elements (Fig. 11), with an increases in mass of 199%-473% and volume of 190%-451% (Table S2). The spinel is heterogeneously distributed through the talc schist, and occurs in the talc + chlorite matrix but not in the talc  $\pm$  tremolite matrix (Fig. S7c). These observations suggest that

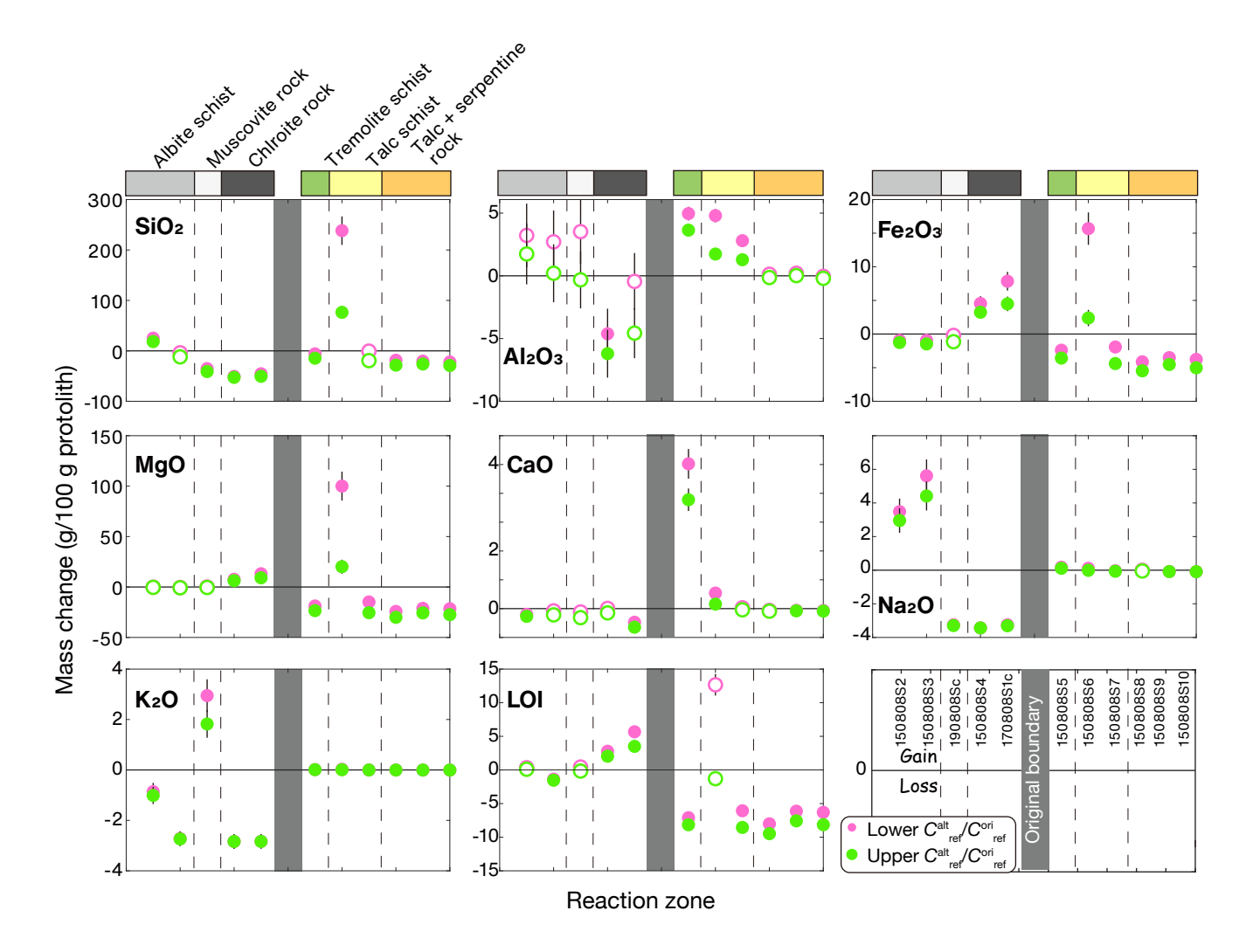


FIG. 11. Results of mass balance calculations for individual reaction zones. Filled symbols indicate statistically significant changes, and open symbols indicate no statistical significance. Error bars are ±2. When error bars are not shown, they are smaller than the size of the symbol. Rock samples are described in the lower left panel.

the talc  $\pm$  tremolite matrix in the talc schist was formed by precipitation or overgrowth in open fractures, rather than by metasomatic replacement of serpentinite; consequently, the bulk rock composition is not representative of the reaction zone.

Chemical components can be transferred from adjacent rocks, and can also be sourced from outside the system. The overall mass balance between the metasomatic zones with pelitic and serpentinite protoliths is given as follows:

$$\Delta C_i = \sum_j \left(\frac{c_{j,ref}^{alt}}{c_{j,ref}^{ori}}\right) L_j \rho_j^{alt} \Delta c_{i,j},\tag{2}$$

where  $c_{j,ref}^{ori}$  is the concentration of the geochemical reference element in the protolith;  $c_{j,ref}^{alt}$  is the concentration of the geochemical reference element in reaction zone j;  $\rho_j^{alt}$  (kg m<sup>-3</sup> altered rock) is the density of the altered rock of reaction zone j (Table 4);  $\Delta c_{i,j}$  (kg component i per kg original rock) is the

mass change of component i in the reaction zone j and was determined using Equation (1); and  $L_j$  (m) is the width of the reaction zone j, constrained by field observations (Table 1).  $\Delta C_i$  (kg m<sup>-2</sup> altered rock) is the overall mass change of component i and was calculated for lithologies where significant gain or loss was observed (Fig. 11). One of the talc schist samples (150808S6) was excluded because the bulk rock composition is not representative, as discussed above.

One albite schist sample (150808S2) showed an increase in  $SiO_2$ , whereas the other sample (150808S3) showed no significant change (Fig. 11). The increase in  $SiO_2$  in the albite rock is likely due to contamination from quartz veins that formed during the retrogression stage; the formation of the albite rock did not involve the transfer of  $SiO_2$ . In contrast, the muscovite rock and chlorite rock showed losses in  $SiO_2$ . Using the calculated losses and observed thicknesses (Table 1), the metasomatism of the pelitic schist released 507.5–883.7 kg m<sup>-</sup>2 of  $SiO_2$  (Fig. 12a). In contrast, the metasomatic zones in

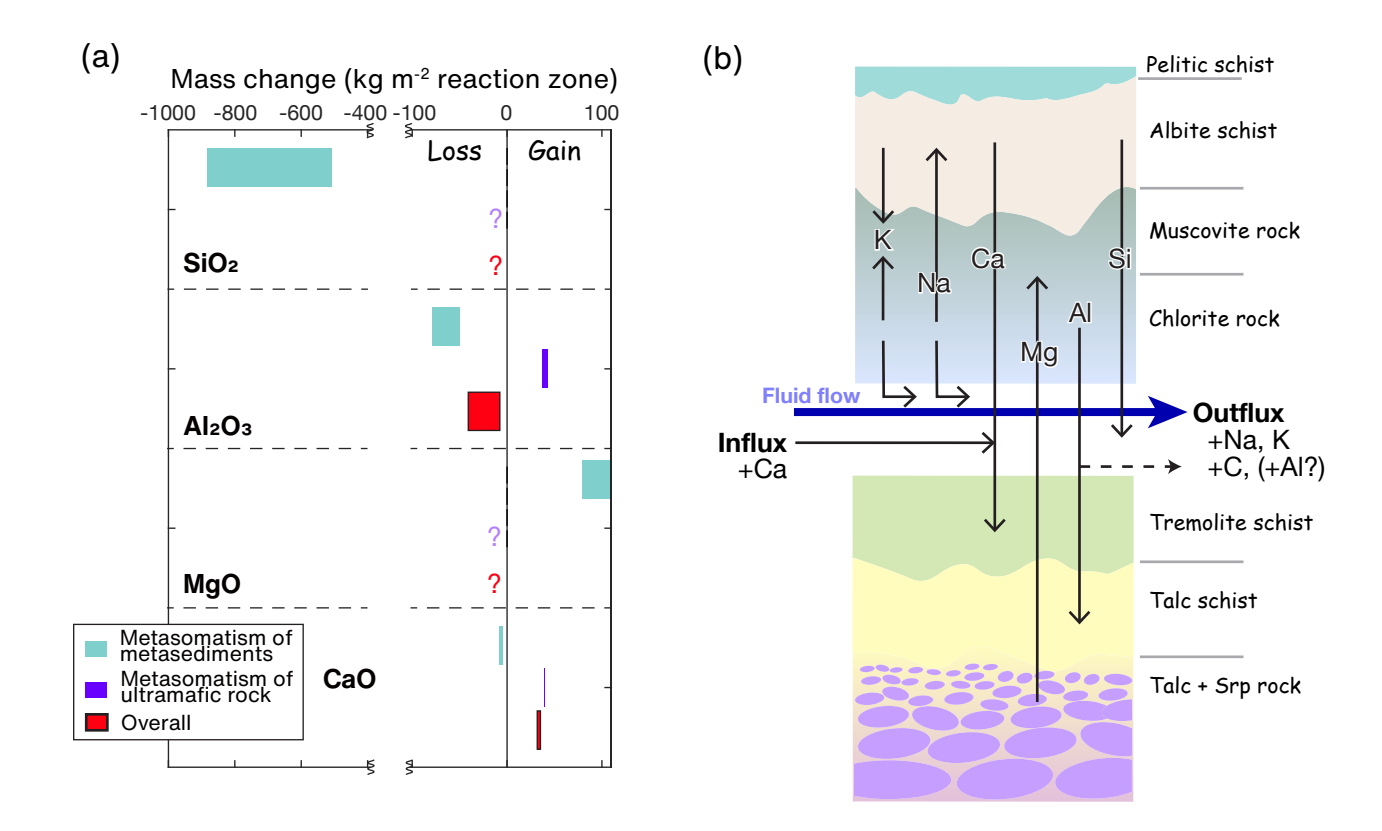


FIG. 12. (a) Results of mass balance calculations for the whole outcrop. Changes in the mass of SiO<sub>2</sub> and MgO due to the metasomatism of ultramafic rock were not estimated, due to the lack of evidence for mass transfer. (b) Schematic showing mass transfer through the reaction zone.

the serpentinite showed  $SiO_2$  loss. The metasomatism of serpentinite would release  $SiO_2$ ; however, our observations suggest the presence of thick talc layers that precipitated in open fractures may act as a significant reservoir of  $SiO_2$  and MgO. Because the original thickness of the precipitated talc layer is uncertain, the overall amount of  $SiO_2$  released during the metasomatism of serpentine is difficult to constrain. Thus, the present study did not constrain the overall  $SiO_2$  mass transfer, and it is unclear whether the  $SiO_2$  released from the pelitic schist was balanced (Fig. 12a, b).

Most samples from the metasomatic zones in the pelitic schist show no significant change in Al<sub>2</sub>O<sub>3</sub> contents, but a chlorite rock sample (170808S4) shows a loss of Al<sub>2</sub>O<sub>3</sub>. Using the values from the chlorite rock sample (170808S4). we estimate that the formation of the chlorite rock released  $50.3-78.2 \text{ kg m}^{-2} \text{ of Al}_2\text{O}_3$  (Fig. 12a). In contrast, in the metasomatic zones in the serpentinite, the tremolite and talc schists show an increase in Al<sub>2</sub>O<sub>3</sub> (Fig. 11). Using the calculated Al<sub>2</sub>O<sub>3</sub> gains and the observed thicknesses (Table 1), the formation of the tremolite and talc schists from the serpentinite resulted in gains of  $32.1-34.6 \text{ kg m}^{-2}$  and  $5.2-8.1 \text{ kg m}^{-2}$ of Al<sub>2</sub>O<sub>3</sub>, respectively, resulting in a total gain of 37.3–42.7 kg m<sup>-2</sup> of Al<sub>2</sub>O<sub>3</sub> (Fig. 12a). More Al<sub>2</sub>O<sub>3</sub> was released from the pelitic schist than was added to the serpentinite, suggesting that the Al<sub>2</sub>O<sub>3</sub> added to the serpentinite was sourced from the pelitic schist. No external source of Al<sub>2</sub>O<sub>3</sub> was required, and excess  $Al_2O_3$  (7.6–40.9 kg m<sup>-2</sup>) may have been released to an external system (Fig. 12a, b). In general, the solubility of  $Al_2O_3$  was low. However, the release of  $Al_2O_3$  from the pelitic schist occurred along with a release of  $SiO_2$ , suggesting the large-scale transfer of  $Al_2O_3$  may be facilitated by the increased solubility of Al due to the formation of Si–Al complexes (Manning 2007).

The chlorite rock samples (150808S4 and 170808S1c) show increases in MgO, with greater increases closer to the original boundary (Fig. 11). Based on the thickness of the chlorite rock (Table 1) and the estimated increase in MgO (Fig. 11), 79.0–103.0 kg m<sup>-2</sup> of MgO was added during the metasomatism of the pelitic schist (Fig. 12a). The metasomatic zones in the serpentinite show MgO loss, but the overall MgO loss during the metasomatism of the serpentine is difficult to constrain because of the presence of a talc layer that may have been precipitated in open fractures. However, the formation of the tremolite schist from the serpentinite would have resulted in 145.7–239.6 kg m<sup>-2</sup> of MgO loss, suggesting the metasomatism of serpentinite was a sufficient source for the MgO added to the pelitic schist.

We observed CaO losses in the albite schist (sample 150808S3) and chlorite rock (sample 170808S1c) (Fig. 11), which result in the release of 4.5-8.0 kg m<sup>-2</sup> of CaO during the metasomatism of the pelitic schist. In contrast, the tremolite schist that formed from the serpentinite gained 38.6-38.9

kg m<sup>-2</sup> of CaO (Fig. 12a), suggesting that an external source of CaO (30.6–34.5 kg m<sup>-2</sup>) is required to explain its CaO content (Fig. 12a, b).

The albite rock shows a gain in Na<sub>2</sub>O, while the muscovite and chlorite rocks show losses (Fig. 11). Using the calculated gain and the observed thickness of the albite rock, we estimate that the formation of the albite rock from the pelitic schist required the addition of 13.4–30.6 kg m<sup>-2</sup> of Na<sub>2</sub>O. Similarly, the formation of the muscovite rock and chlorite rock from the pelitic schist resulted in the release of 14.0–17.6 kg m<sup>-2</sup> and 25.4–43.3 kg m<sup>-2</sup> of Na<sub>2</sub>O, respectively, resulting in a total loss of 39.4–60.9 kg m<sup>-2</sup> of Na<sub>2</sub>O. This suggests that the Na<sub>2</sub>O gained by the albite rock was sourced from the Na<sub>2</sub>O released during the formation of the muscovite and chlorite rocks, and excess Na<sub>2</sub>O (8.8–47.5 kg m<sup>-2</sup>) may have been released to an external system.

The muscovite rock shows a gain in K<sub>2</sub>O, while the albite and chlorite rocks show losses (Fig. 11). Using the calculated gain and the observed thickness of the muscovite rock, we estimate that the formation of the muscovite rock from the pelitic schist would have required the addition of 9.8–12.7 kg m<sup>-2</sup> of K<sub>2</sub>O. On the other hand, the formation of the albite and chlorite rocks would have released 3.6–17.2 kg m<sup>-2</sup> and 22.1–35.8 kg m<sup>-2</sup> of K<sub>2</sub>O, respectively, resulting in a total release of 25.7–48.5 kg m<sup>-2</sup> of K<sub>2</sub>O. This suggests that the K<sub>2</sub>O gained by the muscovite rock may have been sourced from the K<sub>2</sub>O released during the formation of the albite and chlorite rocks, and excess K<sub>2</sub>O (13.0–38.7 kg m<sup>-2</sup>) may have been released to an external system.

The chlorite rock is similar to outcrops commonly described as "chlorite blackwalls" (Frost 1975; Bebout and Barton 2002; Maekawa et al. 2004; King et al. 2006; Miller et al. 2009). Our mass balance calculations suggest that the chlorite rock was formed by a gain in Fe<sub>2</sub>O<sub>3</sub>, MgO, and H2O, and loss of SiO<sub>2</sub>, Al<sub>2</sub>O<sub>3</sub>, CaO, Na<sub>2</sub>O, and K<sub>2</sub>O from a pelitic schist, and the MgO released by the metasomatism of serpentinite (forming the tremolite schist, talc schist, and talc+serpentine rock) would have been transported to the pelitic schist, forming the chlorite rock. A similar mechanism (i.e., Mg metasomatism producing a chlorite reaction zone) has been proposed for greenschist facies serpentinite-metasediment interfaces (Okamoto et al. 2021) and eclogite, blueschist, and serpentine-metagabbro interfaces evolved throughout retrogression from eclogite to greenschist facies (Codillo et al. 2022a). These previous studies proposed that the metasomatism of crustal lithologies was driven by the high solubility of Mg due to the formation of Mg(OH)<sub>2</sub>(aq) at high pressures and temperatures (Okamoto et al. 2021; Codillo et al. 2022a). Our study, as well as these previous studies, suggests that Mg metasomatism of crustal lithologies in contact with serpentinite is favored over a wide range of P-T conditions in the subduction zone.

CM has not been observed in the muscovite and chlorite rocks (Fig. 3a, 4c, d), although their protolith (the pelitic schist) contains CM (Fig. 3a), and carbonates have not been observed anywhere in the outcrop (Fig. 3); therefore, the CM must have been removed during metasomatic formation of the muscovite and chlorite rocks, although a quantitative estimate

of the C flux was not carried out in the present study. In general, the subducted CM is largely preserved in metasediments; however, experiments reveal that CM is soluble in metamorphic fluids (Nishiyama 1990; Tumiati et al. 2020). Carbon removal during metasomatism could be related to the fluid-mediated addition of Mg and removal of Si (Figs. 11, 12a) from the pelitic schist, because Mg–Si–C complexes would increase the solubility of C in subduction fluids (Tumiati et al. 2017; Huang and Sverjensky 2019; Tiraboschi et al. 2022).

#### D. Implications

We investigated the processes of metasomatism along a metasediment–serpentinite interface at peak P-T conditions (530–570 °C and 0.8–1.0 GPa), which corresponds to a depth of ~40 km (Aoya et al. 2013) at the mantle wedge corner in the Cretaceous Sanbagawa subduction zone (Fig. 10a, b). Outcrops of a reaction zone between pelitic schist and serpentine are not well preserved in the Sanbagawa metamorphic belt, possibly due to the preferential erosion of weak minerals (e.g., talc) in the reaction zone by river flow. However, similar reaction zones have been reported elsewhere (Maekawa et al. 2004), suggesting that the process observed is pervasive.

Geophysical observations reveal that the slab-mantle interface is decoupled at <70-80 km depth and acts as a weak shear zone. Peacock and Wang (2021) proposed that decoupling between the subducting slab and mantle wedge is caused by metasomatism that produces talc at the mantle wedge corner. Our observations show that tremolite-, chlorite-, and talc-rich rock formed from serpentinite around the metasediment-ultramafic rock boundary (Fig. 2a). Formation of these weak minerals would affect rheological properties, even the proportion of minerals are a few tens vol% (Moore and Lockner 2011; Hirauchi et al. 2013, 2020). Moreover, chlorite-rich reaction zones should form in crustal lithologies (metasediments and metagabbro) adjacent to serpentinite over a wide range of P-T conditions, as discussed in section 5.3 (Okamoto et al. 2021; Codillo et al. 2022a). Therefore, the degree of slab-mantle coupling at the subduction interface could be controlled by the mechanical characteristics of tremolite-, chlorite, and talc-rich rocks.

In warm subduction zones, including Nankai (Kii and Tokai) and Cascadia, episodic tremor and accompanying slow slip occur along the base of the mantle wedge. The mechanism of episodic tremor and accompanying slow slip is debated. One possible mechanism is high pore-fluid pressures around the mantle wedge (Gao and Wang 2017), possibly in talc-bearing metasomatic rocks (French and Condit 2019; Hoover et al. 2022) and generated by metasomatic dehydration along a lithological contact (Tarling et al. 2019; Okamoto et al. 2021). Okamoto et al. (2021) presented a thermodynamic model of the metasomatism of serpentinite by fluids that equilibrated with a metapelite. They proposed that the carbonation of serpentinite was accompanied by a decrease in the solid volume (~1 vol.%), dehydration, and an increase in the total fluid + solid volume, which would promote fluid overpressure. Similar fluid overpressures and hydrofracturing have been suggested for the isovolumetric metasomatism of serpentinite (Nishiyama et al. 2017). Our mass balance calculations show that the metasomatism of serpentinite to form tremolite schist, talc schist, and talc+serpentine rock was also accompanied solid volume decrease (Table S2). Moreover, Okamoto et al. (2021) conducted coupled mechanical-hydrological modeling to investigate the fracture pattern induced by the dehydration reaction between a serpentinite body and a pelitic schist matrix under solid volume expansion and also contraction. Under expansion, radial cracks develop preferentially in the surrounding matrix, whereas under contraction they develop preferentially in the serpentinite body. The veins in the matrix of the pelitic schist surrounding the serpentinite body are oriented at a high angle to the foliation in the schist (Fig. 2b), indicating the veins formed after metasomatism and during the later stages of exhumation (Toriumi and Hara 1995; Okamoto et al. 2008). In contrast, a pervasive network of talc veins developed preferentially in the metasomatized volume of the serpentinite body (Figs. 2c, S1). This vein network is consistent with the fracture pattern that is predicted to develop during contraction of the serpentinite body as a result of metasomatism (Okamoto et al., 2021), and the Ca-Al-Si metasomatism of serpentinite would have induced fracturing and elevated the pore-fluid pressure in the serpentinite at the mantle wedge corner.

Chlorite and muscovite are important carriers of  $\rm H_2O$  to the deep Earth, because they are stable up to 5.0–6.2 GPa (Hermann and Lakey 2021) and 10 GPa (Schmidt 1996), respectively. Our observations demonstrate that these minerals are not only formed by the metamorphism of sediments, but also by the metasomatism of pelitic schists adjacent to serpentinite. Although the size of the reaction zone in this study is limited (~0.2 m thickness; Fig. 2b), chlorite-rich reaction zones 10–100 m thick are predicted to occur at the slab–mantle interface (Spandler et al. 2008; Marschall and Schumacher 2012). We suggest that chlorite and muscovite reaction zones that form at shallow depths (30–40 km) are important H2O reservoirs controlling the flux of  $\rm H_2O$  to the deep Earth (~180–300 km). Therefore, the effect of metasomatism must be considered when calculating the  $\rm H_2O$  flux to the deep Earth.

Our observations and discussions in section 5.3 suggest that subducted CM can be mobilized by aqueous phases at shallow forearc depths (30–40 km) via metasomatic reactions between metasediments and serpentinite. Selective dissolution of CM has been reported in metasomatic zones in ultramafic mélanges (Nishiyama 1990; Mori et al. 2014) and blueschistfacies metapelites (Vitale Brovarone et al. 2020). The metasomatic mobilization of CM could result in the carbonation of serpentinite (e.g., Nishiyama 1990); however, in the Tomisato body we did not find any carbonate minerals in the metasomatic zone in the serpentinite, indicating that the dissolution of carbon in the pelitic schist did not necessarily lead to the carbonation of adjacent serpentinite. In fact, many examples of tremolite-rich rocks that lack carbonate have been reported in the Sanbagawa metamorphic belt, and these are thought to be the products of metasomatic reactions between serpentinite and metasediments (Kunugiza et al. 1986; Aoya et al. 2013) although carbonate-bearing or carbonated serpentinite has also been reported in the Sanbagawa metamorphic belt (Kawahara et al. 2016; Okamoto et al. 2021). Further study is required for understanding carbon cycling in the Sanbagawa metamorphic belt (e.g., Wada et al. 1984; Morohashi et al. 2008). Sieber et al. (2022) proposed that the metasomatism of serpentinite may shift the composition of COH-bearing fluids from CO<sub>2</sub>(aq)-rich to CO<sub>2</sub>(aq)-depleted and SiO<sub>2</sub>(aq)-rich. These fluids would induce Si metasomatism in serpentinite away from the flow of COH-bearing fluid. Our study suggests that carbonation of the mantle wedge is spatially heterogeneous, thereby complicating its rheological properties and the chemical composition of the rocks at the slab–mantle interface.

#### VI. CONCLUSIONS

We investigated an ultramafic body that originated in the mantle wedge in the Sanbagawa metamorphic belt, SW Japan. We summarize our findings below.

- 1. A reaction zone at the metasediment–serpentinite interface consist of pelitic schist, albite schist, muscovite rock, chlorite rock, tremolite schist, talc schist, talc+serpentine rock, and serpentinite. The original interface between the pelitic schist and serpentinite can be constrained from the presence of Ti- and Cr-bearing phases and was located between the chlorite rock and the tremolite schist. Thus, the pelitic schist was the protolith of the albitite schist, muscovite rock, and chlorite rock.
- 2. The peak pressure–temperature (P-T) conditions experienced by the pelitic schist were 0.8–1.0 GPa and 530–570 °C, based on hornblende–plagioclase–quartz thermometry, Raman spectroscopy of carbonaceous material thermometry, and quartz-in-garnet geobarometry.
- 3. Garnet crystals in the pelitic schist exhibit bell-shaped zoning in spessartine content, indicating prograde growth. Compositional zoning in garnet crystals from the muscovite rock is also consistent with prograde garnet growth, although they have grossular-rich outer rims that are not observed in crystals from the pelitic schist. The grossular-rich outer rims record a change in the whole-rock composition and suggest that metasomatism at the pelite–serpentinite interface started around the peak P-T conditions.
- 4. Our mass balance calculations suggest that  $SiO_2$  was lost (-507.5 to -883.7 kg m<sup>-2</sup>) from the reaction zones in the pelitic schist, whereas the metasomatic zones in the serpentinite gained  $Al_2O_3$  (+37.3 to +42.7 kg m<sup>-2</sup>) and CaO (+38.6 to +38.9 kg m<sup>-2</sup>). The metasomatic zones in the serpentinite lost  $SiO_2$  and MgO. Consequently, at the metasediment–serpentinite interface, the Mg-metasomatism of the metasediment produced a chlorite-rich reaction zone, and Ca-Al-metasomatism

of the serpentinite produced a tremolite-talc-chlorite-rich reaction zone. The mechanical and chemical characteristics of the subduction interface could be controlled by tremolite-, chlorite-, and talc-rich rocks (formed from serpentinite) and chlorite-rich rocks (formed from metasediments).

- 5. Estimates of the overall mass transfer between the pelitic schist and serpentinite show that the whole outcrop gained CaO (30.6–34.5 kg m<sup>-2</sup>) and lost Na<sub>2</sub>O and K<sub>2</sub>O (-8.8 to -47.5 kg m<sup>-2</sup> and -13.0 to -38.7 kg m<sup>-2</sup>, respectively), suggesting that a CaO-rich fluid infiltrated from outside the system and Na<sub>2</sub>O, K<sub>2</sub>O, and C was removed by fluid flow. No external source of Al<sub>2</sub>O<sub>3</sub> is required. Qualitatively, C was also removed. Si–Al (e.g., Manning 2007) and Mg–C–Si (e.g., Tumiati et al. 2017) complexes may have formed in the input and output fluids, respectively.
- 6. The present study suggests that metasomatism at the mantle wedge corner redistributes elements in the fluid and rocks, introduces spatial heterogeneities in the mineral assemblages in the mantle wedge and subduct-

ing slab, and produces fluid overpressure. This process would, therefore, influence slab—mantle decoupling, seismicity, and global geochemical cycling.

#### **ACKNOWLEDGMENTS**

We thank Mitsuhiro Toriumi, Yoshitaka Hashimoto, and Ken-ichi Hirauchi for valuable discussions during fieldwork. We thank Kenta Yoshida for advice on RSCM thermometry and QuiG geobarometry and for valuable comments on an early version of this manuscript. Hikaru Sawada is thanked for discussions regarding geochemistry. We thank Satoshi Matsuno and Shinichi Yamasaki for assisting with whole-rock analyses. We appreciate constructive comments from two anonymous reviewers and Timm John for editorial handling. This work was supported by the Japan Society for the Promotion of Science KAKENHI grants (JP18J01649, JP19K14827, JP20KK0079, JP22H05295 and JP22H04932) and by Earthquake Research Institute, the University of Tokyo, Joint Research program (ERI JURP 2021-B-01).

## References

- Ague JJ (2014) Fluid Flow in the Deep Crust. In: Treatise on Geochemistry, 2nd Endo S, Wallis SR, Tsuboi M, et al (2012) Slow subduction and buoyant edn. Elsevier, pp 203-247
- Ague JJ (2011) Extreme channelization of fluid and the problem of element mobility during Barrovian metamorphism. Am Mineral 96:333-352. https://doi.org/10.2138/am.2011.3582
- Aoya M, Endo S, Mizukami T, Wallis SR (2013) Paleo-mantle wedge preserved in the Sambagawa high-pressure: Metamorphic belt and the thickness of forearc continental crust. Geology 41:451-454. https://doi.org/10.1130/G33834.1
- Banno S (2004) Ultramafic Rocks and Associated Eclogites of the Sanbagawa Schists, Japan: A Review. Int Geol Rev 46:693-704. https://doi.org/10.2747/0020-6814.46.8.693
- Banno S, Sakai C, Higashino T (1986) Pressure-temperature trajectory of the Sanbagawa metamorphism deduced from garnet zoning. Lithos 19:51-63. https://doi.org/10.1016/0024-4937(86)90015-0
- Beard JS, Frost BR (2017) The stoichiometric effects of ferric iron substitutions in serpentine from microprobe data. Int Geol Rev 59:541-547. https://doi.org/10.1080/00206814.2016.1197803
- Bebout GE, Barton MD (2002) Tectonic and metasomatic mixing in a high-T, subduction-zone melange — insights into the geochemical evolution of the me slab - mantle interface. Chem Geol 187:79-106. https://doi.org/10.1016/S0009-2541(02)00019-0
- Beinlich A, John T, Vrijmoed JC, et al (2020) Instantaneous rock transformations in the deep crust driven by reactive fluid flow. Nat Geosci 13:307-311. https://doi.org/10.1038/s41561-020-0554-9
- Beyssac O, Goffé B, Chopin C, Rouzaud JN (2002) Raman spectra of carbonaceous material in metasediments: a new geothermometer. J Metamorph Geol 20:859-871. https://doi.org/10.1046/j.1525-1314.2002.00408.x
- Beyssac O, Goffé B, Petitet J-P, et al (2003) On the characterization of disordered and heterogeneous carbonaceous materials by Raman spectroscopy. Spectrochim Acta Part A Mol Biomol Spectrosc 59:2267-2276. https://doi.org/10.1016/S1386-1425(03)00070-2
- Beyssac O, Simoes M, Avouac JP, et al (2007) Late Cenozoic metamorphic evolution and exhumation of Taiwan. Tectonics 26:TC6001. https://doi.org/10.1029/2006TC002064
- Codillo EA, Klein F, Dragovic B, et al (2022a) Fluid Mediated Mass Transfer Between Mafic and Ultramafic Rocks in Subduction Zones. Geochemistry, Geophys Geosystems 23:. https://doi.org/10.1029/2021GC010206
- Codillo EA, Klein F, Marschall HR (2022b) Preferential Formation of Chlorite Over Talc During Si-Metasomatism of Ultramafic Rocks in Subduction Zones. Geophys Res Lett 49:1-12. https://doi.org/10.1029/2022GL100218
- Collettini C, Viti C, Smith SAF, Holdsworth RE (2009) Development of interconnected talc networks and weakening of continental low-angle normal faults. Geology 37:567-570. https://doi.org/10.1130/G25645A.1
- Condit CB, Guevara VE, Delph JR, French ME (2020) Slab dehydration in warm subduction zones at depths of episodic slip and tremor. Earth Planet Sci Lett 552:116601. https://doi.org/10.1016/j.epsl.2020.116601
- Dale J, Powell R, White RW, et al (2005) A thermodynamic model for Ca-Na clinoamphiboles in Na2O-CaO-FeO-MgO-Al2O3-SiO2-H2O-O for petrological calculations. J Metamorph Geol 23:771-791. https://doi.org/10.1111/j.1525-1314.2005.00609.x
- Dullien FAL (1992) Porous Media: Fluid Transport and Pore Structure. Academic Press
- Enami M (1983) Petrology of pelitic schists in the oligoclase-biotite zone of the Sanbagawa metamorphic terrain, Japan: phase equilibria in the highest grade zone of a high-pressure intermediate type of metamorphic belt. J Metamorph Geol 1:141-161. https://doi.org/10.1111/j.1525-1314.1983.tb00269.x
- Enami M (1998) Pressure-temperature path of Sanbagawa prograde metamorphism deduced from grossular zoning of garnet. J Metamorph Geol 16:97-106. https://doi.org/10.1111/j.1525-1314.1998.00058.x
- Enami M (2012) Influence of garnet hosts on the raman spectra of quartz inclusions. J Mineral Petrol Sci 107:173-180. https://doi.org/10.2465/jmps.111216
- Enami M, Wallis SR, Banno Y (1994) Paragenesis of sodic pyroxene-bearing quartz schists: implications for the P-T history of the Sanbagawa belt. Contrib to Mineral Petrol 116:182-198. https://doi.org/10.1007/BF00310699
- Endo S, Wallis S, Hirata T, et al (2009) Age and early metamorphic history of the Sanbagawa belt: Lu-Hf and P - T constraints from the Western Iratsu eclogite. J Metamorph Geol 27:371-384. https://doi.org/10.1111/j.1525-1314.2009.00821.x

- exhumation of the Sanbagawa eclogite. Lithos 146-147:183-201. https://doi.org/10.1016/j.lithos.2012.05.010
- Erambert M, Austrheim H (1993) The effect of fluid and deformation on zoning and inclusion patterns in poly-metamorphic garnets. Contrib to Mineral Petrol 115:204-214. https://doi.org/10.1007/BF00321220
- Escartín J, Andreani M, Hirth G, Evans B (2008) Relationships between the microstructural evolution and the rheology of talc at elevated pressures and temperatures. Earth Planet Sci Lett 268:463-475. https://doi.org/10.1016/j.epsl.2008.02.004
- French ME, Condit CB (2019) Slip partitioning along an idealized subduction plate boundary at deep slow slip conditions. Earth Planet Sci Lett 528:115828. https://doi.org/10.1016/j.epsl.2019.115828
- Frost BR (1975) Contact metamorphism of serpentinite, chloritic blackwall and rodingite at paddy-go-easy pass, central cascades, Washington. J Petrol 16:272-313. https://doi.org/10.1093/petrology/16.1.272
- Galvez ME, Connolly JAD, Manning CE (2016) Implications for metal and volatile cycles from the pH of subduction zone fluids. Nature 539:420-424. https://doi.org/10.1038/nature20103
- Galvez ME, Manning CE, Connolly JAD, Rumble D (2015) The solubility of rocks in metamorphic fluids: A model for rock-dominated conditions to upper mantle pressure and temperature. Earth Planet Sci Lett 430:486-498. https://doi.org/10.1016/j.epsl.2015.06.019
- Gao X, Wang K (2017) Rheological separation of the megathrust seismogenic zone and episodic tremor and slip. Nature 543:416-419. https://doi.org/10.1038/nature21389
- Gonzalez CM, Gorczyk W, Gerya T V. (2016) Decarbonation of subducting slabs: Insight from petrological-thermomechanical modeling. Gondwana Res 36:314-332. https://doi.org/10.1016/j.gr.2015.07.011
- Hacker BR, Peacock SM, Abers GA, Holloway SD (2003) Subduction factory 2. Are intermediate-depth earthquakes in subducting slabs linked to metamorphic dehydration reactions? J Geophys Res Solid Earth 108:. https://doi.org/10.1029/2001jb001129
- Hermann J, Lakey S (2021) Water transfer to the deep mantle through hydrous, Al-rich silicates in subduction zones. Geology 49:911-915. https://doi.org/10.1130/G48658.1
- Higashino T (1990) The higher grade metamorphic zonation of the Sambagawa metamorphic belt in central Shikoku, Japan. J Metamorph Geol 8:413-423. https://doi.org/10.1111/j.1525-1314.1990.tb00628.x
- Hirauchi K, den Hartog SAM, Spiers CJ (2013) Weakening of the slab-mantle wedge interface induced by metasomatic growth of talc. Geology 41:75-78. https://doi.org/10.1130/G33552.1
- Hirauchi K ichi, Katayama I (2013) Rheological contrast between serpentine species and implications for slab-mantle wedge decoupling. Tectonophysics 608:545-551. https://doi.org/10.1016/j.tecto.2013.08.027
- Hirauchi K ichi, Nagata Y, Kataoka K, et al (2021) Cataclastic and crystalplastic deformation in shallow mantle-wedge serpentinite controlled by cyclic changes in pore fluid pressures. Earth Planet Sci Lett 576:117232. https://doi.org/10.1016/j.epsl.2021.117232
- Hirauchi K ichi, Yamamoto Y, den Hartog SAM, Niemeijer AR (2020) The role of metasomatic alteration on frictional properties of subduction thrusts: An example from a serpentinite body in the Franciscan Complex, California. Earth Planet Sci Lett 531:115967. https://doi.org/10.1016/j.epsl.2019.115967
- Holland T, Blundy J (1994) Non-ideal interactions in calcic amphiboles and their bearing on amphibole-plagioclase thermometry. Contrib to Mineral Petrol 116:433-447. https://doi.org/10.1007/BF00310910
- Hoover WF, Condit CB, Lindquist PC, et al (2022) Episodic Slow Slip Hosted by Talc - Bearing Metasomatic Rocks: High Strain Rates and Stress Amplification in a Chemically Reacting Shear Zone. Geophys Res Lett 49:. https://doi.org/10.1029/2022GL101083
- Huang F, Sverjensky DA (2019) Extended Deep Earth Water Model for predicting major element mantle metasomatism. Geochim Cosmochim Acta 254:192-230. https://doi.org/10.1016/j.gca.2019.03.027
- Inui M, Toriumi M (2002) Prograde pressure-temperature paths in the pelitic schists of the Sambagawa metamorphic belt, SW Japan. J Metamorph Geol 20:563-580. https://doi.org/10.1046/j.1525-1314.2002.00389.x
- John T, Gussone N, Podladchikov YY, et al (2012) Volcanic arcs fed by rapid pulsed fluid flow through subducting slabs. Nat Geosci 5:489-492. https://doi.org/10.1038/ngeo1482
- Katayama I, Kurosaki I, Hirauchi K ichi (2010) Low silica activity for hydrogen generation during serpentinization: An example of natural serpentinites in the Mineoka ophiolite complex, central Japan. Earth Planet Sci Lett 298:199-204. https://doi.org/10.1016/j.epsl.2010.07.045

- Kawahara H, Endo S, Wallis SR, et al (2016) Brucite as an important phase of the shallow mantle wedge: Evidence from the Shiraga unit of the Sanbagawa subduction zone, SW Japan. Lithos 254–255:53–66. https://doi.org/10.1016/j.lithos.2016.02.022
- Kim YH, Clayton RW, Asimow PD, Jackson JM (2013) Generation of talc in the mantle wedge and its role in subduction dynamics in central Mexico. Earth Planet Sci Lett 384:81–87. https://doi.org/10.1016/j.epsl.2013.10.006
- King RL, Bebout GE, Moriguti T, Nakamura E (2006) Elemental mixing systematics and Sr-Nd isotope geochemistry of mélange formation: Obstacles to identification of fluid sources to arc volcanics. Earth Planet Sci Lett 246:288–304. https://doi.org/10.1016/j.epsl.2006.03.053
- King RL, Kohn MJ, Eiler JM (2003) Constraints on the petrologic structure of the subduction zone slab-mantle interface from Franciscan Complex exotic ultramafic blocks. Bull Geol Soc Am 115:1097–1109. https://doi.org/10.1130/B25255.1
- Kouketsu Y, Enami M (2011) Calculated stabilities of sodic phases in the Sambagawa metapelites and their implications. J Metamorph Geol 29:301–316. https://doi.org/10.1111/j.1525-1314.2010.00919.x
- Kouketsu Y, Enami M, Mizukami T (2010) Omphacite-bearing metapelite from the Besshi region, Sambagawa metamorphic belt, Japan: Prograde eclogite facies metamorphism recorded in metasediment. J Mineral Petrol Sci 105:9–19. https://doi.org/10.2465/jmps.090217
- Kouketsu Y, Enami M, Mouri T, et al (2014a) Composite metamorphic history recorded in garnet porphyroblasts of Sambagawa metasediments in the Besshi region, central Shikoku, Southwest Japan. Isl Arc 23:263–280. https://doi.org/10.1111/iar.12075
- Kouketsu Y, Nishiyama T, Ikeda T, Enami M (2014b) Evaluation of residual pressure in an inclusion-host system using negative frequency shift of quartz Raman spectra. Am Mineral 99:433–442. https://doi.org/10.1515/am.2014.4427
- Kouketsu Y, Sadamoto K, Umeda H, et al (2021) Thermal structure in subducted units from continental Moho depths in a palaeo subduction zone, the Asemigawa region of the Sanbagawa metamorphic belt, SW Japan. J Metamorph Geol 39:727–749. https://doi.org/10.1111/jmg.12584
- Kunugiza K, Takasu A, Banno S (1986) The origin and metamorphic history of the ultramafic and metagabbro bodies in the Sanbagawa metamorphic belt. Mem Geol Soc Am 164:375–385. https://doi.org/10.1130/MEM164-p375
- Lanari P, Vidal O, De Andrade V, et al (2014) XMapTools: A MATLAB©-based program for electron microprobe X-ray image processing and geothermobarometry. Comput Geosci 62:227–240. https://doi.org/10.1016/j.cageo.2013.08.010
- Leake BE, Woolley AR, Birch WD, et al (2003) Nomenclature of amphiboles: additions and revisions to the international mineralogical association's 1997 recommendations. Can Mineral 41:1355–1362. https://doi.org/10.2113/gscanmin.41.6.1355
- Maekawa H, Yamamoto K, Ueno T, et al (2004) Significance of Serpentinites and Related Rocks in the High-Pressure Metamorphic Terranes, Circum-Pacific Regions. Int Geol Rev 46:426–444. https://doi.org/10.2747/0020-6814.46.5.426
- Manning CE (2007) Solubility of corundum + kyanite in H2O at 700°C and 10 kbar: Evidence for Al-Si complexing at high pressure and temperature. Geofluids 7:258–269. https://doi.org/10.1111/j.1468-8123.2007.00179.x
- Manning CE (1994) The solubility of quartz in H2O in the lower crust and upper mantle. Geochim Cosmochim Acta 58:4831–4839. https://doi.org/10.1016/0016-7037(94)90214-3
- Manning CE (1997) Coupled Reaction and Flow in Subduction Zones: Silica Metasomatism in the Mantle Wedge. Fluid Flow Transp. Rocks 139–148
- Manning CE (2018) Fluids of the Lower Crust: Deep Is Different. Annu Rev Earth Planet Sci 46:67–97. https://doi.org/10.1146/annurev-earth-060614-105224
- Manning CE, Frezzotti ML (2020) Subduction-zone fluids. Elements 16:395–400. https://doi.org/10.2138/GSELEMENTS.16.6.395
- Marschall HR, Schumacher JC (2012) Arc magmas sourced from mélange diapirs in subduction zones. Nat Geosci 5:862–867. https://doi.org/10.1038/ngeo1634
- McLennan SM (1989) Rare earth elements in sedimentary rocks: Influence of provenance and sedimentary processes. In: Reviews in Mineralogy and Geochemistry. pp 169–200
- Miller DP, Marschall HR, Schumacher JC (2009) Metasomatic formation and petrology of blueschist-facies hybrid rocks from Syros (Greece): Implications for reactions at the slab-mantle interface. Lithos 107:53–67. https://doi.org/10.1016/j.lithos.2008.07.015
- Mindaleva D, Uno M, Higashino F, et al (2020) Rapid fluid infiltration and permeability enhancement during middle–lower crustal fracturing:

- Evidence from amphibolite–granulite-facies fluid–rock reaction zones, Sør Rondane Mountains, East Antarctica. Lithos 372–373:105521. https://doi.org/10.1016/j.lithos.2020.105521
- Mindaleva D, Uno M, Tsuchiya N (2023) Short Lived and Voluminous Fluid - Flow in a Single Fracture Related to Seismic Events in the Middle Crust. Geophys Res Lett. https://doi.org/10.1029/2022GL099892
- Mizukami T, Yokoyama H, Hiramatsu Y, et al (2014) Two types of antigorite serpentinite controlling heterogeneous slow-slip behaviours of slabmantle interface. Earth Planet Sci Lett 401:148–158. https://doi.org/10.1016/j.epsl.2014.06.009
- Moore DE, Lockner DA (2011) Frictional strengths of talc-serpentine and talcquartz mixtures. J Geophys Res Solid Earth 116:1–17. https://doi.org/10.1029/2010JB007881
- Mori H, Wallis S (2009) Large-scale folding in the Asemi-gawa region of the Sanbagawa Belt, southwest Japan. Isl Arc 19:357–370. https://doi.org/10.1111/j.1440-1738.2010.00713.x
- Mori Y, Shigeno M, Nishiyama T (2014) Fluid-metapelite interaction in an ultramafic mélange: Implications for mass transfer along the slab-mantle interface in subduction zones. Earth, Planets Sp 66:1–8. https://doi.org/10.1186/1880-5981-66-47
- Morohashi K, Okamoto A, Satish-Kumar M, Tsuchiya N (2008) Variations in stable isotope compositions (δ13C, δ18O) of calcite within exhumation-related veins from the Sanbagawa metamorphic belt. J Mineral Petrol Sci 103:361–364. https://doi.org/10.2465/jmps.080620b
- Mouri T, Enami M (2008) Areal extent of eclogite facies metamorphism in the Sanbagawa belt, Japan: New evidence from a Raman microprobe study of quartz residual pressure. Geology 36:503. https://doi.org/10.1130/G24599A.1
- Nagaya T, Okamoto A, Oyanagi R, et al (2020) Crystallographic preferred orientation of talc determined by an improved EBSD procedure for sheet silicates: Implications for anisotropy at the slab—mantle interface due to Si-metasomatism. Am Mineral 105:873–893. https://doi.org/10.2138/am-2020-7006
- Nishiyama T (1989) Kinetics of hydrofracturing and metamorphic veining. Geology 17:1068–1071. https://doi.org/10.1130/0091-7613(1989)017<1068:KOHAMV>2.3.CO;2
- Nishiyama T (1990) CO2-metasomatism of a metabasite block in a serpentine melange from the Nishisonogi metamorphic rocks, southwest Japan. Contrib to Mineral Petrol 104:35–46. https://doi.org/10.1007/BF00310644
- Nishiyama T, Yoshida-Shiosaki C, Mori Y, Shigeno M (2017) Interplay of irreversible reactions and deformation: A case of hydrofracturing in the rodingite–serpentinite system. Prog Earth Planet Sci 4:1–17. https://doi.org/10.1186/s40645-016-0115-4
- Okamoto A, Kikuchi T, Tsuchiya N (2008) Mineral distribution within polymineralic veins in the Sanbagawa belt, Japan: Implications for mass transfer during vein formation. Contrib to Mineral Petrol 156:323–336. https://doi.org/10.1007/s00410-008-0288-y
- Okamoto A, Oyanagi R, Yoshida K, et al (2021) Rupture of wet mantle wedge by self-promoting carbonation. Commun Earth Environ 2:1–10. https://doi.org/10.1038/s43247-021-00224-5
- Okamoto A, Toriumi M (2005) Progress of actinolite-forming reactions in mafic schists during retrograde metamorphism: An example from the Sanbagawa metamorphic belt in central Shikoku, Japan. J Metamorph Geol 23:335–356. https://doi.org/10.1111/j.1525-1314.2005.00580.x
- Oyanagi R, Okamoto A, Satish-Kumar M, et al (2021) Hadal aragonite records venting of stagnant paleoseawater in the hydrated forearc mantle.

  Commun Earth Environ 2:1–10. https://doi.org/10.1038/s43247-021-00317-1
- Peacock SM (1987) Serpentinization and infiltration metasomatism in the Trinity peridotite, Klamath province, northern California: implications for subduction zones. Contrib to Mineral Petrol 95:55–70. https://doi.org/10.1007/BF00518030
- Peacock SM, Wang K (1999) Seismic consequences of warm versus cool subduction metamorphism: Examples from southwest and northeast Japan. Science (80-) 286:937–939. https://doi.org/10.1126/science.286.5441.937
- Peacock SM, Wang K (2021) On the Stability of Talc in Subduction Zones: A Possible Control on the Maximum Depth of Decoupling Between the Subducting Plate and Mantle Wedge. Geophys Res Lett 48:1–8. https://doi.org/10.1029/2021GL094889
- Penniston-Dorland SC, Gorman JK, Bebout GE, et al (2014) Reaction rind formation in the Catalina Schist: Deciphering a history of mechanical mixing and metasomatic alteration. Chem Geol 384:47–61. https://doi.org/10.1016/j.chemgeo.2014.06.024
- Penniston-Dorland SC, Sorensen SS, Ash RD, Khadke S V. (2010) Lithium

- isotopes as a tracer of fluids in a subduction zone mélange: Franciscan Complex, CA. Earth Planet Sci Lett 292:181–190. https://doi.org/10.1016/j.epsl.2010.01.034
- Rüpke LH, Morgan JP, Hort M, Connolly JAD (2004) Serpentine and the subduction zone water cycle. Earth Planet Sci Lett 223:17–34. https://doi.org/10.1016/j.epsl.2004.04.018
- Saiga A, Kato A, Kurashimo E, et al (2013) Anisotropic structures of oceanic slab and mantle wedge in a deep low-frequency tremor zone beneath the Kii Peninsula, SW Japan. J Geophys Res Solid Earth 118:1091–1097. https://doi.org/10.1002/jgrb.50069
- Sanford RF (1982) Growth of ultramafic reaction zones in greenschist to amphibolite facies metamorphism. Am J Sci 282:543–616. https://doi.org/10.2475/ajs.282.5.543
- Schmidt MW (1996) Experimental Constraints on Recycling of Potassium from Subducted Oceanic Crust. Science (80- ) 272:1927–1930. https://doi.org/10.1126/science.272.5270.1927
- Sieber MJ, Yaxley GM, Hermann J (2022) COH-fluid induced metasomatism of peridotites in the forearc mantle. Contrib to Mineral Petrol 177:1–22. https://doi.org/10.1007/s00410-022-01905-w
- Spandler C, Hermann J, Faure K, et al (2008) The importance of talc and chlorite "hybrid" rocks for volatile recycling through subduction zones; evidence from the high-pressure subduction mélange of New Caledonia. Contrib to Mineral Petrol 155:181–198. https://doi.org/10.1007/s00410-007-0236-2
- Steenberg L, Boroughs S, Knaack C (2017) Estimation of accuracy and precision for trace elements analyzed by inductively coupled plasma mass spectrometry (ICP-MS) at the Peter Hooper GeoAnalytical laboratory, Washington State University. Geol Soc Am Abstr with Programs 49:. https://doi.org/10.1130/abs/2017AM-307211
- Taetz S, John T, Bröcker M, et al (2018) Fast intraslab fluid-flow events linked to pulses of high pore fluid pressure at the subducted plate interface. Earth Planet Sci Lett 482:33–43. https://doi.org/10.1016/j.epsl.2017.10.044
- Tarling MS, Smith SAF, Scott JM (2019) Fluid overpressure from chemical reactions in serpentinite within the source region of deep episodic tremor. Nat Geosci 12:1034–1042. https://doi.org/10.1038/s41561-019-0470-z
- Tiraboschi C, Miozzi F, Tumiati S (2022) Carbon-saturated COH fluids in the upper mantle: A review of high-pressure and high-temperature ex situ experiments. Eur J Mineral 34:59–75. https://doi.org/10.5194/ejm-34-59.2022
- Toriumi M, Hara E (1995) Crack geometries and deformation by the crack-seal mechanism in the Sambagawa metamorphic belt. Tectonophysics 245:249–261. https://doi.org/10.1016/0040-1951(94)00238-5
- Tumiati S, Tiraboschi C, Miozzi F, et al (2020) Dissolution susceptibility of glass-like carbon versus crystalline graphite in high-pressure aqueous fluids and implications for the behavior of organic matter in subduction zones. Geochim Cosmochim Acta 273:383–402. https://doi.org/10.1016/j.gca.2020.01.030
- Tumiati S, Tiraboschi C, Sverjensky DA, et al (2017) Silicate dissolution boosts the CO2 concentrations in subduction fluids. Nat Commun 8:1–11. https://doi.org/10.1038/s41467-017-00562-z
- Uno M, Iwamori H, Toriumi M (2015) Transition from dehydration to hydration during exhumation of the Sanbagawa metamorphic belt, Japan, revealed by the continuous P–T path recorded in garnet and amphibole zoning. Contrib to Mineral Petrol 170:. https://doi.org/10.1007/s00410-015-1185-9
- Vitale Brovarone A, Tumiati S, Piccoli F, et al (2020) Fluid-mediated selective dissolution of subducting carbonaceous material: Implications for carbon recycling and fluid fluxes at foreare depths. Chem Geol 549:119682. https://doi.org/10.1016/j.chemgeo.2020.119682
- Viti C, Collettini C (2009) Growth and deformation mechanisms of talc along a natural fault: A micro/nanostructural investigation. Contrib to Mineral Petrol 158:529–542. https://doi.org/10.1007/s00410-009-0395-4
- Wada H, Enami M, Yanagi T (1984) Isotopic studies of marbles in the Sanbagawa metamorphic terrain, central, Shikoku, Japan. Geochem J 18:61–73. https://doi.org/10.2343/geochemj.18.61
- Wallis S, Aoya M (2000) A re-evaluation of eclogite facies metamorphism in SW Japan: proposal for an eclogite nappe. J Metamorph Geol 18:653–664. https://doi.org/10.1046/j.1525-1314.2000.00285.x
- Wallis S, Takasu A, Enami M, Tsujimori T (2000) Eclogite and related metamorphism in the Sanbagawa belt, Southwest Japan. Bull Res Inst Nat Sci Okayama Univ Sci 26:3–17
- Wallis SR, Yamaoka K, Mori H, et al (2020) The basement geology of Japan from A to Z. Isl Arc 29:. https://doi.org/10.1111/iar.12339
- Whitney DL, Evans BW (2010) Abbreviations for names of rock-forming

- minerals. Am Mineral 95:185–187. https://doi.org/10.2138/am.2010.3371
- Whitney DL, Mechum TA, Dilek Y, Kuehner SM (1996) Modification of garnet by fluid infiltration during regional metamorphism in garnet through sillimanite-zone rocks, Dutchess County, New York. Am Mineral 81:696–705. https://doi.org/10.2138/am-1996-5-617
- Yamasaki S, Matsunami H, Takeda A, et al (2011) Simultaneous Determination of Trace Elements in Soils and Sediments by Polarizing Energy Dispersive X-ray Fluorescence Spectrometry. BUNSEKI KAGAKU 60:315–323. https://doi.org/10.2116/bunsekikagaku.60.315
- Yoshida K, Niki S, Sawada H, et al (2021) Discovery of the Early Jurassic hightemperature pre-Sanbagawa metamorphism recorded in titanite. Lithos 398–399:106349. https://doi.org/10.1016/j.lithos.2021.106349
- Reference in the supplementary materials
- Ague JJ (2017) Element mobility during regional metamorphism in crustal and subduction zone environments with a focus on the rare earth elements (REE). Am Mineral 102:1796–1821. https://doi.org/10.2138/am-2017-6130
- Ague JJ, Van Haren JL (1996) Assessing metasomatic mass and volume changes using the bootstrap, with application to deep crustal hydrothermal alteration of marble. Economic Geology 91:1169-1182. https://doi.org/10.2113/gsecongeo.91.7.1169
- Baumgartner LP, Olsen SN (1995) A least-squares approach to mass transport calculations using the isocon method. Economic Geology 90:1261-1270. https://doi.org/10.2113/gsecongeo.90.5.1261
- Holland T, Blundy J (1994) Non-ideal interactions in calcic amphiboles and their bearing on amphibole-plagioclase thermometry. Contrib to Mineral Petrol 116:433–447. https://doi.org/10.1007/BF00310910
- Penniston-Dorland SC, Ferry JM (2008) Element mobility and scale of mass transport in the formation of quartz veins during regional metamorphism of the Waits River Formation, east-central Vermont. Am Mineral, 93:7–21. https://doi.org/10.2138/am.2008.2461
- Whitney DL, Evans BW (2010) Abbreviations for names of rock-forming minerals. Am Mineral 95:185–187. https://doi.org/10.2138/am.2010.3371

**Table 1.** Sample descriptions and relative locations.

	_	Distance	Thickness	
Sample no.	Zone	(cm)	(cm)	
150808S1	Pelitic schist	0		
170808S17-4		-		
150808S2		22		
150808S3	Albite schist	35		20
170808S1a_up		-		
170808S1a_low		-		
170808S1b_up		-		
190808Sb	Muscovite rock	-		10
190808Sc		-		
190808Sa_up		-		
150808S4		55		
170808S1b_low	Chlorite rock	-		20
170808S1c	Chionte rock	-		20
190808Sa_low		-		
150808S5	Tremolite schist	85		20
150808S6	Talc schist	90		10
150808S7	Taic scriist	100		10
150808S8	Talc +	130		
150808S9		-		50
150808S10	serpentine rock	180		
150808S11	Serpentinite	300		

Table 2. Modal abundances of minerals in the reaction zones. Mineral abbreviations are after Whitney and Evans (2010).

Sample No.	150808S1	150808S3	170808S1a_up	170808S1a_low	170808S1b_up	170808Sb_low	170808S1c	150808S5	150808S6	150808S7	150808S8	150808S9	150808S11
Rock Type	Pelitic schist	Albite schist	Albite schist	Muscovite rock	Muscovite rock	Chlorite rock	Chlorite rock	Tr schist	Tlc schist	Tlc schist	Tlc + srp rock	Tlc + srp rock	Serpentinite
Mineral mode	(vol%)												
Qz	25.3	8.6	0.4										
PI	30.6	61.4	59.9										
Ms	28.9	7.7	24.1	86.1	69.4	2.3							
Ep	2.7			5.3		23.6	4.1						
Chl	5.3	2.0	13.5	6.3	14.2	68.2	93.7	33.2	20.5	34.0	7.7		
Grt	1.5	2.8		0.1									
Amp	0.7							66.7	1.3				
Ap	0.2	0.2	0.2		0.0	2.0	0.2						
Tor	3.7												
Rt													
Spt		15.9											
Ttn	1.1	1.5	1.9	2.2	2.6	3.9	2.0						
Tlc									78.6	64.0	42.0	13.1	
Srp										0.5	50.3	85.7	95.0
Spl								0.5	0.2	0.2	0.0	0.3	5.1

Table 3 Representative chemical compositions of minerals in the reaction zones

Mineral	Plagiocalse	Epidote			Ga	rnet							Amphibol	е						Chlorit	e				Talc		5	Serpentine			Spinel	
Lithology	Albite schist	Pelitic schist	Р	elitic sch	ist	М	uscovite	rock	Р	elitic sch	ist	,	Albite sch	ist	Tremolite schist	Talc schist	Pelitic schist	Albite schist	Muscovit- rock	Chlorite rock	e echiet	Talc schist	serpentine		serpentine	Talc schist		erpentine ick	Serpe	ntinite	Serpentinite S	erpentinite
			Core	<b>→</b>	Rim	Core	$\rightarrow$	Rim	Core	$\rightarrow$	Rim	Core	$\rightarrow$	Rim													Block	Matrx	Block	Matrx		
wt%																																
SiO <sub>2</sub>	68.80	37.61	36.30	35.68	35.95	35.96	36.41	36.42	44.87	46.83	50.78	48.44	49.18	52.50	56.59	57.29	25.88	26.87	7 25.6	6 27.21	31.28	8 34.2	0 34.37	62.49	62.04	37.45	40.15	41.68	43.11	44.33	0.23	0.06
TiO <sub>2</sub>	0.02	0.21	0.17	0.07	0.21	0.16	0.10	0.32	0.20	0.25	0.11	0.05	0.00	0.04	0.08	0.00	0.01	0.03	3 0.0	1 0.01	0.04	4 0.0	0 0.02	0.03	0.03	0.00	0.02	0.00	0.01	0.00	0.67	0.52
$Al_2O_3$	19.73	26.80	21.11	20.64	20.92	21.12	20.84	21.55	9.61	8.08	3.63	7.18	4.78	0.96	0.34	0.02	19.98	19.4	1 21.6	1 19.33	13.16	6 12.4	0 12.00	0.03	0.01	6.21	3.57	1.68	0.36	0.46	21.23	1.44
Cr <sub>2</sub> O <sub>3</sub>	0.07	0.00	0.01	0.00	0.00	0.01	0.10	0.04	0.00	0.01	0.04	0.04	0.00	0.00	0.04	0.00	0.13	0.00	0.0	5 0.02	3.01	1 3.6	7 3.64	0.02	0.04	2.00	1.31	9.19	0.18	2.81	0.00	0.02
FeO	0.00	6.90	13.69	25.01	27.00	16.72	23.39	19.16	18.05	17.44	15.86	19.99	19.48	23.05	4.84	4.74	30.06	28.89	9 26.0	3 14.37	7.97	7 9.3	8 9.32	3.41	2.91	11.23	9.99	0.17	5.45	0.07	45.80	30.12
MnO	0.31	0.28	19.38	5.34	4.08	13.20	8.52	7.30	0.13	0.14	0.21	0.09	0.11	0.19	0.10	0.18	0.03	0.42	2 0.4	0.28	0.08	8 0.0	4 0.12	0.02	0.02	0.11	0.13	31.85	0.00	38.34	19.05	63.53
MgO	0.03	0.03	0.29		0.94	0.34	0.73		9.24	10.18	12.42	9.47		9.07	21.27	21.54	11.76				29.37	7 28.6		30.03	29.70	30.26	31.08	0.00	37.19	0.04	0.45	1.65
CaO	0.01	22.94	8.38	9.79	8.88	10.58	8.68	14.73	9.81	10.75	11.53	10.97	11.19	12.08	12.54	12.26	0.33	0.00	0.0	0.00	0.06	6 0.0		0.02	0.02	0.04	0.07	0.06	0.00	0.01	11.91	1.60
Na <sub>2</sub> O	11.12	0.18	0.04	0.14	0.07	0.05	0.09	0.03	2.54	1.97	0.88	1.67	1.30	0.22	0.23	0.12	0.04	0.07	7 0.0	0.00	0.02	2 0.0	1 0.02	0.00	0.07	0.00	0.00	0.00	0.05	0.00	0.01	0.00
K <sub>2</sub> O	0.06	0.04	0.01	0.01	0.02	0.01	0.00	0.05	0.53	0.31	0.14	0.37	0.23	0.11	0.05	0.04	0.00	0.04	4 0.0	1 0.05	0.04	4 0.0	2 0.01	0.01	0.00	0.02	0.04	0.42	0.00	0.11	0.03	0.05
Total	100.14	94.98	99.39	97.51	98.07	98.15	98.84	100.07	94.97	95.95	95.62	98.27	96.33	98.22	96.10	96.19	88.22	88.20	88.7	85.07	85.02	2 88.3	7 88.51	96.07	94.84	87.32	86.37	85.05	87.28	86.18	99.38	98.97
Oxygen	8	12.5	12		12	12			23	23		2	3 23		23		14			4 1		14 1	14 14		11	7	7	7	7	7	8	8
Si	3.00	3.03	2.94	2.92	2.92	2.91	2.94	2.88	6.84	7.02	7.53	7.15		7.82	7.97		2.75							3.98	3.99	1.83	1.96	2.05	2.05	2.08	0.01	0.00
Ti	0.00	0.01	0.01		0.01	0.01	0.01	0.02	0.02	0.03	0.01	0.01	0.00	0.00	0.00		0.00							0.00	0.00	0.00	0.00	0.00	0.00	0.00	0.02	0.01
Al	1.01	2.54	2.02		2.00	2.02	1.98	2.01	1.73	1.43	0.64	1.25		0.17	0.03		2.50				1.53			0.00	0.00	0.36	0.21	0.10	0.02	0.03	0.78	0.06
Cr = 3+	0.00	0.00	0.00		0.00	0.00	0.01	0.00	0.00	0.00	0.01	0.00		0.00	0.00		0.01	0.00			0.24			0.00	0.00	0.08	0.05	0.02	0.01	0.00	0.00	0.00
re-	-	0.08	0.09	0.09	0.09	0.09	0.08	0.08	0.16	0.16	0.16	0.15	0.16	0.16	0.00		0.11	0.1			0.10	0.1		-	-	-	-	-	-	-	1.13	0.86
Fe*	0.00	0.46	0.84	1.71	1.83	1.13	1.58	1.27	2.30	2.19	1.97	2.47	2.45	2.87	0.76		2.67	2.5						0.18	0.16	0.46	0.41	0.38	0.22	0.11	0.05	1.05
Mn	0.01	0.02	1.33		0.28	0.91	0.58	0.49	0.02	0.02	0.03	0.01	0.01	0.02	0.04		0.00							0.00	0.00	0.00	0.01	0.01	0.00	0.00	0.45	0.87
Co	0.00 0.00	0.00 1.98	0.04		0.11	0.04	0.09	0.06 1.25	2.10 1.60	2.27 1.73	2.75 1.83	2.08 1.74	2.25 1.80	2.01 1.93	4.38 1.78		1.86							2.85 0.00	2.85 0.00	2.21 0.00	2.27 0.00	2.34 0.00	2.64 0.00	2.68 0.00	0.01 0.55	0.05
Na	0.00	0.03	0.73	0.00	0.77	0.92	0.75	0.00	0.75	0.57	0.25	0.48		0.06	0.08		0.04	0.00						0.00	0.00	0.00	0.00	0.00	0.00	0.00	0.00	0.09
K	0.00	0.00	0.00		0.00	0.01	0.00	0.00	0.10	0.06	0.23	0.40	0.04	0.00	0.00	0.10	0.00				0.00	1 0.0		0.00	0.00	0.00	0.00	0.00	0.00	0.00	0.00	0.00
Total	4 97	8.16	8.00		8.03	8.03	8.03	8.06	15.62	15.47	15.20	15.41		15.06	15.06		9.95				9.97	7 9.8		7.02	7.01	4.95	4.91	4.89	4 94	4.91	3.00	3.00

 Table 4. Whole-rock compositions of the reaction zones.

Sample No.		150808S1	150808S2	150808S3	190808Sc	150808S4	170808S1c	150808S5	150808S6	150808S7	150808S8	150808S9	150808S10	150808S11
Rock Type		Pelite	Albite rock	Albite rock	Muscovite rock	Chlorite rock	Chlorite rock	Tremolite schist	Talc schist	Talc schist	Talc + Serpentine rock	Talc + Serpentine rock	Serpentinite	Serpentinite
Oxide (wt%)											1001	1001		
	SiO <sub>2</sub>	64.87	70.11	62.24	43.81	26.49	26.16	47.23	59.20	51.39	51.77	43.93	42.60	41.46
	TiO <sub>2</sub>	0.52	0.39	0.50	0.85	1.50	1.07	0.01	0.00	0.00	0.00	0.01	0.03	0.0
	$Al_2O_3$	16.24	15.15	19.33	29.27	21.77	21.25	7.25	1.12	4.13	1.39	1.45	0.99	0.49
	Fe <sub>2</sub> O <sub>3</sub>	5.04	3.19	4.20	7.18	17.97	17.36	6.48	4.86	6.71	7.10	7.84	7.68	7.27
	MnO	0.16	0.06	0.07	0.13	0.38	0.35	0.20	0.03	0.06	0.08	0.14	0.17	0.0
	MgO	2.37	1.69	1.91	3.48	18.74	20.93	25.45	29.20	29.05	31.04	34.97	35.93	37.95
	CaO	1.13	0.73	1.08	1.51	2.14	0.89	6.85	0.14	0.19	0.14	0.13	0.13	0.12
	Na <sub>2</sub> O	3.47	5.41	9.27	0.33	0.08	0.30	0.37	0.04	0.08	0.20	0.04	0.03	0.10
	K <sub>2</sub> O	2.85	1.55	0.13	8.58	0.02	0.02	0.03	0.01	0.01	0.01	0.01	0.01	0.0
	$P_2O_5$	0.09	0.06	0.06	0.01	0.12	0.12	0.00	0.00	0.00	0.00	0.00	0.00	0.00
	LOI	2.64	2.32	1.31	4.56	10.17	11.20	5.79	5.10	6.75	7.76	11.06	11.27	11.45
	Total	99.39	100.65	100.09	99.71	99.38	99.65	99.65	99.70	98.38	99.52	99.58	98.83	98.93
Elements (mg/	/kg)													
	V	84.2	35.1	63.0	128.8	197.2	141.8	35.7	3.1	26.0	7.3	9.5	13.8	8.5
	Cr	38.5	18.0	31.9	100.9	114.2	92.1	4506.3	1713.1	9286.6	3839.4	3280.6	4208.9	3366.5
	Ni	29.0	21.6	20.2	35.4	61.5	46.7	2084.6	2521.9	2595.3	2402.9	1718.0	2436.6	1986.1
	Cu	46.0	32.1	26.5	29.3	17.4	23.2	18.8	83.4	13.4	113.8	11.6	13.7	13.3
	Zn	88.4	54.1	73.4	94.2	229.8	217.2	72.2	62.6	88.9	103.4	68.4	79.1	43.2
	As	4.4	3.3	6.6	3.4	2.1	b.d.l.	b.d.l.	b.d.l.	b.d.l.	b.d.l.	b.d.l.	3.8	5.3
	Sn	3.0	3.1	2.7	8.2	2.7	1.4	b.d.l.	b.d.l.	b.d.l.	b.d.l.	b.d.l.	b.d.l.	b.d.l
	La	30.60	25.44	32.68	46.53	64.48	52.17	0.32	0.12	0.76	0.75	0.40	0.46	0.24
	Се	66.19	52.49	67.51	98.05	137.40	111.99	0.72	0.13	0.36	0.87	0.69	1.02	0.48
	Pr	7.02	5.76	7.54	10.83	14.92	11.72	0.15	0.02	0.09	0.15	0.08	0.12	0.06
	Nd	26.12	21.29	27.24	39.54	55.51	43.02	0.13	0.02	0.09	0.13	0.33	0.12	0.19
		5.18		5.57				0.43		0.04		0.09	0.49	0.06
	Sm		4.36		8.11	11.02	9.33		0.02		0.13			
	Eu	0.96	0.85	1.07	1.72	3.19	1.24	0.02	0.00	0.01	0.01	0.00	0.00	0.00
	Gd	4.62	3.70	4.95	7.35	9.85	8.20	0.59	0.02	0.08	0.15	0.09	0.11	
	Tb	0.75	0.62	0.84	1.20	1.62	1.36	0.12	0.00	0.01	0.02	0.02	0.03	0.0
	Dy	4.39	3.45	4.79	7.23	9.20	7.66	0.72	0.02	0.08	0.14	0.13	0.14	0.06
	Но	0.88	0.71	0.99	1.48	1.86	1.48	0.14	0.00	0.02	0.03	0.03	0.03	0.0
	Er	2.50	1.99	2.81	4.27	5.05	3.97	0.40	0.01	0.06	0.11	0.08	0.10	0.03
	Tm	0.40	0.32	0.45	0.68	0.78	0.58	0.06	0.00	0.01	0.02	0.01	0.02	0.0
	Yb	2.62	2.04	2.86	4.44	4.91	3.54	0.35	0.02	0.06	0.12	0.08	0.10	0.03
	Lu	0.39	0.32	0.45	0.71	0.75	0.52	0.04	0.00	0.01	0.02	0.01	0.02	0.0
	Ва	401.38	404.76	80.39	3515.11	5.71	1.06	0.58	0.19	0.94	1.30	1.83	2.82	0.47
	Th	13.38	10.56	13.55	19.78	27.04	19.99	0.26	0.06	0.14	0.09	0.27	0.27	0.03
	Nb	11.17	9.55	12.52	18.74	34.65	23.84	0.08	0.03	0.06	0.15	0.16	0.21	0.13
	Υ	24.76	20.20	28.11	42.51	52.44	40.49	4.30	0.11	0.63	1.10	0.84	1.03	0.3
	Hf	4.46	4.94	5.84	7.81	9.63	7.27	0.04	0.01	0.02	0.05	0.12	0.07	0.02
	Та	0.89	0.76	1.06	1.36	2.15	1.53	0.00	0.00	0.01	0.02	0.02	0.02	0.0
	U	2.90	2.40	3.12	4.36	5.27	3.71	0.02	0.02	0.11	0.08	0.04	0.04	0.0
	Pb	27.37	17.85	35.20	29.85	23.62	12.45	2.55	0.01	0.03	0.49	0.06	0.10	0.2
	Rb	114.96	67.43	3.49	294.89	0.79	0.43	0.11	0.08	0.20	0.13	0.13	0.13	0.0
	Cs	6.79	9.98	2.60	15.11	0.33	0.47	0.09	0.07	0.30	0.37	0.25	0.32	0.04
	Sr	137.70	58.36	94.45	548.84	361.13	15.28	22.39	0.09	0.62	0.87	0.35	0.22	0.46
	Sc	11.72	8.04	11.50	23.78	27.29	18.49	2.34	1.47	3.45	3.44	7.09	5.74	4.00
	Zr	154.52	176.81	206.99	280.74	345.95	259.93	1.04	0.32	0.50	1.72	5.65	2.78	0.59
	Ti/Cr	80.7	131.4	94.7	50.2	79.0	69.9	0.0	0.0	0.0	0.0	0.0	0.0	0.0
	Eu/Eu*	0.60	0.65	0.62	0.68	0.93	0.43	0.10	0.10	0.39	0.22	0.07	0.0	0.19
	Eu/Eu	0.00	0.05	0.02	0.08	0.93	0.43	0.10	U. IU	0.39	U.22	0.07	0.11	U. I
	osity (%)	2.3	2.5	1.5	0.1	1.0	1.0	1.4	1.2	1.3	1.1	0.5	0.5	0.3
Density	(g cm <sup>-3</sup> )	2.77	2.68	2.67	2.91	2.90	2.90	2.91	2.81	2.81	2.76	2.69	2.66	2.68

# Supplementary material

# Metasomatism at a metapelite-ultramafic rock contact at the subduction interface: Insights into mass transfer and fluid flow at the mantle wedge corner

Ryosuke Oyanagi<sup>1, 2\*</sup>, Masaoki Uno<sup>3</sup>, Atsushi Okamoto<sup>3</sup>

# \*Corresponding author:

<u>Tel.: +81-46-867-9667</u> <u>oyanagir@kokushikan.ac.jp</u>

# This file contains

Supplementary Figure S1 – S11 Supplementary Table S1– S2 Supplementary Text 1

<sup>&</sup>lt;sup>1</sup> School of Engineering and Science, Kokushikan University, Tokyo 154-8515, Japan

<sup>&</sup>lt;sup>2</sup> Research Institute for Marine Geodynamics, Japan Agency for Marine-Earth Science and Technology (JAMSTEC), Yokosuka 237-0061, Japan

<sup>&</sup>lt;sup>3</sup> Department of Environmental Studies for Advanced Society, Graduate School of Environmental Studies, Tohoku University, Sendai 980-8579, Japan

# **Supplementary Figures**

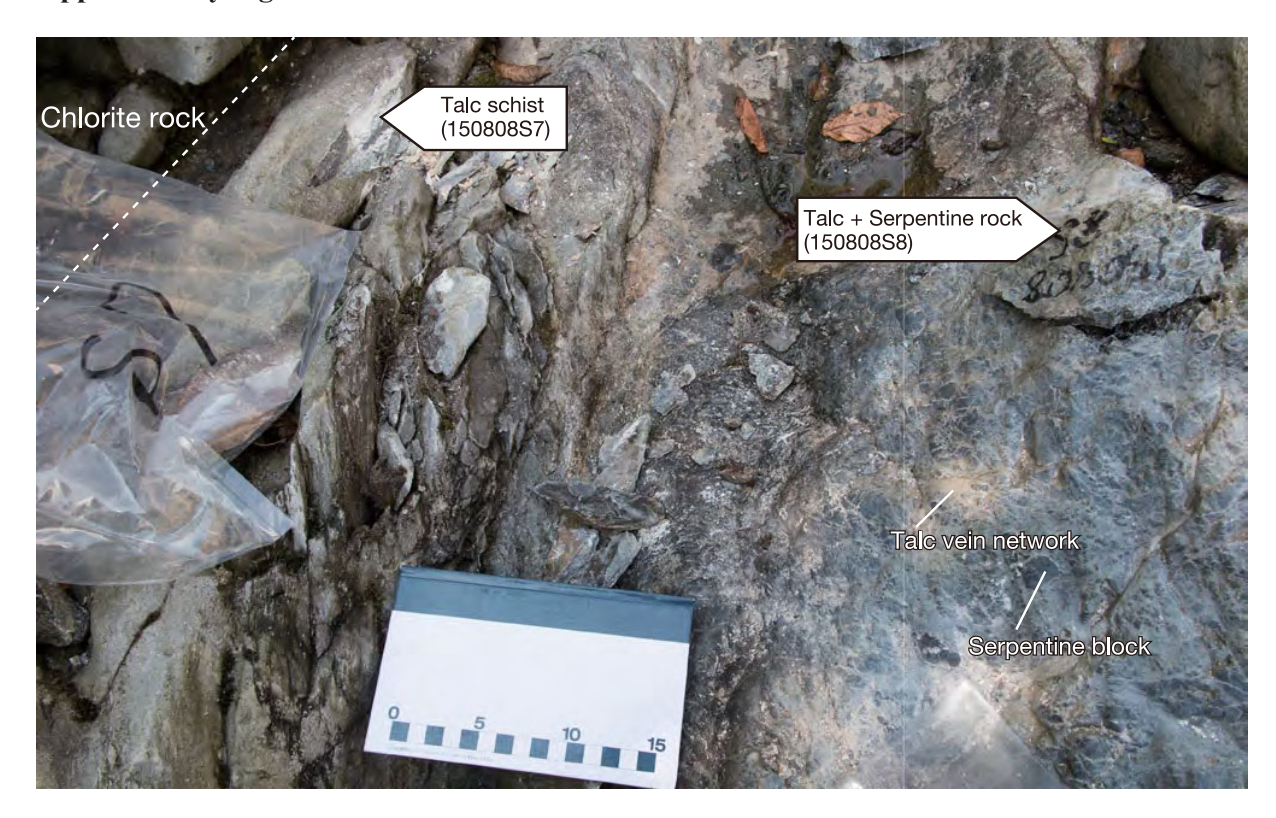


**Figure S1** (a and b) Photomicrograph showing the boundary between chlorite rock and talc schist. In the talc + serpentine rock, talc vein networks are observed.

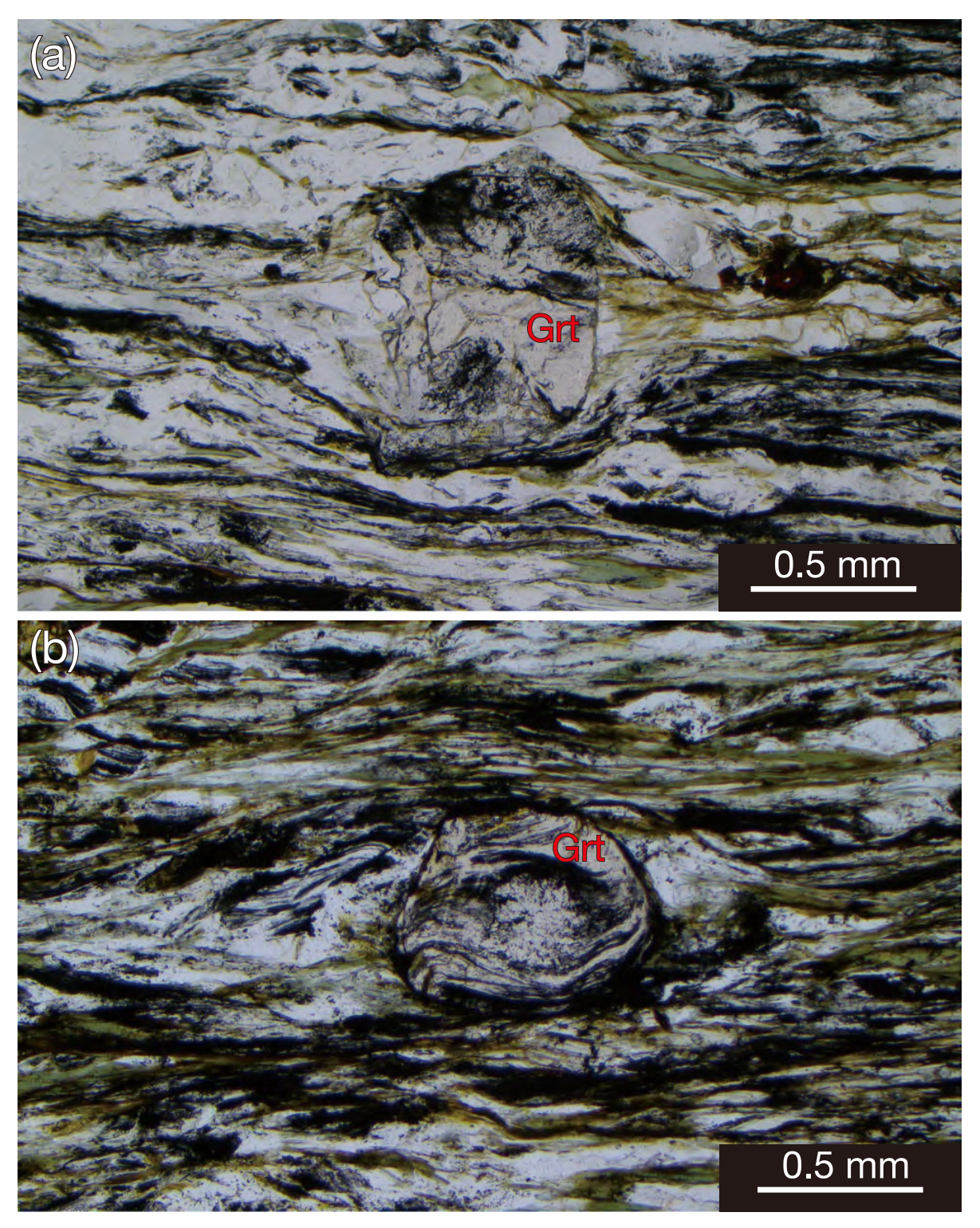


**Figure S2** (a and b) Photomicrograph of garnet in the pelitic schist (sample 150808S1) under plane-polarized light.

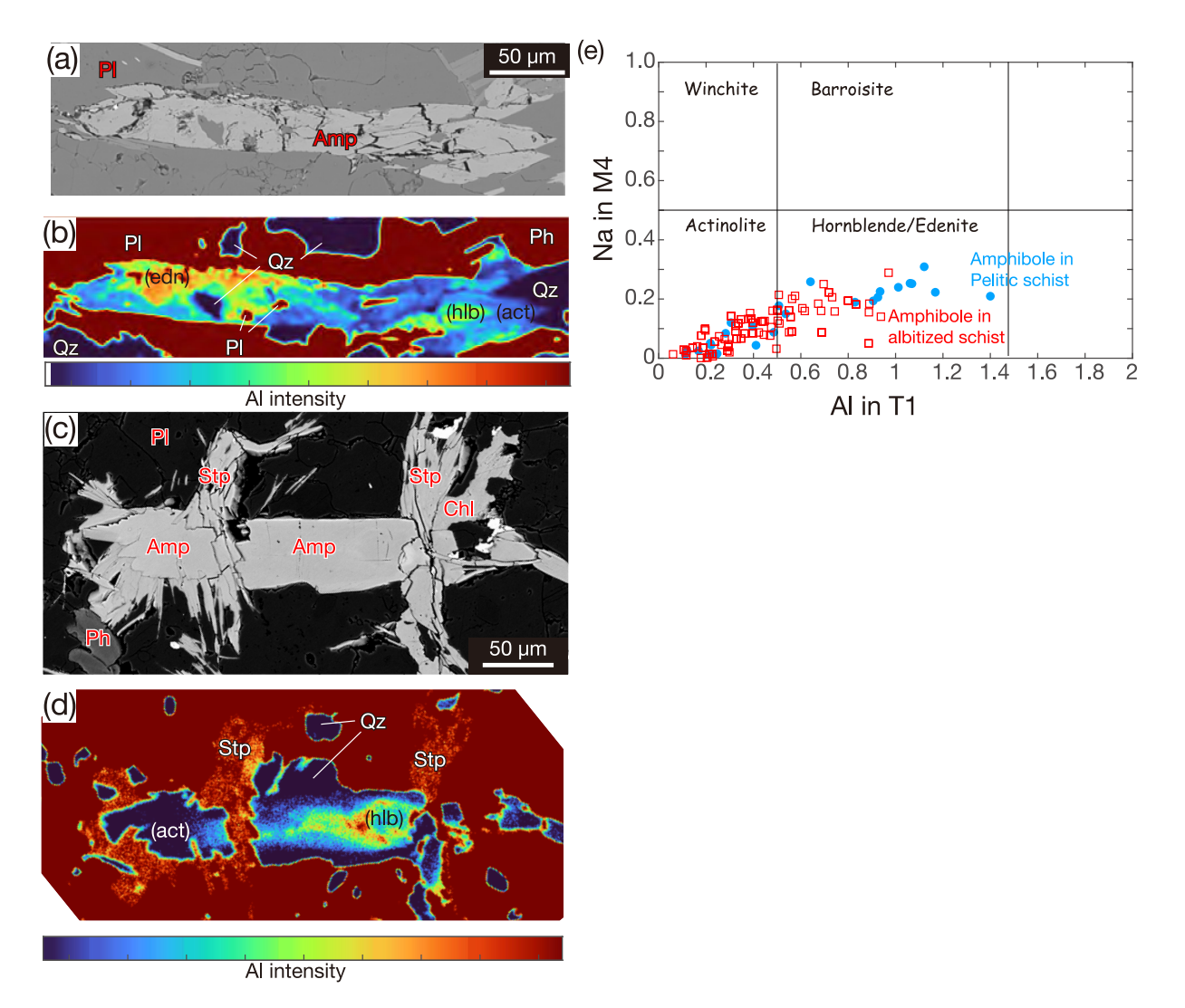
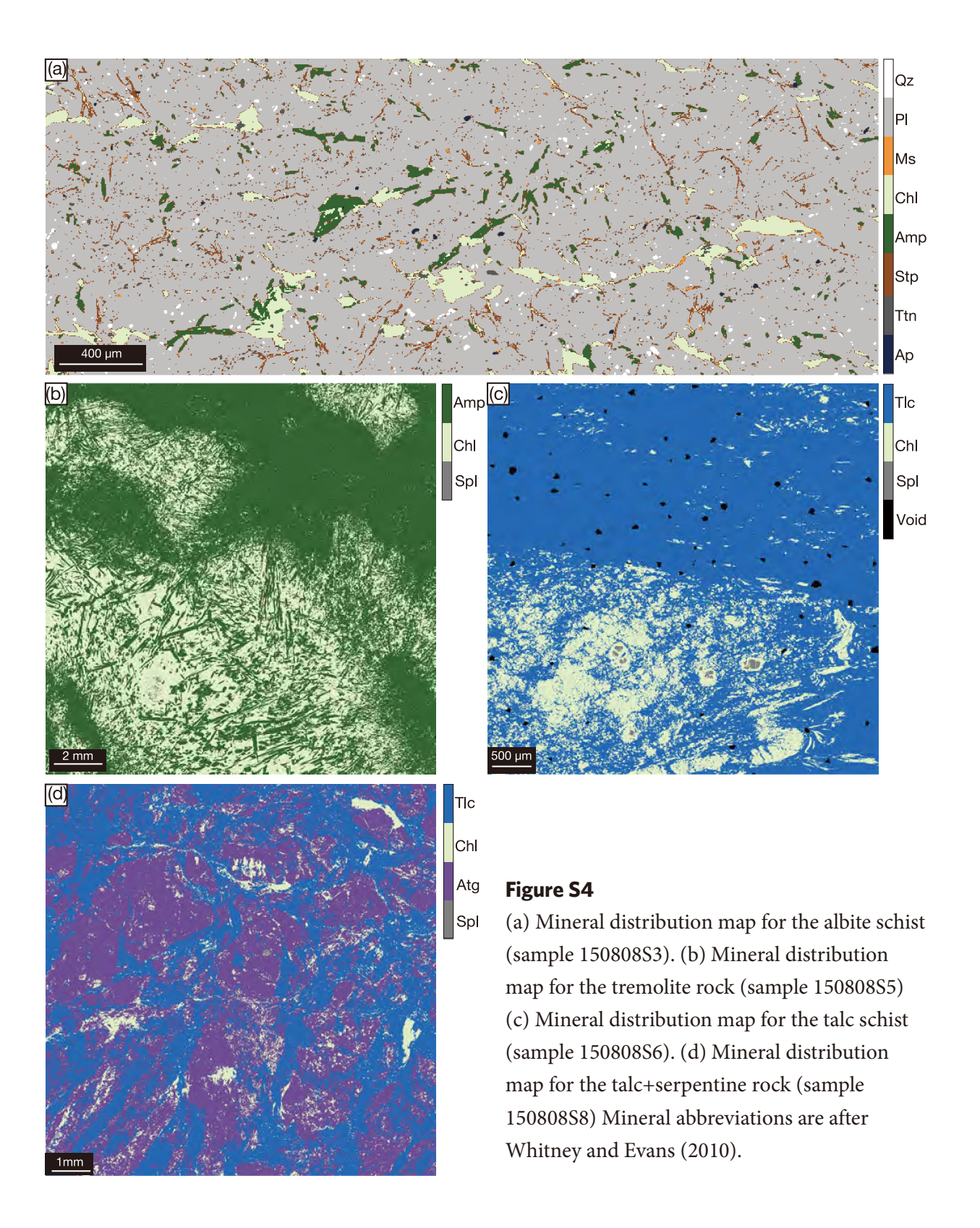
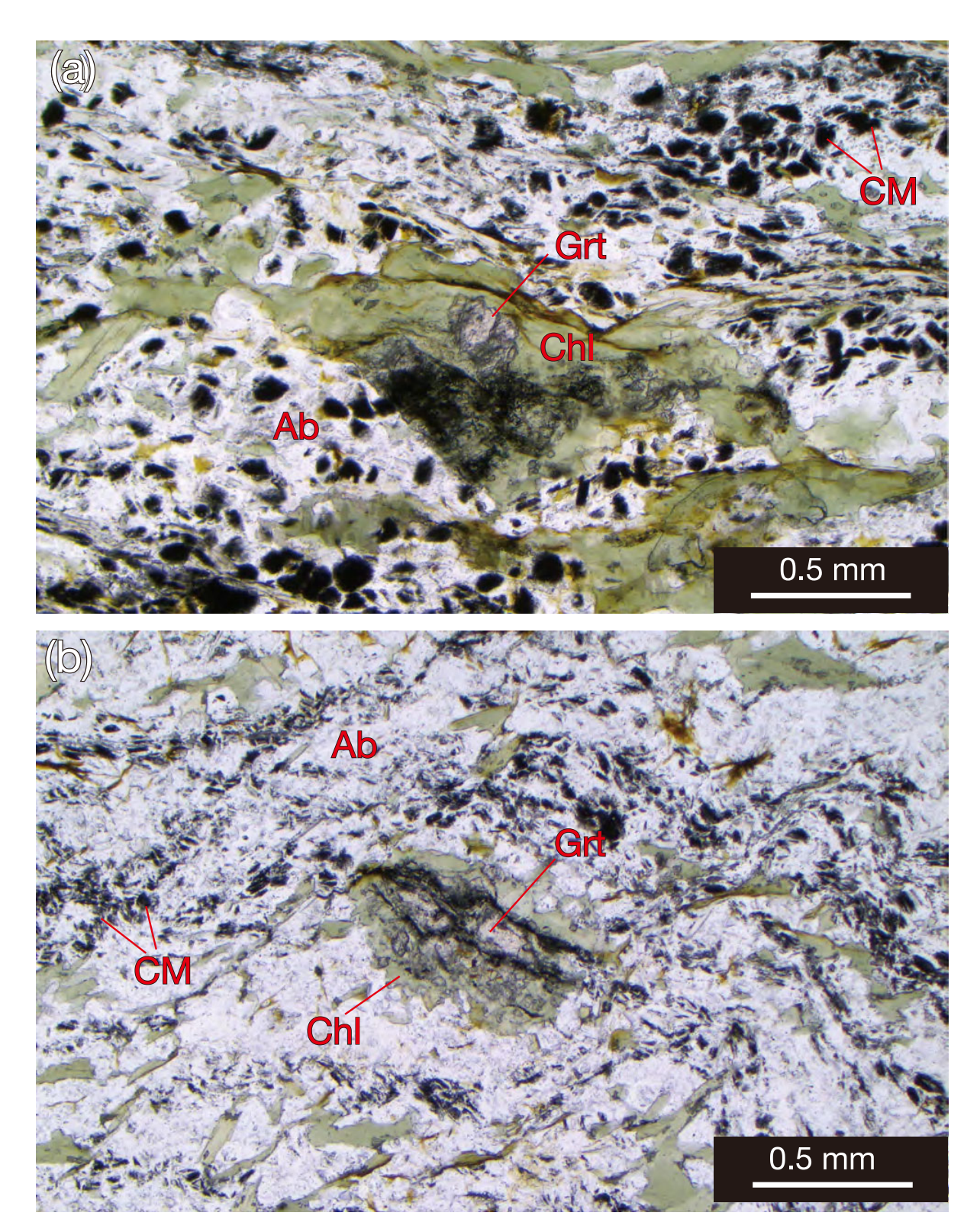


Figure S3

(a, b) BSE images (a) and its aluminum X-ray maps (b) of amphibole in the pelitic schist. (c, d) BSE images (c) and its aluminum X-ray maps (d) of amphibole in the albite schist. (e) Plot of Al in the T1 site vs Na in the M4 site of amphibole.





**Figure S5** (a and b) Photomicrograph of garnet in the albite schist (sample 170808S1a\_up) under plane-polarized light.

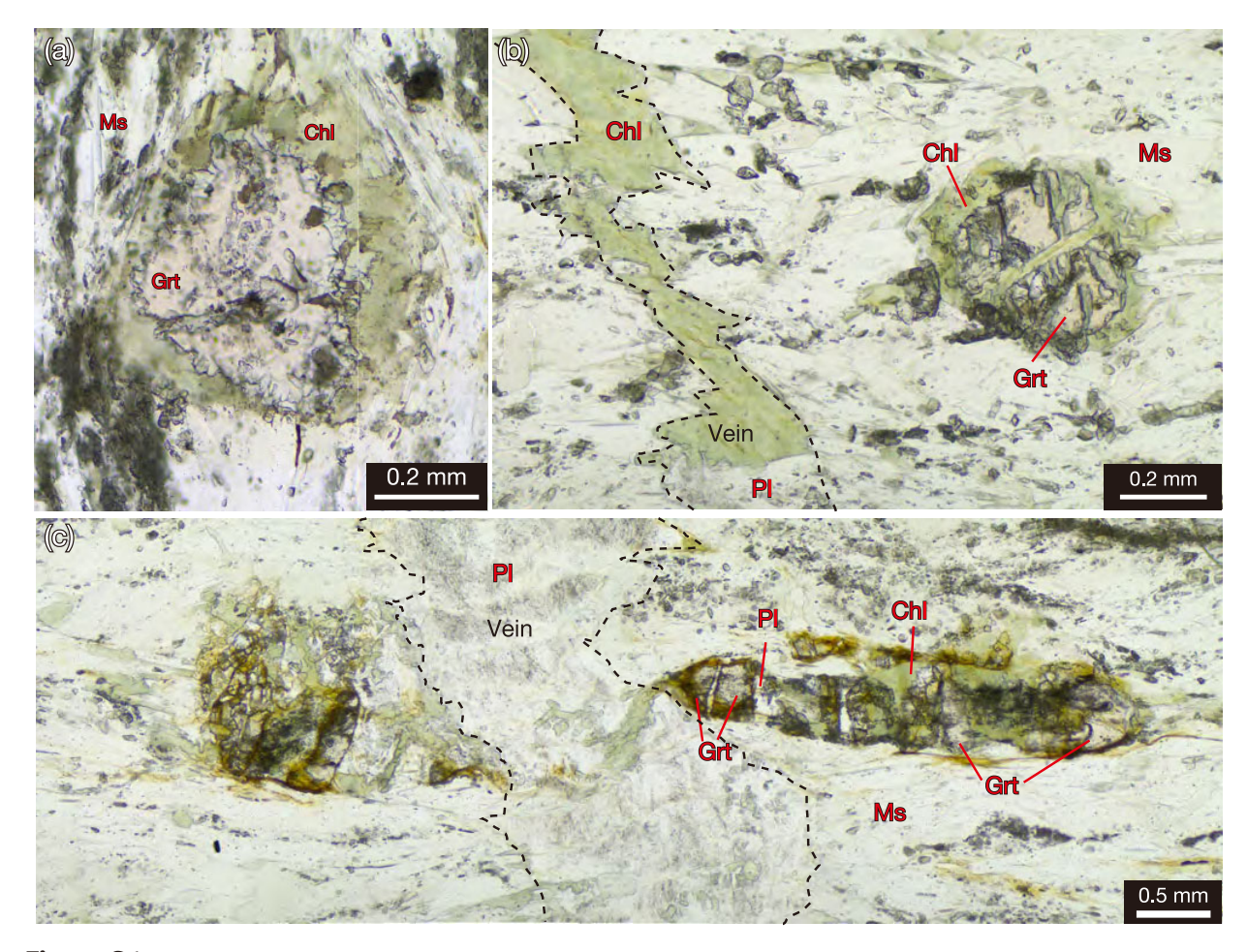


**Figure S6**Photomicrograph of garnet in the muscovite rock (sample 150808S1a\_low) far from vein (a) and around vein (b and c) under plane-polarized light. The black dotted line in (b) and (c) is boundary between vein and host rock.

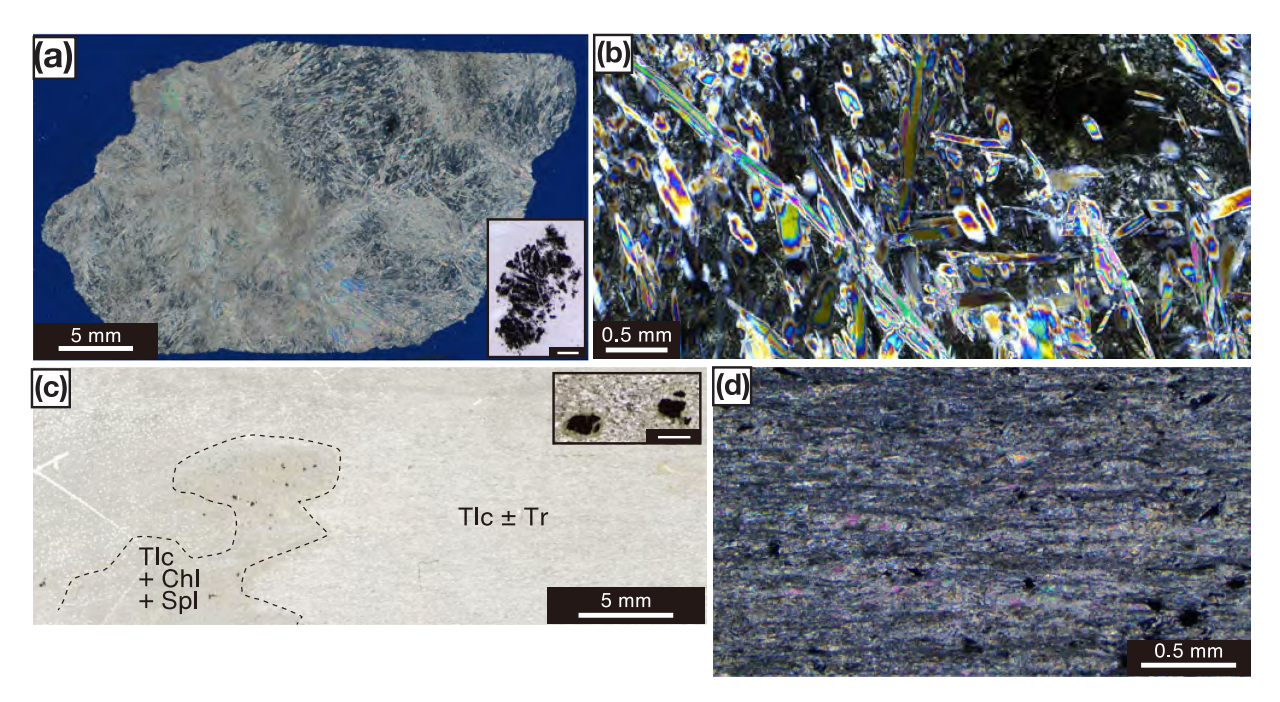
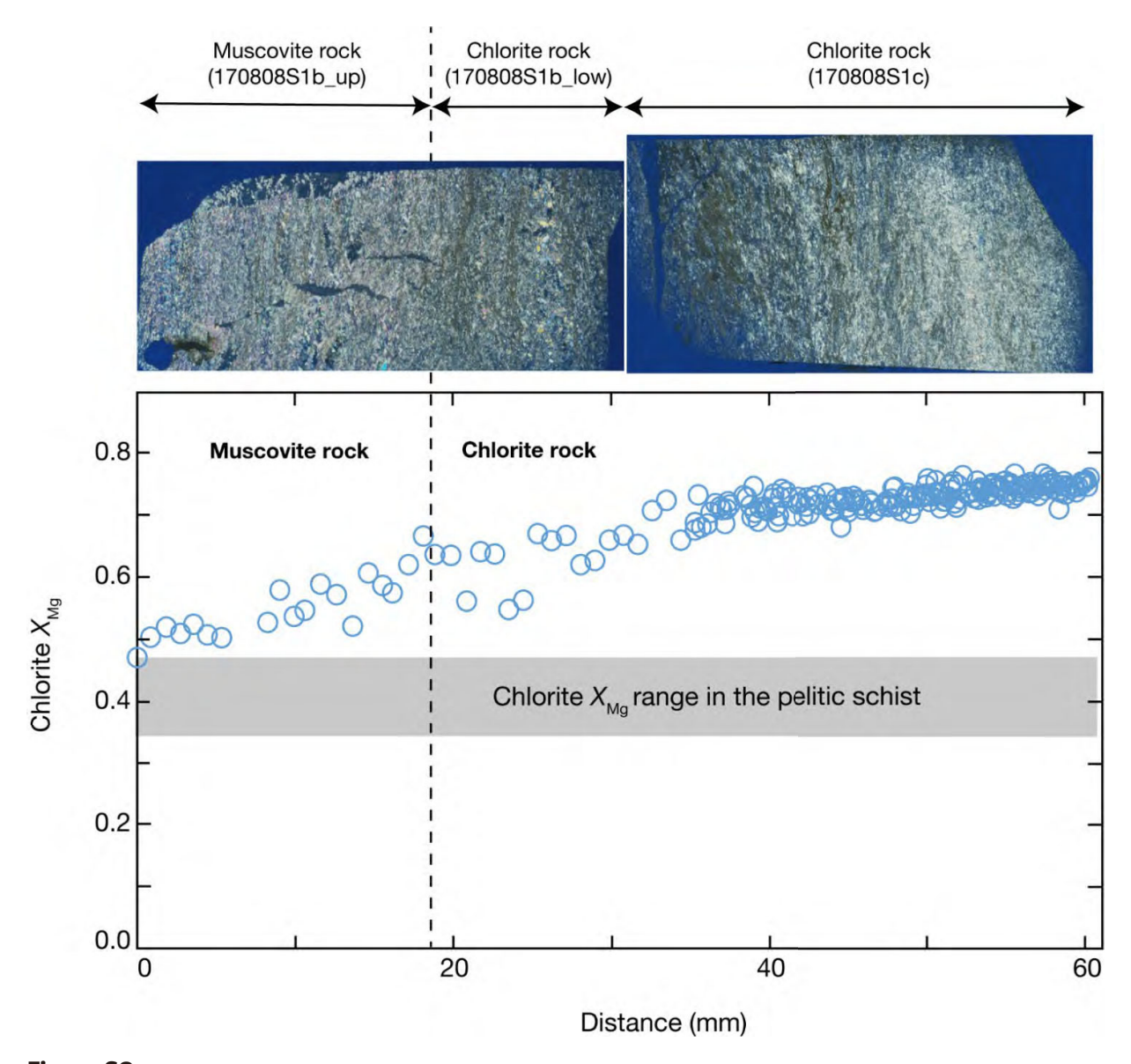


Figure S7

(a)Thin section image of tremolite schist (sample 150808S5) under cross-polarized light. Inserted figure is spinel grain in the tremolite rock under cross-polarized light. Scale bar is 0.2 mm. (b) Representative photograph of tremolite crystal in the tremolite schist under cross-polarized light. (c) Thin section image of talc schist (sample 150808S6) under plane-polarized light. The inset is a spinel grain in the talc schist under plane-polarised light. Scale bar is 0.2 mm. (d) Photomicrograph of highly aligned talc (cross-polarized light).



**Figure S8** Chlorite  $X_{Mg}$  with distance from the muscovite rock to chlorite rock.

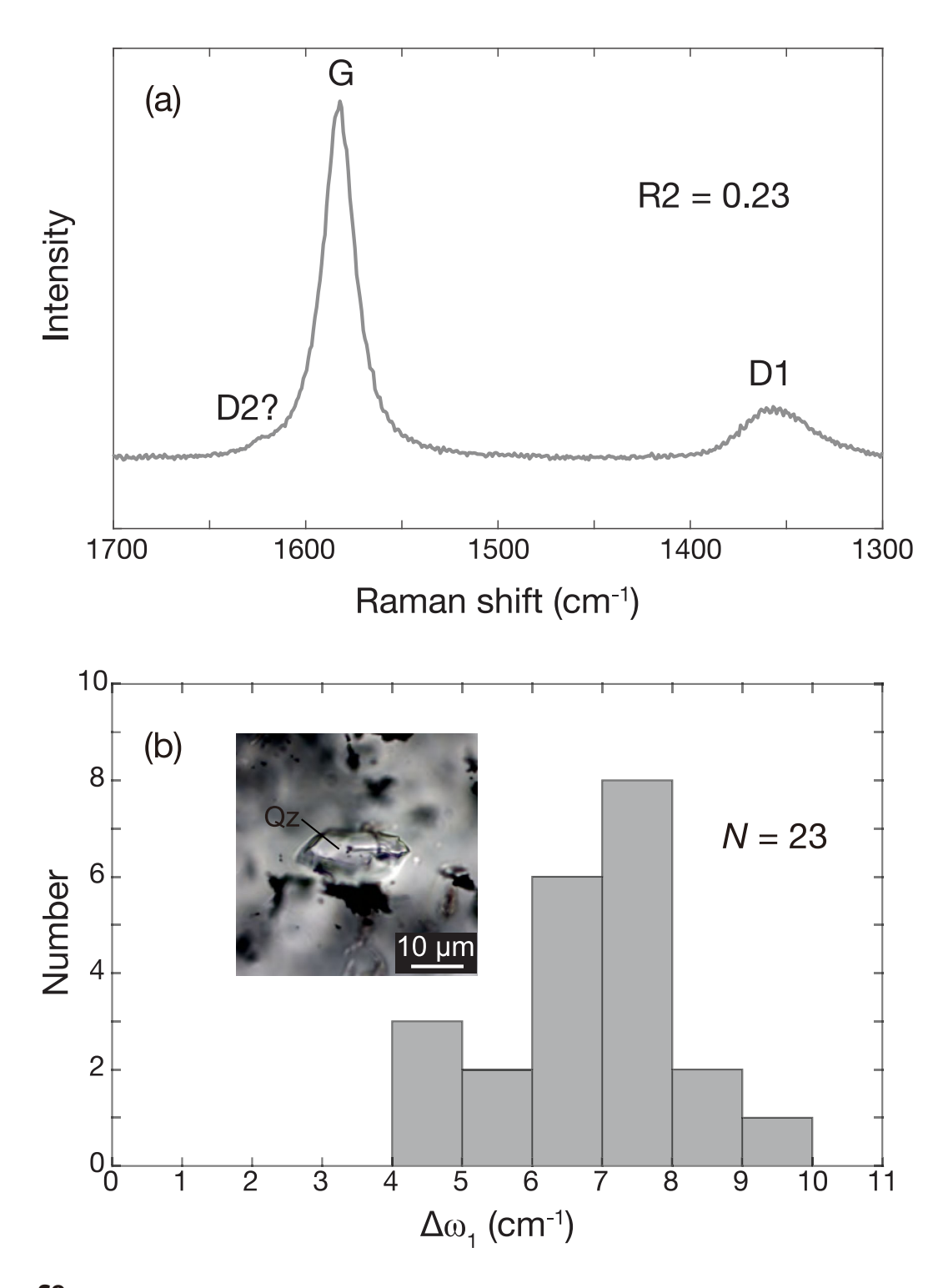


Figure S9 (a) Representative Raman spectra of carbonaceous matter in the pelitic schist. (b) Histogram of  $\Delta\omega_1$  values obtained from the quartz inclusions in the garnet in the pelitic schists. The inset photograph is a representative image of quartz inclusion hosted by the garnet.

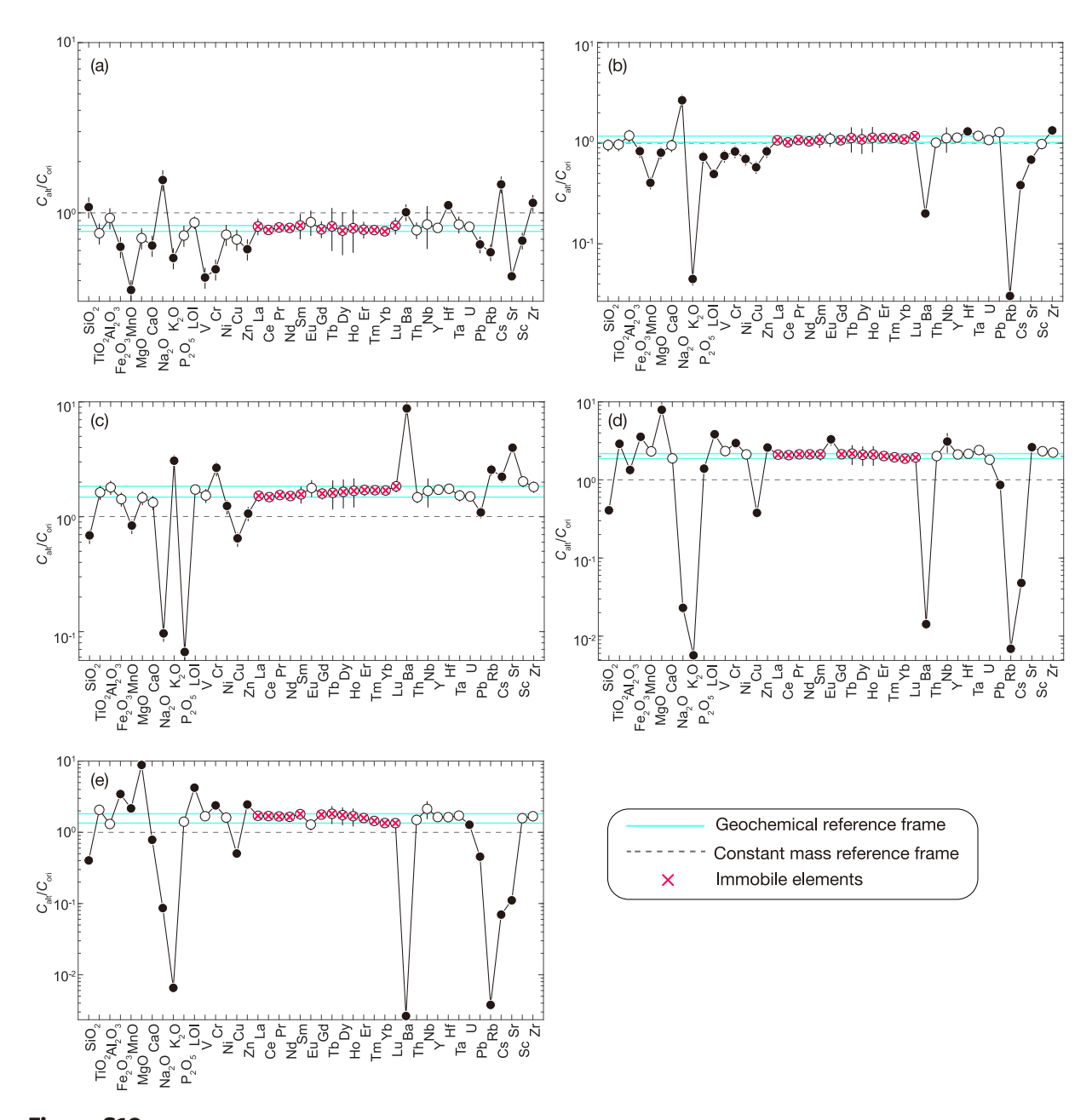
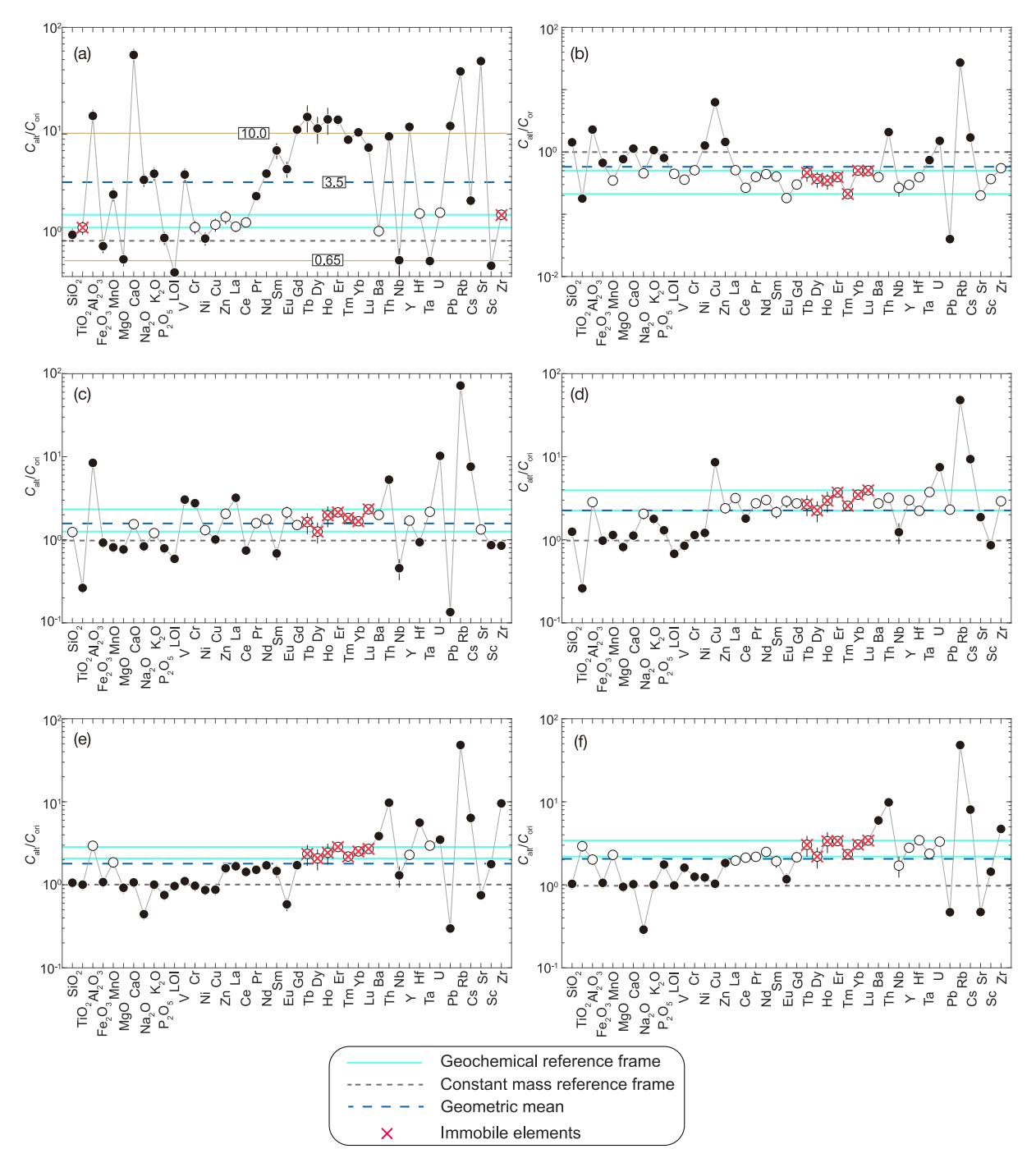


Figure S10.

Major and trace element concentration ratios of the altered metasediments, specifically for albite schist samples (a) 150808S2 and (b) 150808S3, (c) muscovite rock (sample 190808Sc), and chlorite rock samples (d)150808S4 and (e) 170808S1c. The composition of the pelitic schist (sample 150808S1; Table 1) was used as the composition of the protolith ( $C_{ori}$ ). Error bars are  $\pm 2\sigma$ . Where error bars are not shown, they are smaller than the symbol size. The dashed gray horizontal line indicates the concentration ratio assuming no mass transfer. Solid horizontal lines show the range of the immobile reference frame. White circles are elements that fall within the immobile reference frame (indicating no evidence for gain or loss during alteration), elements with black circles fall above (indicating gain during alteration) or below (indicating loss during alteration) the immobile reference frame. The  $\times$  symbols indicate elements used to define the immobile reference frame.



**Figure S11.** Major and trace element concentration ratios of the altered serpentinite, specifically for (a) tremolite schist (sample 150808S5), talc schist samples (b) 150808S6 and (c) 150808S7, and talc + serpentine rock samples (d) 150808S8, (e) 150808S9, and (f) 150808S10. The composition of the serpentinite sample 150808S11 (Table 1) was used as the composition of the protolith ( $C_{ori}$ ). The numbers in boxes in (a) are the concentration ratios for other potential geochemical reference frames (see the supplementary text for details). Error bars are  $\pm 2\sigma$ . Where error bars are not shown they are smaller than the symbol size. The dashed gray horizontal lines indicate the concentration ratios with no mass transfer. Solid horizontal lines show the range of the immobile reference frame. White circles are elements that fall within the immobile reference frame (indicating no significant change during alteration), elements with black circles fall above (indicating gain during alteration) or below (indicating loss during alteration) the immobile reference frame. The × symbols indicate elements that were used to define the immobile reference frame.

**Table S1.** Summary of amphibole composition in the pelitic schist and result of thermobarometry.

Sample	150808S1								
Lithology	Pelitic schist Amp. core								
wt%									
SiO <sub>2</sub>	44.87	45.45	44.66	46.22	49.16	47.52	46.83	45.90	47.76
TiO <sub>2</sub>	0.20	0.20	0.14	0.18	0.00	0.25	0.25	0.14	0.04
$Al_2O_3$	9.61	9.27	9.66	9.71	6.49	7.20	8.08	8.71	8.51
FeO	18.05	17.69	17.99	18.19	16.89	17.18	17.44	17.93	17.91
MnO	0.13	0.12	0.13	0.14	0.06	0.14	0.14	0.17	0.19
MgO	9.24	9.47	9.48	9.39	10.87	10.58	10.18	9.76	9.97
CaO	9.81	10.33	10.41	10.48	10.53	10.92	10.75	10.25	11.07
Na₂O	2.54	2.34	2.50	2.26	1.56	1.89	1.97	2.05	1.96
K <sub>2</sub> O	0.53	0.38	0.37	0.33	0.23	0.27	0.31	0.36	0.34
Total	94.97	95.24	95.34	96.89	95.78	95.94	95.94	95.27	97.75
Cations per 2	23 oxygens								
Si	6.88	6.85	6.75	6.85	7.27	7.07	6.98	6.91	6.99
Ti	0.02	0.02	0.02	0.02	0.00	0.03	0.03	0.02	0.00
$Al^{iv}$	1.13	1.15	1.25	1.15	0.73	0.93	1.02	1.09	1.01
$Al^{vi}$	0.61	0.50	0.47	0.54	0.40	0.33	0.40	0.46	0.46
Fe <sup>3+</sup>	0.25	0.25	0.25	0.24	0.24	0.24	0.24	0.25	0.24
Fe <sup>2+</sup>	2.06	2.23	2.27	2.25	2.09	2.14	2.17	2.26	2.19
Mn	0.02	0.02	0.02	0.02	0.01	0.02	0.02	0.02	0.02
Mg	2.11	2.13	2.14	2.07	2.40	2.35	2.26	2.19	2.18
Ca	1.61	1.67	1.69	1.66	1.67	1.74	1.72	1.65	1.74
Na	0.75	0.69	0.73	0.65	0.45	0.54	0.57	0.60	0.56
K	0.10	0.07	0.07	0.06	0.04	0.05	0.06	0.07	0.06
Sum	15.54	15.56	15.65	15.52	15.29	15.45	15.47	15.51	15.46
Plagioclase o	composition								
$X_{ab}$	0.99	0.99	0.99	0.99	0.99	0.99	0.99	0.99	0.99
Result of the	hornblende-pl	agioclase-qua	artz thermoba	rometer (Holla	and & Blundy	(1994), Therm	ometer A)		
0.1 GPa	547	546	560	541	537	575	569	569	542
0.5 GPa	554	552	563	551	533	566	565	570	545
1.0 GPa	563	560	567	564	529	554	561	570	550
1.5 GPa	572	567	571	577	525	543	557	571	554

**Table S2.** Calculated immobile reference frame with mass and volume change during the reaction zone.

		C <sup>alt</sup> ref	/ C <sup>ori</sup> ref	<i>M</i> <sup>alt</sup>	/ M <sup>ori</sup>	Valt / Vori			
		Lower	Upper	Lower	Upper	Lower	Upper		
Sample	Lithology	bound	bound	bound	bound	bound	bound		
150808S2	Albite schist	0.78	0.84	1.19	1.28	1.23	1.33		
150808S3	Albite schist	1.02	1.18	0.85	0.98	0.90	1.03		
190808Sc	Muscovite rock	1.48	1.84	0.54	0.68	0.52	0.64		
150808S4	Chlorite rock	1.87	2.17	0.46	0.53	0.44	0.51		
170808S1c	Chlorite rock	1.35	1.82	0.55	0.74	0.52	0.71		
150808S5	Tremolite schist	1.33	1.75	0.57	0.75	0.52	0.69		
150808S6	Talc schist	0.21	0.50	1.99	4.73	1.90	4.51		
150808S7	Talc schist	1.26	2.33	0.43	0.80	0.41	0.76		
150808S8	Talc + Serpentine rock	2.26	3.95	0.25	0.44	0.25	0.43		
150808S9	Talc + Serpentine rock	2.08	2.85	0.35	0.48	0.35	0.48		
150808S10	Talc + Serpentine rock	2.19	3.41	0.29	0.46	0.30	0.46		

# Supplementary Text 1: Geochemical, mass, and volume changes during metasomatism

Quantitative changes in the mass of element *i* can be calculated using Eq. (1) in the main text. Using a geochemical reference frame, the ratio of the mass of altered rock to that of original rock can be calculated as follows:

$$\frac{M^{alt}}{M^{ori}} = \frac{c_{ref}^{ori}}{c_{ref}^{alt}},$$

where  $M^{\rm alt}$  and  $M^{\rm ori}$  are the mass of altered and original rock, respectively.  $c_{ref}^{Ori}$  and  $c_{ref}^{Alt}$  are the concentrations of immobile elements (the geochemical reference frame). The volume change relative to the protolith can be calculated as follows:

$$\frac{V^{alt}}{V^{ori}} = \left(\frac{M^{alt}}{M^{ori}}\right) \left(\frac{\rho^{ori}}{\rho^{alt}}\right) \left(\frac{\phi_{ori} - 1}{\phi_{alt} - 1}\right),$$

where  $V^{\rm alt}$  and  $V^{\rm ori}$  are the volume of altered and original rock, respectively, and  $\rho^{\rm alt}$  and  $\rho^{\rm ori}$  are the porosity-free densities of the altered and original rock (i.e., grain density or true density), respectively.  $\varphi_{\rm ori}$  and  $\varphi_{\rm alt}$  are the porosities of the altered and original rock, respectively. We assumed that  $(\varphi_{\rm ori} - 1)/(\varphi_{\rm alt} - 1) = 1$ , given that porosity is very low during metamorphism and  $\varphi_{\rm ori}$  and  $\varphi_{\rm alt}$  have similar values.

# 1. Metasomatism of the pelitic schist

The albite schist, muscovite rock, and chlorite rock formed from the pelitic schist. For the mass balance calculations involving these rocks, the bulk rock composition of the pelitic schist (sample 150808S1; Tables 1, 4) was used as the composition of the original rock. The high field strength elements (HFSEs; e.g., Nb, Ta, Zr, and Th) are usually assumed to be fluid-immobile and used as a geochemical reference frame (e.g., Baumgartner and Olsen, 1995; Ague and Van Haren 1996; Ague 2017). However, the Zr content could be altered if slightly more zircon crystals were included in the analyzed bulk-rock sample (i.e., the nugget effect; Penniston-Dorland and Ferry, 2008). Thus, Zr may be inappropriate as a geochemical reference frame. The present study assumed that the rare earth elements (REEs) excluding Eu would be an appropriate geochemical reference frame, given the following evidence. (i) The  $C_{\rm alt}/C_{\rm ori}$  ratios for the REEs are similar in all cases (Fig. S10a–e). (ii) The titanite layering in the pelitic schist is also observed in the albite schist, muscovite rock, and chlorite rock, suggesting the titanite from the protolith is preserved. (iii) The immobile reference frame suggests the HFSEs are largely immobile. Eu was excluded from consideration as an immobile element because the variation in the Eu anomaly in the reaction zone in the pelitic schist indicates the mobilization of Eu (Fig. 9b).

# 1.1 Albite schist

Mass balance calculations were conducted for two albite schist samples (150808S2 and 150808S3; Tables 1, 4). Using the geochemical reference frame yields  $C_{\rm alt}/C_{\rm ori}$  ratios of 0.78–0.84 (Fig. S10a) and 1.02–1.18 for samples 150808S2 and 150808S3, respectively (Fig. S10b). These results indicate that the

 $M^{alt}/M^{ori}$  ratio is 1.19–1.28 for sample 150808S2 and 0.85–0.98 for sample 150808S3 (Table S2). Major-element mass balance calculations for the two samples show a gain in Na<sub>2</sub>O and losses in Fe<sub>2</sub>O<sub>3</sub>, MnO, and K<sub>2</sub>O. Immobile elements include Th, Nb, Ta, Y, and U (Fig. S10a, b), consistent with their low solubility and immobility in hydrothermal fluids (e.g., Ague 2017). There were slight gains in Zr and Hf (Fig. S10a, b), presumably due to the nugget effect associated with zircon crystals.

#### 1.2 Muscovite rock

Mass balance calculations were conducted for one sample of the muscovite rock (190808Sc; Tables 1, 3). The geochemical reference frame indicates  $C_{\rm alt}/C_{\rm ori}$  ratios of 1.48–1.84 and  $M^{\rm alt}/M^{\rm ori}$  ratios of 0.54–0.68 (Fig. S10c; Table S2). The major-element mass balance calculations yield a gain in K<sub>2</sub>O and losses in SiO<sub>2</sub>, MnO, and Na<sub>2</sub>O. There was no significant gain or loss in the HFSEs (Hf, Ti, Zr, Nb, and Ta), Y, Th, U, or Sc (Fig. S10c). There was a gain in large-ion lithophile elements (LILEs; K, Rb, Ba, Cs, and Sr) associated with mica enrichment in the muscovite rock, and a loss in Pb.

# 1.3 Chlorite rock

Mass balance calculations were conducted for two samples of the chlorite schist (150808S4 and 170808S1c; Table 1, 3). The geochemical reference frame for samples 150808S4 and 170808S1c indicates  $C_{\rm alt}/C_{\rm ori}$  ratios of 1.87–2.17 (Fig. S10d) and 1.35–1.82 (Fig. S10e), respectively, yielding  $M^{\rm alt}/M^{\rm ori}$  ratios of 0.46–0.53 and 0.55–0.74, respectively (Table S2). The major-element mass balance calculations for the two samples yield gains in MgO and Fe<sub>2</sub>O<sub>3</sub> and losses in SiO<sub>2</sub>, Na<sub>2</sub>O, and K<sub>2</sub>O. There is a gain in TiO<sub>2</sub> in sample 150808S4 (Fig. S10d) but no significant change in TiO<sub>2</sub> in sample 170808S1c (Fig. S10e). There is no significant change in the HFSEs (including Hf, Zr, Nb, and Ta), Y, Th, U, or Sc (Fig. S10d, f). Losses in LILEs (K, Ba, Pb, Rb, and Cs) were observed.

## 2. Metasomatism of the serpentinite

The tremolite schist, talc schist, and talc + serpentine rock were formed from serpentinite. The bulk rock composition of the serpentinite sample (150808S11; Table 1, 4) was used as the composition of the original rock in the mass balance calculations. The concentration ratios in the tremolite rock (Fig. S11a) suggest four possible choices for the geochemical reference frame: (i) the geometric mean  $C_{\rm alt}/C_{\rm ori}$  ratio (3.5); (ii) the  $C_{\rm alt}/C_{\rm ori}$  ratio for the heavy REEs (HREEs; 7.4–14.5); (iii) the  $C_{\rm alt}/C_{\rm ori}$  ratio for Nb and Ta (~0.65); and (iv) the  $C_{\rm alt}/C_{\rm ori}$  ratio for Zr and Ti (1.33–1.75). Using the first of these reference frames indicates that Na<sub>2</sub>O and K<sub>2</sub>O were immobile; however, Na<sub>2</sub>O and K<sub>2</sub>O are generally fluid-mobile, and there are few immobile elements in this case (i.e., Na<sub>2</sub>O, K<sub>2</sub>O, and V). Therefore, the first potential reference frame is unlikely to be appropriate. Using the second reference frame indicates that Th ( $C_{\rm alt}/C_{\rm ori}$  = 9.5), Y (11.7), and Pb (11.9) were immobile and had similar  $C_{\rm alt}/C_{\rm ori}$  ratios. This reference frame would not be appropriate, given that the tremolite rock showed enrichment in the HREEs relative to the light REEs (LREEs), in contrast to talc schist, talc + serpentine rock, and serpentinite (Fig. 9d), suggesting significant REE fractionation and mobility. The

third and fourth reference frames use HFSEs as the geochemical reference frame. The elements with similar concentration ratios in the third reference frame are MgO (0.67), LOI (0.51), and Sc (0.58), and the fourth reference frame indicates that multiple elements were immobile (Cr, Cu, La, Ce, Ba, Hf, and U). Therefore, Zr and Ti are the best choice for the geochemical reference frame for the tremolite rock with a serpentinite protolith.

In contrast, mass transfer in the talc schist and talc + serpentine rock with a serpentinite protolith was estimated using the HREEs as the geochemical reference frame (Fig. S11b-f). This is because the serpentinite, talc schist, and talc + serpentine rock yield flat HREE patterns (Fig. 9d), suggesting the HREEs were immobile.

#### 2.1 Tremolite schist

Mass balance calculations were conducted for one sample of the tremolite schist (150808S5; Fig. S11a). The immobile reference frame indicates  $C_{\rm alt}/C_{\rm ori}$  ratios of 1.33–1.75, suggesting that the sample lost mass ( $M^{\rm alt}/M^{\rm ori}$ = 0.57–0.75) and volume ( $V^{\rm alt}/V^{\rm ori}$  = 0.52–0.69; Fig S11a; Table S2). The results show gains in Al<sub>2</sub>O<sub>3</sub>, MnO, CaO, Na<sub>2</sub>O, and K<sub>2</sub>O, and losses in SiO<sub>2</sub>, Fe<sub>2</sub>O<sub>3</sub>, and MgO. No significant changes in Cr, Cu, La, Ce, Ba, Hf, and U were observed. Loss of some HFSEs (Nb and Ta) and gain in the HREEs were observed.

#### 2.2 Talc schist

Mass balance calculation for the talc schist were conducted for two samples: 150808S6 (Fig. S11b) and 150808S7 (Fig. S11c). The two samples show different patterns of element gains and losses.

The immobile reference frame for sample 150808S7 (Fig. S11b) indicates  $C_{\rm alt}/C_{\rm ori}$  ratios of 0.21–0.50, suggesting the sample gained a significant mass ( $M^{\rm alt}/M^{\rm ori}$ = 1.99–4.73) and volume ( $V^{\rm alt}/V^{\rm ori}$  = 1.90–4.51). The results indicate gains in SiO<sub>2</sub>, Al<sub>2</sub>O<sub>3</sub>, Fe<sub>2</sub>O<sub>3</sub>, CaO, and K<sub>2</sub>O, and a loss in TiO<sub>2</sub>, with no significant change in MnO or Na<sub>2</sub>O. Gains in some HFSEs (Th, Ta, and U), Rb, and Cs, and a loss in Pb were observed. There is no conclusive evidence for changes in La–Gd and some HFSEs (Zr and Hf).

The immobile reference frame for sample 150808S7 (Fig. S11c) indicates  $C_{\rm alt}/C_{\rm ori}$  ratios of 1.26–2.33, suggesting the sample lost mass ( $M^{\rm alt}/M^{\rm ori}=0.43-0.80$ ). The results show a gain in Al<sub>2</sub>O<sub>3</sub> and losses in TiO<sub>2</sub>, Fe<sub>2</sub>O<sub>3</sub>, MnO, MgO, and Na<sub>2</sub>O, with no significant change in SiO<sub>2</sub>, CaO, or K<sub>2</sub>O. Gains in some HFSEs (Th and U), Ce, Rb, and Cs, and losses in other HFSEs (Nb, Hf, and Zr), Sm, Pb, and Sc were observed. There were no significant changes in La, Pr, Nd, Eu, Gd, Ba, Y, Ta, or Sr.

# 2.3 Talc + Serpentine rock

Mass balance calculations were conducted for three samples of the talc + serpentine rock: 150808S8 (Fig. S11d), 150808S9 (Fig. S11e), and 150808S10 (Fig. S11f).

The immobile reference frame for sample 150808S8 (Fig. S11d) indicates  $C_{\rm alt}/C_{\rm ori}$  ratios of 2.26–3.95, indicating losses in mass ( $M^{\rm alt}/M^{\rm ori} = 0.25-0.44$ ) and volume ( $V^{\rm alt}/V^{\rm ori} = 0.25-0.43$ ; Table S2). The

results show no gain in any major element, losses in SiO<sub>2</sub>, TiO<sub>2</sub>, Fe<sub>2</sub>O<sub>3</sub>, MnO, MgO, CaO, and K<sub>2</sub>O, and no significant change in Al<sub>2</sub>O<sub>3</sub> or Na<sub>2</sub>O. Gains in U, Rb, and Cs, and losses in Ce, Nb, Sr, and Sc were observed, with no significant change in La, Pr–Gd, Ba, Y, Pb, or some HFSEs (Th, Ta, and Zr).

The immobile reference frame for sample 150808S9 (Fig. S11e) indicates  $C_{\rm alt}/C_{\rm ori}$  ratios of 2.08–2.85, corresponding to losses in mass ( $M^{\rm alt}/M^{\rm ori}=0.35-0.48$ ) and volume ( $V^{\rm alt}/V^{\rm ori}=0.35-0.48$ ; Table S2). There was no gain in any major element, losses in SiO<sub>2</sub>, TiO<sub>2</sub>, Fe<sub>2</sub>O<sub>3</sub>, MgO, CaO, Na<sub>2</sub>O, and K<sub>2</sub>O, and no significant change in Al<sub>2</sub>O<sub>3</sub> or MnO. The results show gains in Ba, U, Pb, Rb, Cs, and some HFSEs (Th, Hf, and Zr), losses in La–Gd, Nb, Pb, Sr, and Sc, and no significant change in Y and some other HFSEs (Ta).

The immobile reference frame for sample 150808S10 (Fig. S11f) indicates  $C_{\rm alt}/C_{\rm ori}$  ratios of 2.19–3.41, corresponding to losses in mass ( $M^{\rm alt}/M^{\rm ori}=0.29-0.46$ ) and volume ( $V^{\rm alt}/V^{\rm ori}=0.30-0.46$ ; Table S2). There was no gain in any major element, losses in SiO<sub>2</sub>, Fe<sub>2</sub>O<sub>3</sub>, MgO, CaO, Na<sub>2</sub>O, and K<sub>2</sub>O, and no significant change in TiO<sub>2</sub>, Al<sub>2</sub>O<sub>3</sub>, or MnO. Gains in Ba, Rb, Cs, and some HFSEs (Th and Zr) and losses in Eu, Pb, Sr, and Sc were observed, with no significant change in La–Sm, Gd, Y, U, or some other HFSEs (Nb, Hf, and Ta).

# References in the supplementary material

- Ague JJ (2017) Element mobility during regional metamorphism in crustal and subduction zone environments with a focus on the rare earth elements (REE). Am Mineral 102:1796–1821. <a href="https://doi.org/10.2138/am-2017-6130">https://doi.org/10.2138/am-2017-6130</a>
- Ague JJ, Van Haren JL (1996) Assessing metasomatic mass and volume changes using the bootstrap, with application to deep crustal hydrothermal alteration of marble. Economic Geology 91:1169-1182. <a href="https://doi.org/10.2113/gsecongeo.91.7.1169">https://doi.org/10.2113/gsecongeo.91.7.1169</a>
- Baumgartner LP, Olsen SN (1995) A least-squares approach to mass transport calculations using the isocon method. Economic Geology 90:1261-1270. <a href="https://doi.org/10.2113/gsecongeo.90.5.1261">https://doi.org/10.2113/gsecongeo.90.5.1261</a>
- Holland T, Blundy J (1994) Non-ideal interactions in calcic amphiboles and their bearing on amphibole-plagioclase thermometry. Contrib to Mineral Petrol 116:433–447. https://doi.org/10.1007/BF00310910
- Penniston-Dorland SC, Ferry JM (2008) Element mobility and scale of mass transport in the formation of quartz veins during regional metamorphism of the Waits River Formation, east-central Vermont. Am Mineral, 93:7–21. https://doi.org/10.2138/am.2008.2461
- Whitney DL, Evans BW (2010) Abbreviations for names of rock-forming minerals. Am Mineral 95:185–187. <a href="https://doi.org/10.2138/am.2010.3371">https://doi.org/10.2138/am.2010.3371</a>